

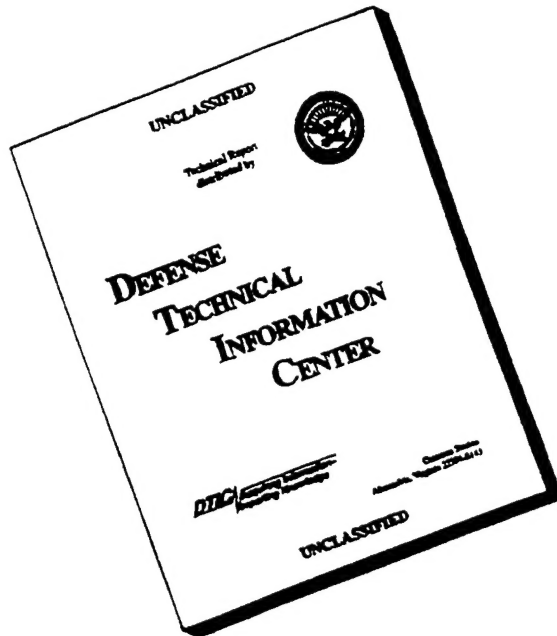
REPORT DOCUMENTATION PAGE

Form Approved
OMB NO. 0704-0188

Public reporting burden for this collection of information is estimated to average 1 hour per response, including the time for reviewing instructions, searching existing data sources, gathering and maintaining the data needed, and completing and reviewing the collection of information. Send comment regarding this burden estimate or any other aspect of this collection of information, including suggestions for reducing this burden, to Washington Headquarters Services, Directorate for Information Operations and Reports, 1215 Jefferson Davis Highway, Suite 1204, Arlington, VA 22202-4302, and to the Office of Management and Budget, Paperwork Reduction Project (0704-0188), Washington, DC 20503.

1. AGENCY USE ONLY (Leave blank)	2. REPORT DATE	3. REPORT TYPE AND DATES COVERED	
	October 1996	Final 08/01/92-05/31/96	
4. TITLE AND SUBTITLE	5. FUNDING NUMBERS		
Fracture and Fatigue of Piezoelectric Ceramics and Development of an Adaptive Sandwich Structure		F49620-92-J-0457	
6. AUTHOR(S)			
C. T. Sun			
7. PERFORMING ORGANIZATION NAMES(S) AND ADDRESS(ES)	AFOSR-TR-96 G537		
School of Aeronautics and Astronautics Purdue University West Lafayette, Indiana 47907-1282			
9. SPONSORING / MONITORING AGENCY NAME(S) AND ADDRESS(ES)	10. SPONSORING / MONITORING AGENCY REPORT NUMBER		
Air Force Office of Scientific Research 110 Duncan Ave. Bolling AFB, DC 20332-6448	NA	92-J-0457	
11. SUPPLEMENTARY NOTES			
The views, opinions and/or findings contained in this report are those of the author(s) and should not be construed as an official Department of the Army position, policy or decision, unless so designated by other documentation			
12a. DISTRIBUTION / AVAILABILITY STATEMENT	19961104 078		
Approved for public release; distribution unlimited.			
3. ABSTRACT (Maximum 200 words) Electrical fields have significant effects on fracture and fatigue of piezoelectric materials. As a result, classical fracture criteria in terms of stress intensity and total potential energy release rate are no longer valid for piezoelectric materials. In this research, we propose the mechanical strain energy release rate to characterize fracture toughness and fatigue crack growth rate in PZT-4 piezoceramic. Fracture and fatigue tests using various specimens were performed to validate the proposed fracture criterion and fatigue model. The results are promising.			
The durability of a smart structure depends only on the durability of its piezoelectric actuators and interfacial bonds. To this end, stresses in the actuator and along the interfaces between the actuator and the host structure must be reduced. As part of this research effort, an adaptive sandwich beam was investigated. The sandwich consists of stiff face sheets with a core consisting partly of piezoceramic and partly honeycomb (a rigid foam) actuators. The piezoelectric core is positioned in such a way that an electric field in the thickness direction would generate thickness shear deformation in the core. This new sandwich construction offers many advantages over conventional surface-mounted actuators in reducing stresses in the actuator and enhancing deflection of the beam.			
4. SUBJECT TERMS	15. NUMBER OF PAGES 83		
Piezoelectricity, Fracture, Fatigue, Energy Release Rate, Actuator, Sandwich Beam		16. PRICE CODE	
7. SECURITY CLASSIFICATION OR REPORT UNCLASSIFIED	18. SECURITY CLASSIFICATION OF THIS PAGE UNCLASSIFIED	19. SECURITY CLASSIFICATION OF ABSTRACT UNCLASSIFIED	20. LIMITATION OF ABSTRACT UL

DISCLAIMER NOTICE



THIS DOCUMENT IS BEST
QUALITY AVAILABLE. THE
COPY FURNISHED TO DTIC
CONTAINED A SIGNIFICANT
NUMBER OF PAGES WHICH DO
NOT REPRODUCE LEGIBLY.

TABLE OF CONTENTS

	Page
1. INTRODUCTION.....	1
2. A FRACTURE CRITERION FOR PIEZOELECTRIC CERAMICS.....	2
2.1 Fracture Criteria.....	2
2.2 Experiments and Comparison with Prediction.....	3
2.2.1 Compact Tension Test.....	3
2.2.2 Mixed Mode Fracture.....	5
2.2.3 Vickers Indentation Test.....	7
2.3 Concluding Remarks.....	11
3. FATIGUE CRACK GROWTH BEHAVIOR IN PIEZOELECTRIC CERAMICS.....	12
3.1 Fatigue Crack Growth Under Combined Mechanical and Electrical Loading Using Compact Tension Specimen.....	12
3.2 Fatigue Crack Growth in Piezoceramics Under Electrical Loads.....	14
3.3 Concluding Remarks.....	15
4. DEVELOPMENT OF ADAPTIVE SANDWICH STRUCTURES.....	16
APPENDIX.....	20

1. INTRODUCTION

Smart materials such as SMA and piezoelectric materials offer promising applications in many adaptive structures enabling the development of new structural control. Potential applications include shape control of large space structures, active noise and vibration control, flutter suppression, and microservoelasticity in flight vehicles.

To deliver the maximum actuation power, piezoelectric actuators are subjected to high electric fields and strains. The development of reliability and life prediction methodologies for piezoceramics is of vital importance to the technology of smart structures. The result of this research concerning the behavior of fracture and fatigue crack growth in PZT piezoceramics under combined electrical and mechanical loads is an important step to the aforementioned goal.

In general, to prolong the service life of piezoceramic actuators, electrical and mechanical loads must be kept as low as possible. In other words, efficiencies of actuation must be high. To achieve this goal, optimal placement of actuators must be determined. In this project we also investigated a new type of adaptive sandwich structure in which the piezoceramic actuator is placed between two stiff face sheets. The thickness shear mode of actuation is utilized. This new construction of adaptive structures was compared with the surface mounted design commonly adopted by researchers.

The main text of this report summarizes the highlights of the results obtained under this research project. Technical details can be found in the reproduction of papers attached in the Appendix.

2. A FRACTURE CRITERION FOR PIEZOELECTRIC CERAMICS

Unlike non-piezoelectric materials, there are electric field effects on fracture of piezoelectric materials. Due to this phenomenon, fracture criteria for non-piezoelectric materials are not directly applicable. Some efforts have been made to establish the fracture criterion for piezoelectric materials. Until now, the total potential energy release rate has been proposed as the fracture criterion. However, an unusual result was found in that the total potential energy release rate is always negative in the absence of mechanical loading, and the presence of electrical loading always reduces the total potential energy release rate, implying that the electric field would impede crack propagation. Although experimental results are still lacking, the few that exist contradict the behavior predicted by the total potential energy release rate criterion.

2.1 Fracture Criteria

Stress Intensity Factor

Consider an infinite piezoelectric medium containing a center crack of length $2a$. The crack is parallel to the x_2 -axis and perpendicular to the x_3 -axis. Remote stresses σ_{33}^∞ and σ_{23}^∞ and electric displacement D_3^∞ are applied. Using the conventionally defined stress intensity factors and electric displacement intensity factor, stresses and electric displacement at the crack tip in the crack plane, $\theta = 0^\circ$, are given by

$$\sigma_{23} = \frac{K_{II}}{\sqrt{2\pi r}}, \quad \sigma_{33} = \frac{K_I}{\sqrt{2\pi r}}, \quad D_3 = \frac{K_{IV}}{\sqrt{2\pi r}} \quad (1)$$

where $K_I = \sqrt{\pi a} \sigma_{33}^\infty$, $K_{II} = \sqrt{\pi a} \sigma_{23}^\infty$, $K_{IV} = \sqrt{\pi a} D_3^\infty$

It is noted that stresses and electric displacement are uncoupled in this plane. This indicates that the electric loading alone cannot produce mechanical stress in the crack plane ahead of the crack tip and vice versa. If the stress intensity factor is used as a fracture criterion, the effect of the electric field cannot be accounted for.

Total Energy Release Rate

Another fracture criterion for piezoelectric materials is based on the total energy release rate. It includes mechanical and electrical energies released as the crack propagates. and is given by

$$J = \int_{\Gamma} \left[H n_2 - \sigma_{ij} n_j u_{i,2} + D_i E_{3n_i} \right] d\Gamma \quad i,j = 2,3 \quad (2)$$

where $H = \frac{1}{2}c_{ijkl}s_{ij}s_{kl} - \frac{1}{2}\epsilon_{ij}E_iE_j - e_{ikl}s_{kl}E_i$ is the electric enthalpy, Γ is an integration contour around the crack tip, \mathbf{n} is the unit normal vector to the contour, σ_{ij} , s_{ij} , and E_i represent stress, strain and electric field, respectively, and c_{ijkl} , e_{ikl} , and ϵ_{ij} represent elastic constants, piezoelectric constants and dielectric permittivities, respectively. Alternatively, J can be obtained by using the crack closure integral as

$$J = G = \lim_{\delta \rightarrow 0} \frac{1}{2\delta} \int_0^{\delta} \left\{ \sigma_{i3}(x_2) \Delta u_i(\delta - x_2) + D_3(x_2) \Delta \phi(\delta - x_2) \right\} dx_2 \quad i = 2, 3 \quad (3)$$

where δ is the assumed crack extension and u_i and ϕ are displacements and electric potential, respectively.

Mechanical Strain Energy Release Rate

Considering the mechanical process of fracture, we proposed to use the mechanical strain energy release rate as the fracture criterion for piezoelectric materials. The mechanical strain energy release rate includes only mechanical strain energy released as the crack propagates. The mechanical strain energy release rates can be calculated by using the crack closure integrals as

$$G_I^M = \lim_{\delta \rightarrow 0} \frac{1}{2\delta} \int_0^{\delta} \sigma_{33}(x_2) \Delta u_3(\delta - x_2) dx_2 \quad (4)$$

$$G_{II}^M = \lim_{\delta \rightarrow 0} \frac{1}{2\delta} \int_0^{\delta} \sigma_{23}(x_2) \Delta u_2(\delta - x_2) dx_2 \quad (5)$$

for Mode I and Mode II, respectively.

The crack closure integrals given by (4) and (5) can be evaluated using nodal forces and displacements with a finite element program. The use of finite elements enables one to consider bodies of finite dimension as well as general loading conditions.

2.2 Experiments and Comparison with Prediction

2.2.1 Compact Tension Test

Mode I fracture experiments were conducted to verify the proposed strain energy release rate as a fracture criterion using PZT-4 piezoelectric ceramics. Fracture tests using compact tension specimens (see Figs. 1 and 2) were performed for Mode I fracture. Throughout all the experiments, attention was focused on the effect of electric fields on fracture.

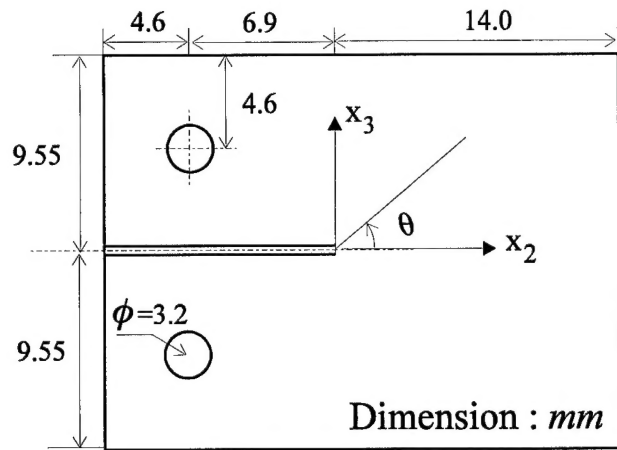


Fig. 1 Compact tension specimen for Mode I fracture test

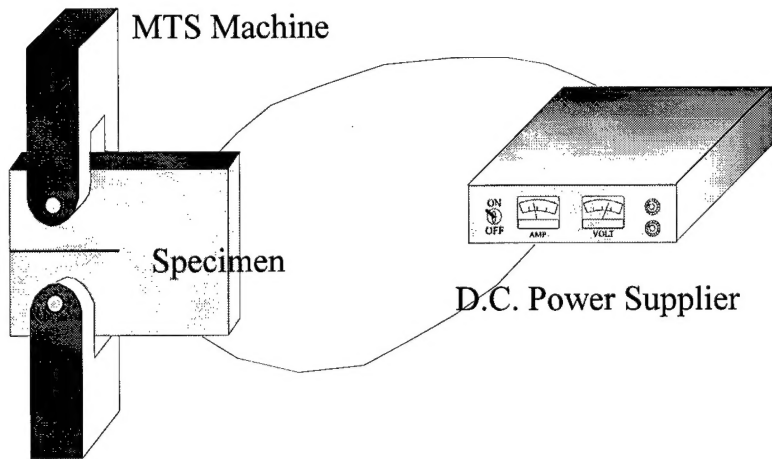


Fig. 2 Test setup for Mode I fracture

Using the fracture load 94 N obtained by the experiment for $E_3 = 0$, i.e., fracture load in the absence of electric field, the finite element analysis was performed. From this analysis, the critical value of the strain energy release rate, G_{IC} , was obtained as $G_{IC} = 2.34(N/m)$. Using this critical strain energy release rate for the PZT-4 piezoelectric ceramic, the fracture loads for other applied electric fields were calculated and shown in Fig. 3. For comparison, the fracture loads predicted according to the total energy release rate are also shown. The superiority of the mechanical strain energy release rate over the total energy release rate criterion is apparent. It is easy to see that the mechanical strain energy release rate criterion predicts the effect of the electric field quite accurately.

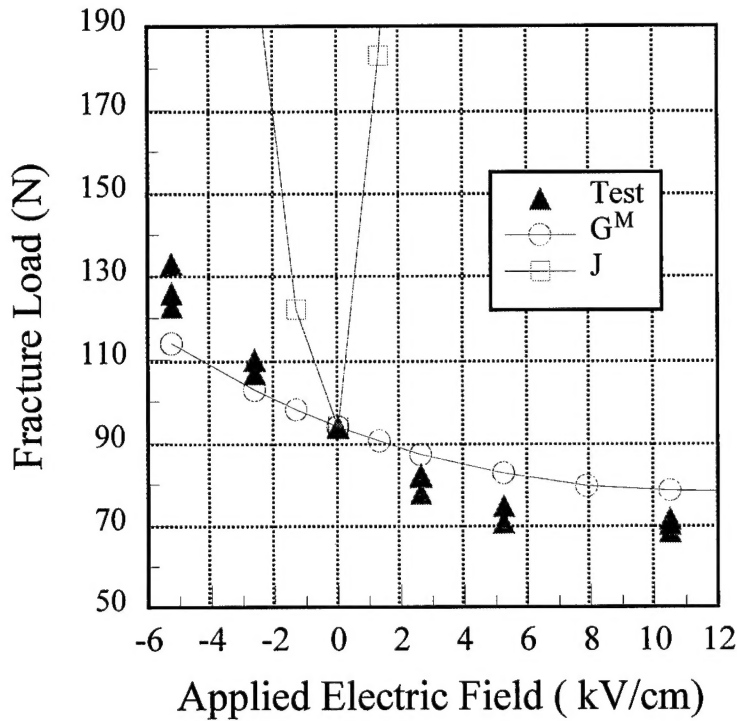


Fig. 3 Comparison of predictions and experimental fracture loads obtained from compact tension specimens

2.2.2 Mixed Mode Fracture

Most mixed mode fracture experiments were performed using oblique crack specimens. Due to the limitation of the size of piezoelectric ceramics, it is difficult to make the oblique crack specimen an experimental model. The symmetric three point bend specimen has been used extensively in obtaining Mode I plane strain fracture toughness, K_{IC} . A three point bend specimen with an unsymmetrical crack was adopted for mixed mode fracture.

Specimens were cut to $19.1 \times 9 \times 5.1$ mm dimension and poling direction was placed along the 19.1 mm dimension. Surfaces of the specimen were polished with 9 mm grain sized diamond abrasive paste. Cracks were introduced using a 0.46 mm thick diamond wheel cutter at three different locations, i.e., the midspan, 2 mm and 4 mm from the midspan. As was done in preparing the Mode I compact tension specimen, the crack tip was refined further by a razor blade with diamond abrasive paste. The final depth of the crack was 4 mm.

Figure 4 shows the three point bend setup and specimen. It is noted that the poling direction is parallel to the span of the bending setup. The prepared specimen was placed on the silicon oil tub which was mounted on the MTS machine. The entire setup including indenter was made of Plexiglas to avoid electric discharging. Critical loads which caused fracture were measured for each set of specimens for

various electric fields. For each electric field and crack location, three tests were performed.

Figures 5 and 6 present comparisons of predicted fracture initiation loads with experimental results for the two off-center cracks. The agreement is fairly good.

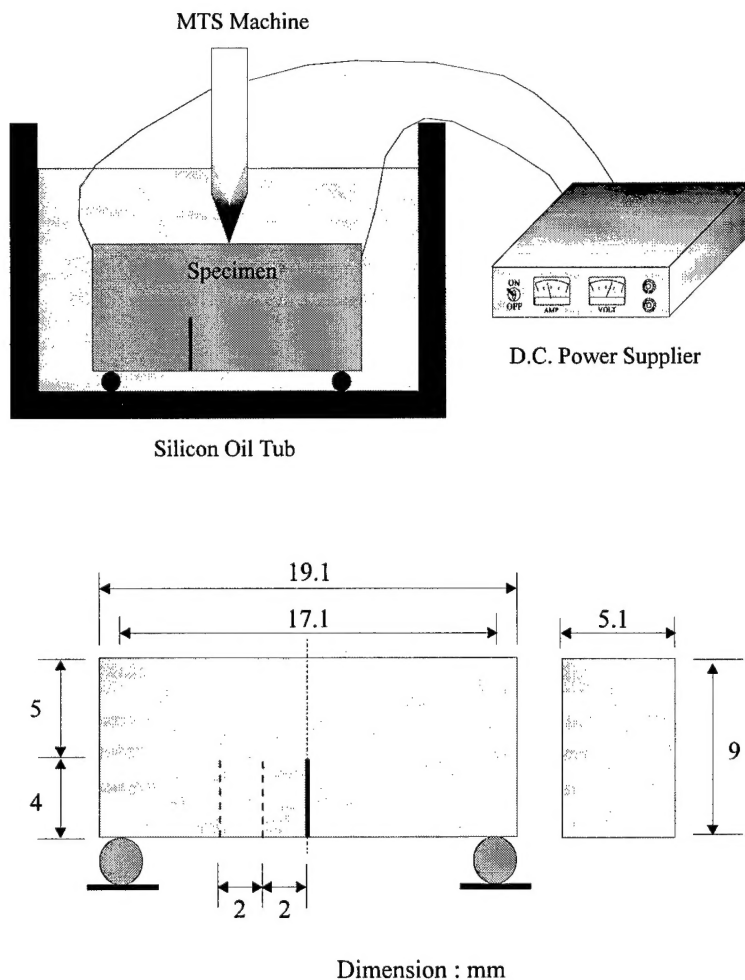


Fig. 4 Three point bending setup for mixed mode fracture test

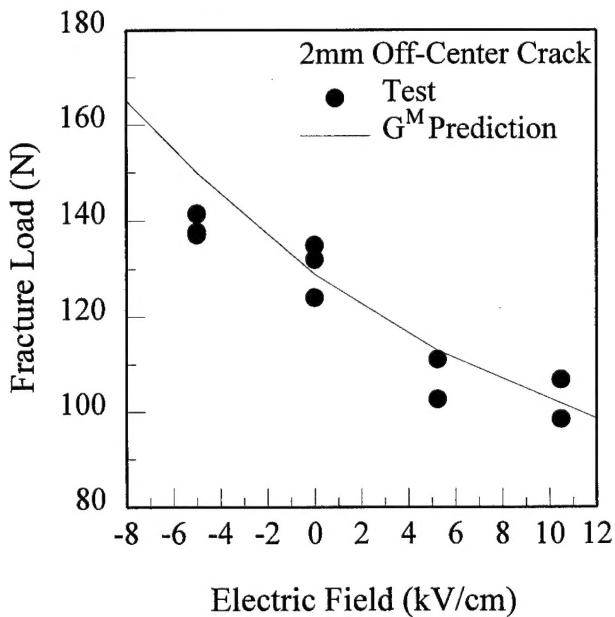


Fig. 5 Comparison of fracture loads for 2 mm off-center crack

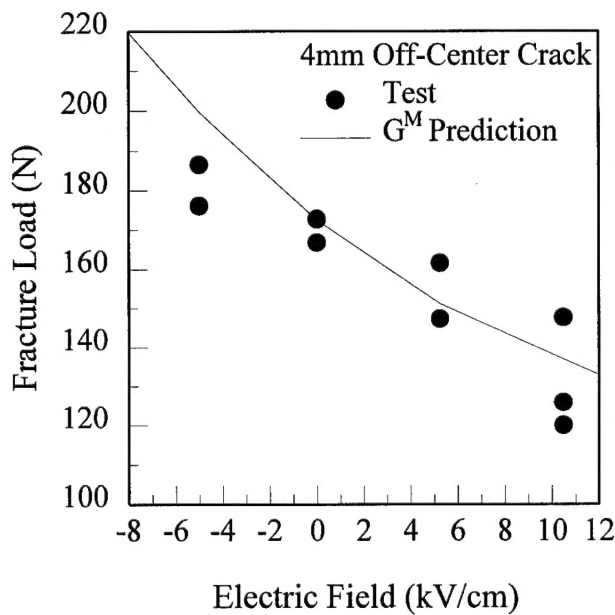


Fig. 6 Comparison of fracture loads for 4 mm off-center crack

2.2.3 Vickers Indentation Test

Although more accurate, the test using compact tension specimen is slow and expensive. Recently, we attempted to apply Vickers indentation tests to determine the fracture toughness of piezoelectric ceramics in the presence of electric loads. Basically, the fracture toughness is to be determined from the indentation force and the resulting crack lengths (a and b) as shown in Fig. 7.

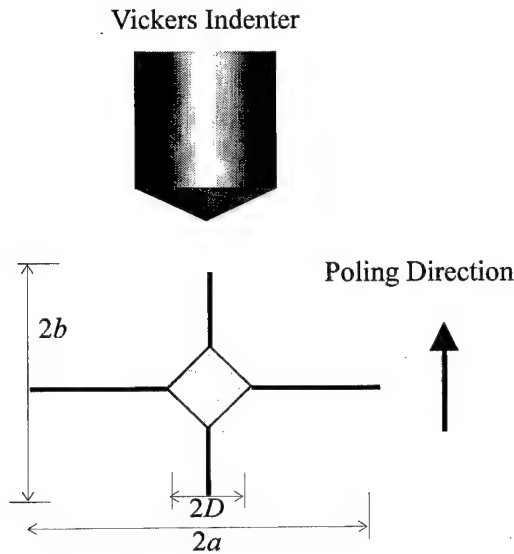


Fig. 7 Dimensions of crack formed by a Vickers indenter.

Using the expression of Mode I mechanical strain energy release rate for an infinite plate, we derived the mechanical strain energy release rate in terms of the indentation load and applied electric field as

$$G_I^M = 2.71 \times 10^{-15} \left(\frac{E}{H} \right) P^2 a^{-3} + 3.78 \times 10^{-12} \left(\frac{E}{H} \right)^{\frac{1}{2}} P E_3^\infty a^{-1} \quad (6)$$

where E and H are Young's modulus and Vickers hardness, respectively. This relation represents the first attempt to determine fracture toughness in piezoelectric ceramics in the presence of electric fields using Vickers indentation.

Taking the critical strain energy release rates from the indentation test, the crack lengths under electric fields were predicted for each indentation loading using Eq. (6) and measured crack lengths. Figures 8 and 9 show the predicted crack length versus the electric field for 9.8N and 49.0N indentation loads, respectively. It is seen that the predictions agree with the experimental results very well for positive electric fields. However, the predictions deviate from the experimental data significantly for negative electric fields, especially for the case of the larger indentation load.

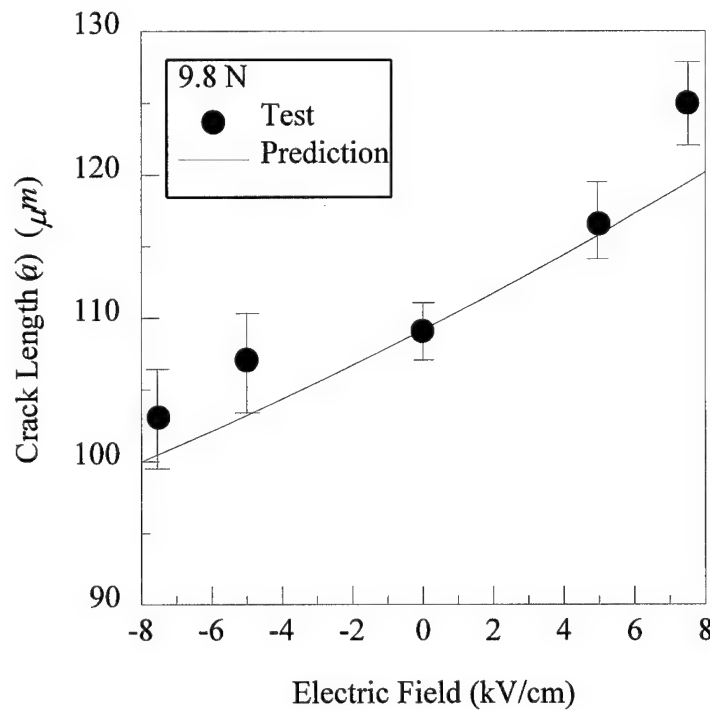


Fig. 8 Prediction of crack length under electric field using the mechanical strain energy release criterion for $P = 9.8$ N.

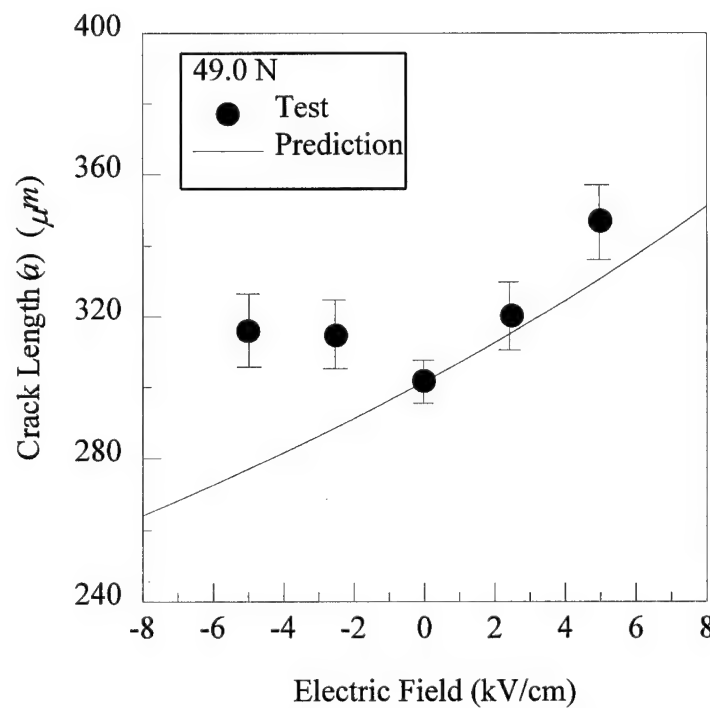


Fig. 9 Prediction of crack length under electric field using the mechanical strain energy release criterion for $P = 49.0$ N.

A possible explanation for this deviation is as follows. In calculating the mechanical strain energy release rate, crack surfaces were modeled as insulated boundary conditions. Considering the low electric permittivity of air or silicone oil, this assumption can be justified for the compact tension test since the width of the machine-notched initial crack was large enough and crack surfaces were always opened both under positive and negative electric fields. For the Vickers indentation test, however, due to the plasticity beneath the indentation, there already exists a contact region right after the indentation. The positive electric field tends to open the crack. However, the specimen is in contraction under a negative electric field and the indentation-produced crack surfaces might be still in contact. This would produce a wedging mechanism that could cause additional crack growth.

Fracture Toughness in Depoled Piezoceramic

Several specimens were depoled by annealing over the Curie temperature to eliminate the piezoelectric property and residual stresses. With this test, changes in fracture toughness of the PZT-4 piezoelectric ceramic by the poling process was also investigated. To depole the as-received specimen, the specimen was placed on a heating oven under 1000°C for two hours and cooled down in the air. A modified empirical formula for fracture toughness based on the Vickers indentation test is obtained as:

$$K_{IC}^* = 0.006 \left(\frac{E}{H} \right)^{\frac{1}{2}} \text{Pa}^{-1.62} \quad (7)$$

Figure 10 shows stress intensity factors for unpoled and poled specimens using the modified equation, Eq. (6). From the figure, it is noted that fracture toughness was changed by the poling process and exhibits strong anisotropy. On the other hand, for the depoled specimen, $a = b$, indicating that fracture toughness is isotropic in the depoled specimen.

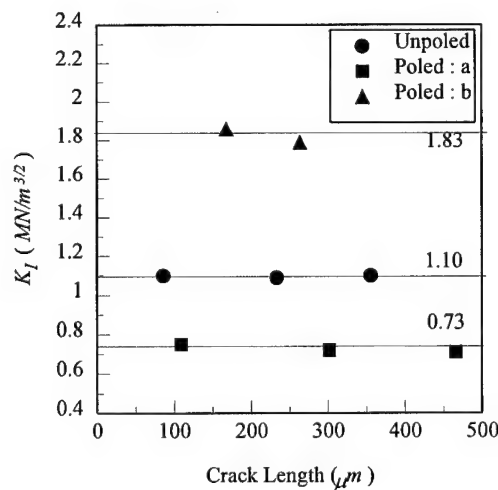


Fig. 10 Stress intensity factor under different indentation loads or crack lengths for unpoled and poled PZT-4.

2.3 Concluding Remarks

From the results of the present study, the following conclusions have been obtained.

- Stress intensity factors and the total energy release rate are not suitable for describing the fracture behavior of piezoelectric ceramics.
- The mechanical strain energy release rate is a promising fracture criterion for piezoelectric ceramics.
- Positive electrical fields aid crack propagation while negative electrical fields impede crack propagation. In other words, positive electric fields decrease the apparent fracture toughness of piezoelectric ceramics while negative electric fields increase it.

3. FATIGUE CRACK GROWTH BEHAVIOR IN PIEZOELECTRIC CERAMICS

Durability of piezoceramic actuators is an important aspect of smart structure technology. Fatigue failure is caused by crack nucleation and propagation. This part of the research concerns the mechanism and prediction methodology for fatigue crack growth in piezoceramics under cyclic mechanical and electrical loads. Two types of specimens were used for the fatigue study, namely, the compact tension specimen and cracks produced by Vickers indentation.

3.1 Fatigue Crack Growth Under Combined Mechanical and Electrical Loading Using Compact Tension Specimen

Compact tension specimens of PZT-4 piezoceramic similar to that shown in Figs. 1 and 2 were used for the fatigue crack growth study. Two types of loading were considered. In the first type of loading, cyclic tension-tension mechanical loads were applied while keeping the electric load constant. The mechanical load was applied using an MTS machine and the electrical load was applied using a 50 kV d.c. power amplifier. In the second type of loading, the mechanical load was kept constant while a half sine wave of electrical field was applied to the specimen.

In order to avoid discharging through the air and to ensure an insulated crack surface boundary condition, the specimen was immersed in a transparent Plexiglas tub filled with silicon oil. A traveling microscope was used to measure the crack length.

Figures 11 and 12 present the results for the two types of loading, respectively. For both types of loading, a positive electric field can produce a greater crack growth than a negative electric field for the same mechanical load. From the results of Figs. 11 and 12 the crack growth rate da/dN can be obtained and plotted versus the range of the mechanical strain energy release rate ΔG^M for both loadings in log-log plots as shown in Fig. 13. It is interesting to note that all these crack growth curves collapse into a single curve. This indicates that crack growth in the piezoceramic is controlled by the mechanical strain energy release rate G^M , and a fatigue crack growth law similar to the Paris law can be established.

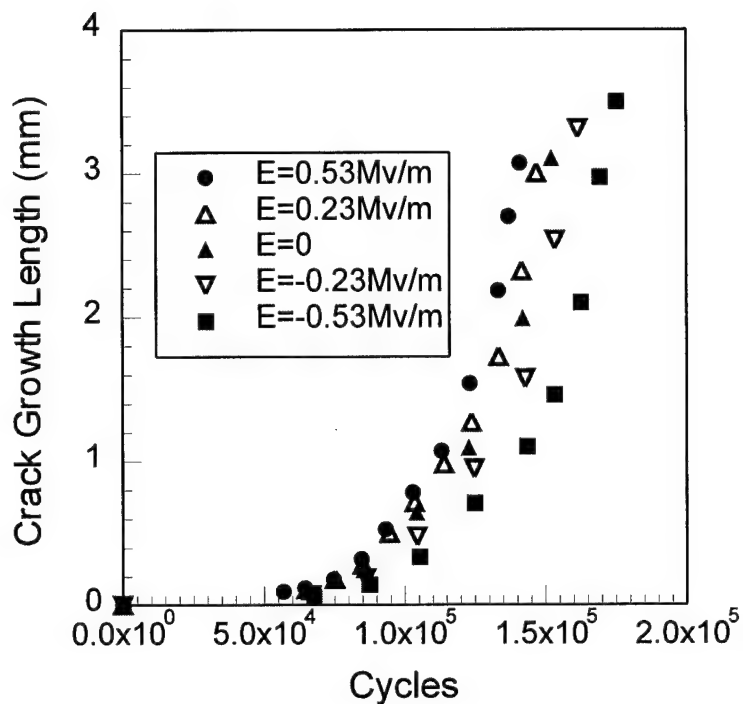


Fig. 11 Crack growth length vs. number of cycles for cyclic mechanical loading with constant electrical loading

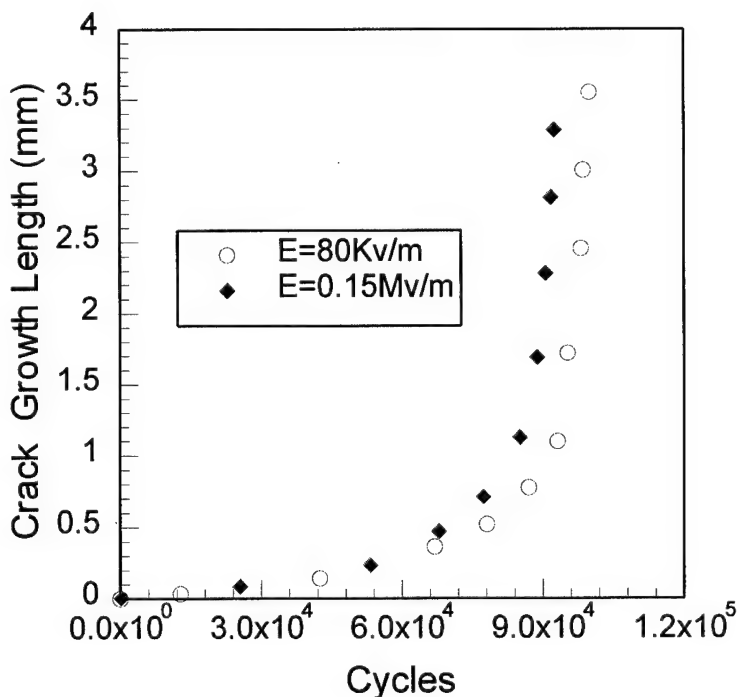


Fig.12 Crack growth length vs. number of cycles for cyclic electrical loading with constant mechanical loading

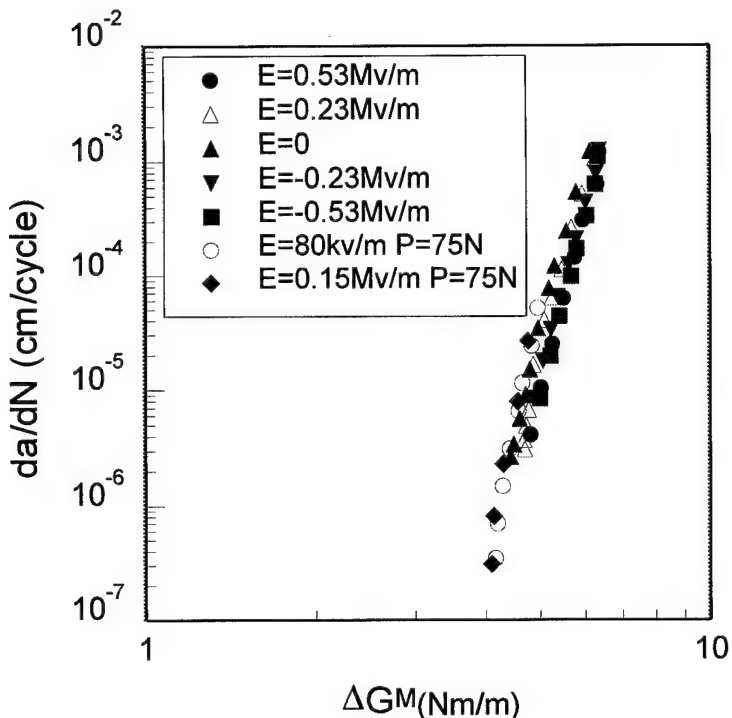


Fig. 13 Crack growth rate da/dN vs. G^M for both types of loading

3.2 Fatigue Crack Growth in Piezoceramics Under Electrical Loads

This part of the research concerns the mechanism and prediction of fatigue crack growth in piezoelectric materials under the action of cyclic electric loading. In this study, the precrack is generated by Vickers indentation. On the basis of mechanical energy release rate, the electric field alone cannot cause crack propagation. However, since the precrack was formed by Vickers indentation, residual stresses exist after unloading. Therefore, crack growth may result from interaction of the residual stress and electric field rather than from the electric field alone. The applied AC electric field with 60 Hz on PZT-4 piezoceramic specimens was determined by averaging the measured crack length of a set of indentations after certain cycles. The crack lengths were measured from an optical microscope.

The results showed that the crack propagates a certain amount under the pure cyclic electric loading with a range from 1.5 kv/cm to 7.5 kv/cm. During crack growth, the major crack, which is perpendicular to the poling direction, propagates dominantly. In order to account for the different contributions from negative and positive electric fields, the circuit is modified so that a half wave can be generated. Figure 14 shows the comparison of crack lengths produced by the full wave, the negative and positive half wave electric fields with peak value of 5 kv/cm. The crack length for the full wave grew by 14 % while 9 % and 4.5 % for positive and negative fields, respectively. It is noted that the crack growth under action of the positive cyclic electric field is much greater than that under the negative electric field.

This phenomenon can be explained as follows. During the indentation with Vickers indenter, a plastic zone is created inside the penny-shaped crack. Tensile residual stresses exist near the crack tip after indentation. On the other hand, a negative electric field when coupled with the crack tip tensile residual stress would yield a smaller strain energy release rate and thus less crack growth. A positive electric field through the coupling with the tensile residual stresses would produce a significant mechanical strain energy release rate that would produce fatigue crack growth. Once the residual stress releases, the crack may stop growing. While the negative electric field is applied, the plasticity zone keeps in contact and acts as a wedge. The wedge effect causes the crack to grow further. The wedge effect becomes small while the crack grows. Finally, the crack growth arrests once the wedge effect disappears.

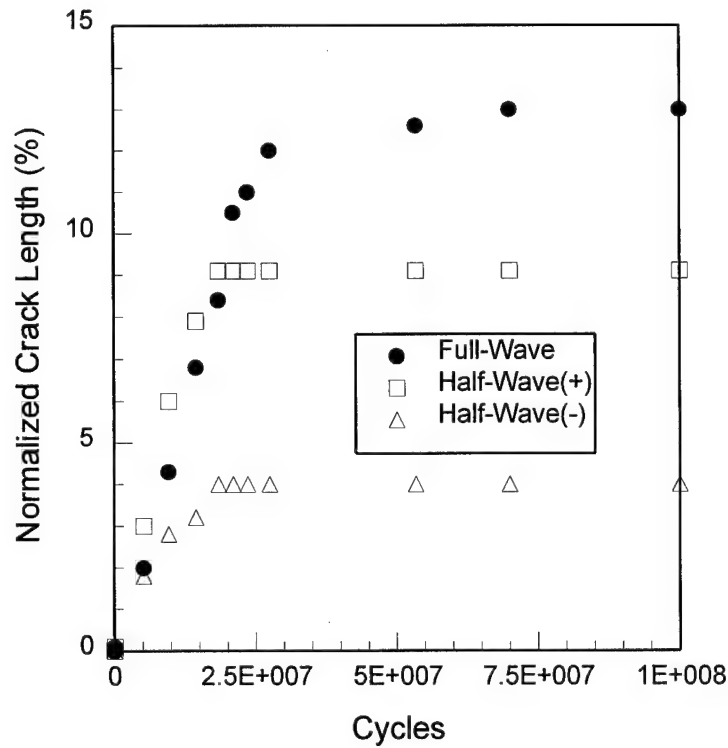


Fig. 14 Fatigue crack growth under cyclic electric loading.

3.3 Concluding Remarks

For the same mechanical loading, a positive electric field would produce a faster crack growth rate than a negative electric field. Nevertheless, combined mechanical and electrical loading can be represented in terms of a single variable in the mechanical strain energy release rate G^M . The experimental result shows that the Paris law can be adopted for fatigue crack growth in piezoceramics if ΔG^M is used as the controlling parameter.

4. DEVELOPMENT OF ADAPTIVE SANDWICH STRUCTURES

Piezoceramic actuators in an adaptive structure are either surface-mounted (see Fig. 15a) or embedded in the host structure. Although effective in actuation, surface-mounted actuators are susceptible to damage inflicted by contact with surrounding objects. Furthermore, being placed at the extreme thickness positions of the structure, the actuator would be subjected to high bending stresses which may prove to be detrimental to the brittle piezoceramic material. Embedding actuators in composite structures is possible. However, to accommodate the actuator, the composite material must be cut and removed, causing significant reduction in stiffness, strength, and durability of the host structure.

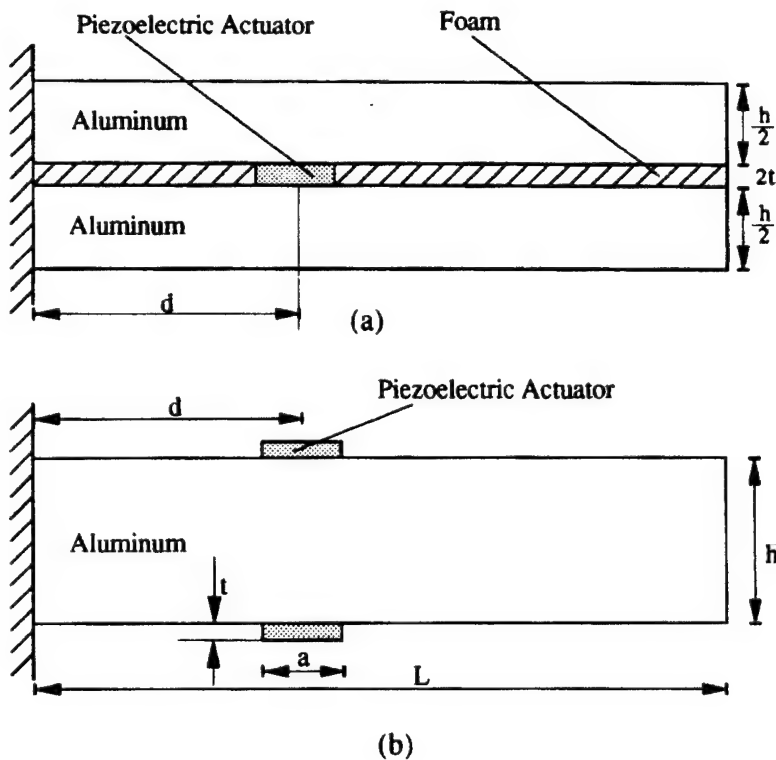


Fig. 15 Adaptive sandwich beam (a) and surface-mounted actuation beam (b)

In this study, a sandwich construction for adaptive structures is investigated. The sandwich consists of stiff facing sheets with a core consisting of partly honeycomb (or rigid foam) and partly piezoelectric ceramics (see Fig. 15b). The piezoelectric core is positioned in such a way that an electric field in the thickness direction would generate the thickness (or transverse) shear deformation of the core (see Fig. 16). The transverse shear deformation in the core would produce the desired transverse deflection of the sandwich. This new sandwich construction offers many advantages over conventional

constructions. For example, stresses in the piezoelectric core are much lower for achieving the same deflection of the structure. Figure 17 shows the axial (bending) stress distributions over the thickness for the two types of beams under a concentrated force applied at the tip of a cantilever. Figure 18 shows the axial stresses due to electrical loading.

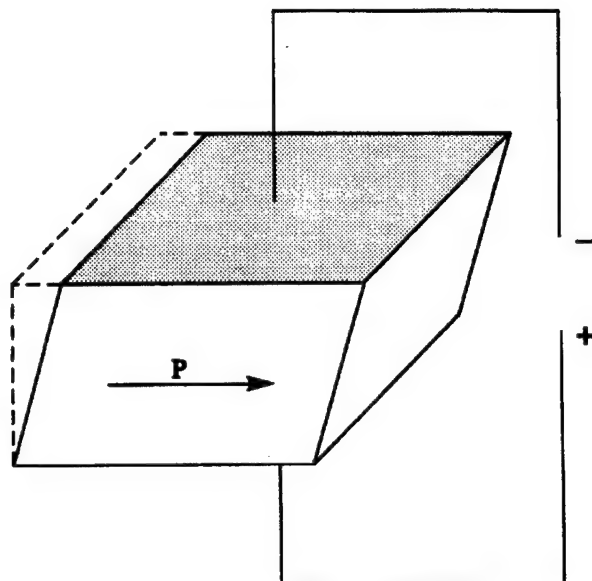


Fig. 16 Shear mode of the piezoelectric core

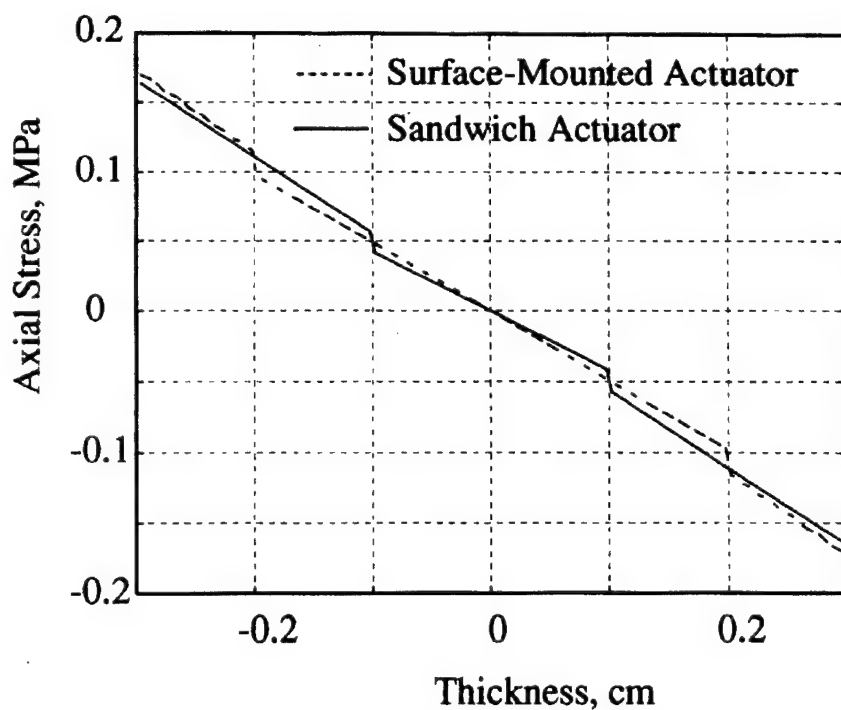


Fig. 17 Axial stress distribution through the thickness
at $d = 1$ cm under mechanical loading

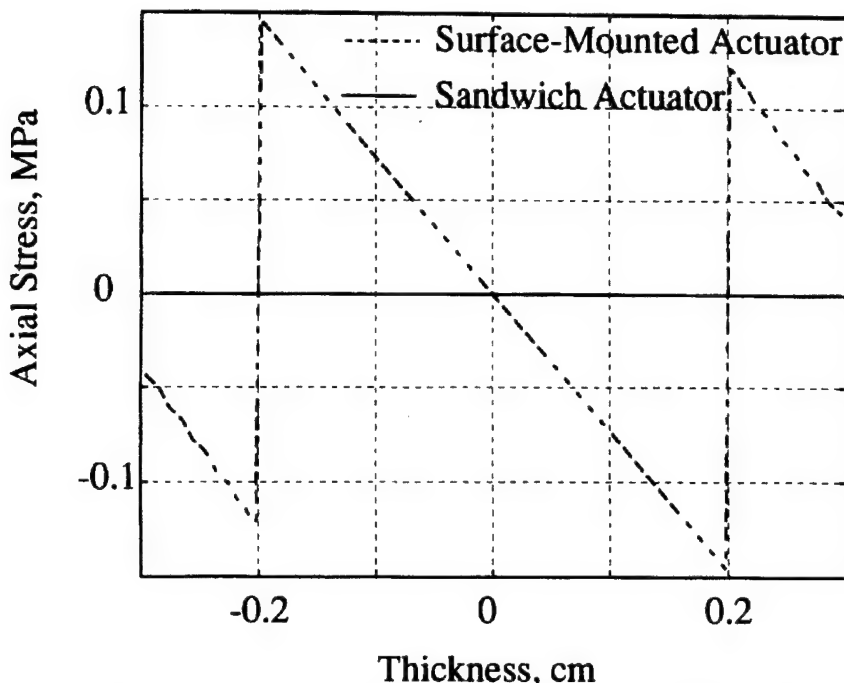


Fig. 18 Axial stress distribution through the thickness
at $d = 1$ cm under electrical loading

Finite element analysis results also indicate that interfacial stresses between the actuator and the host structure in the sandwich beam are much smaller than those in the beam with surface-mounted actuators. Consequently, debonding would be less of a problem in the sandwich beam than in the surface-mounted actuation beam. It is evident that the induced bending stress in the actuator in the sandwich construction is much smaller than that in the surface-mounted actuator.

The result of this study indicates that the use of continuous piezoelectric core in sandwich construction is not necessary. In fact, it is more effective and efficient to use sparsely spaced piezoelectric core. The spaces between the actuators can be filled with light rigid foam or honeycomb core, thus minimizing the added weight penalty.

To compare the deflections produced by these two types of beams, cantilevered beams shown in Fig. 15 are subjected to the same electrical field. The tip deflections of the beams are plotted in Fig. 19 for various locations (d) of the actuator of size $a = 1$ cm. It is evident that the tip deflection for the sandwich beam is much larger than that for the surface-mounted actuation beam.

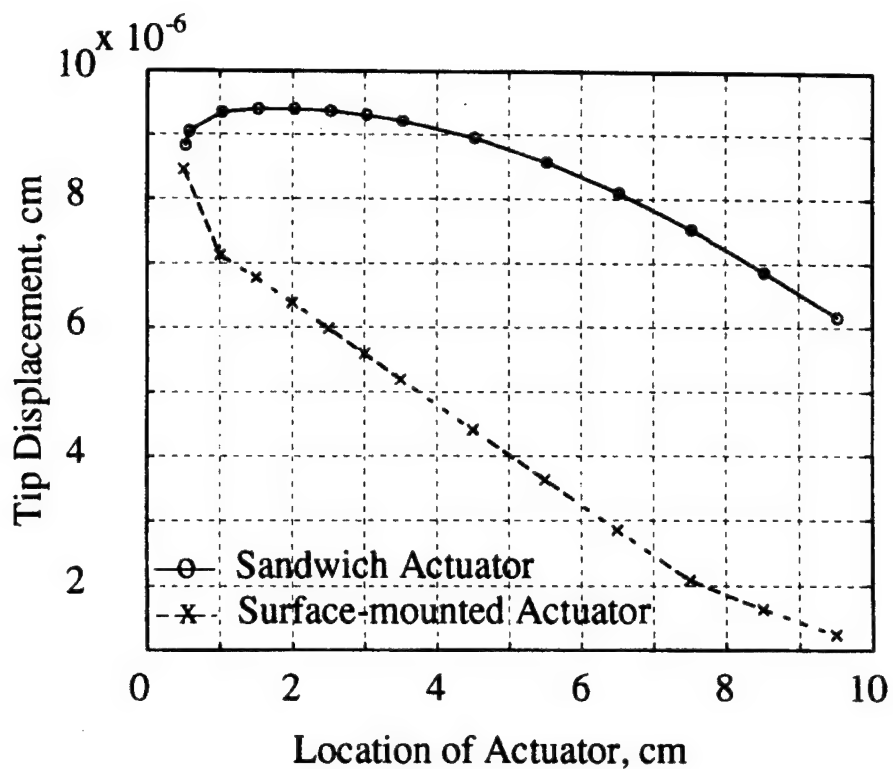


Fig. 19 Effect of actuator location on tip-deflection

APPENDIX

PUBLICATIONS

1. S. B. Park and C. T. Sun, "Effect of Electric Fields on Fracture of Piezoelectric Ceramics", *Int. J. Fracture*, **70**, 203-216 (1995).
2. S. B. Park and C. T. Sun, "Fracture Criteria for Piezoelectric Ceramics", *J. Am. Ceram. Soc.*, **78** [6], 1475-1480 (1995).
3. C. T. Sun and S. Park, "Determination of Fracture Toughness of Piezoelectric Ceramics Under the Influence of Electric Field Using Vickers Indentation", *Proc. 1995 N. Am. Conf. on Smart Structures and Materials*, 26 February-3 March 1995, San Diego, CA.
4. C. T. Sun and X. D. Zhang, "Use of Thickness-Shear Mode in Constructing Adaptive Sandwich Structures", *Smart Materials and Structures*, Vol. 4, 202-206 (1995).
5. X. D. Zhang and C. T. Sun, "Formulation of an Adaptive Sandwich Beam", accepted for publication in *Smart Materials & Structures* (1996).

Effect of electric field on fracture of piezoelectric ceramics

S.B. PARK and C.T. SUN

School of Aeronautics and Astronautics, Purdue University, West Lafayette, Indiana 47907-1282, USA

Received 1 May 1994; accepted in revised form 9 December 1994

Abstract. Closed form solutions for all three modes of fracture for an infinite piezoelectric medium containing a center crack subjected to a combined mechanical and electrical loading were obtained. The explicit mechanical and electrical fields near the crack tip were derived, from which the strain energy release rate and the total potential energy release rate were obtained by using the crack closure integral. The suitability in using the stress intensity factor, the total energy release rate, or the mechanical strain energy release rate as the fracture criterion was discussed.

1. Introduction

Due to the intrinsic coupling effect between mechanical and electrical fields, piezoelectric materials have been widely used as electromechanical devices. Among them, manmade piezoelectric ceramics possess strong coupling characteristics and are used as actuation devices. However, piezoelectric ceramics are very brittle and susceptible to fracture during service. To prevent failure during service, the fracture behavior of these materials must be understood.

Recently several researchers have performed analyses of piezoelectric materials containing a crack. Two crack surface boundary conditions have been considered. One is to consider the crack surface as an electrically conducting surface and the other is as an insulated one. Since dielectric permittivity of piezoelectric ceramics is three orders of magnitude higher than air or vacuum which is considered to be in between crack surfaces, the insulated model is considered closer to reality.

Parton [1] and McMeeking [2] modeled the problem in which a crack was filled with conducting fluids. Later Parton and Kudriyavtsev [3] obtained solutions for insulated cracks. They derived stress and electric displacement fields near the crack tip. Using complex displacement formulation and an insulated crack model, Pak [4] obtained a closed form solution for the antiplane mode III fracture. Sosa and Pak [5] used Williams' eigenfunction expansion method [6] to investigate the singular nature of the near tip stress and electric fields in piezoelectric media. They showed square root singularities in both stresses and electric displacements. Considering a crack in a piezoelectric medium as a limiting case of an elliptical hole, Sosa [7, 8] investigated stress fields near a crack using complex potential formulation. Suo et al. [9] studied in-body and interface crack problems of piezoelectric materials using an integral formalism.

Efforts have been made to establish the fracture criterion for piezoelectric materials. Up to now, the total potential energy release rate has been proposed as the fracture criterion. Similar to the path independent Γ integral of Cherepanov [10], Pak and Herrmann [11] derived the material momentum tensor which accounts for the total potential energy release rate. Pak [4] used it to predict mode III fracture. However, he found an unusual result in that the

total potential energy release rate is always negative in the absence of mechanical loading and the presence of electrical loading always reduces the total potential energy release rate, implying that the electric field would impede crack propagation. This contradicts all available experimental observations [12, 13, 14].

In this study, full field closed form solutions for all three modes of fracture with insulated crack surfaces were derived. Stroh formalism [15, 16] was employed to analyze general anisotropic material properties. This approach was used by other researchers [9, 17, 18]. The solutions were reduced to near tip solutions to investigate the characteristics of stresses induced by mechanical and electric fields. Since fracture itself is a mechanical process, a new fracture criterion based on the mechanical strain energy release rate was proposed.

2. Closed form solutions for crack problem

Field equations for piezoelectric material subjected to mechanical and electrical fields can be written as [19]

$$\sigma_{ij} = c_{ijkl} u_{k,l} + \epsilon_{ijl} \phi_{,l}, \quad D_i = \epsilon_{ikl} u_{k,l} - \epsilon_{il} \phi_{,l}, \quad (1)$$

$$\sigma_{ij,j} = 0, \quad D_{i,i} = 0, \quad (2)$$

where σ_{ij} , u_i , D_i , and ϕ are stresses, displacements, electric displacements, electric potential, respectively; c_{ijkl} , ϵ_{ijk} , ϵ_{ij} are elastic constants, piezoelectric constants, and dielectric permittivities, respectively; and a comma indicates partial derivative. The electric field, E_i , is related to the electric potential, ϕ , as $E_i = -\phi_{,i}$.

Assume that the field variables u_i and ϕ are functions of x_1 and x_2 only, i.e.,

$$u_k = A_k f(z), \quad \phi = A_4 f(z), \quad k = 1, 2, 3, \quad (3)$$

where $z = x_1 + px_2$. Applying field variables, (3), to field equations, (1) and (2), we obtain

$$\begin{aligned} c_{ijkl} A_k f_{,jl} + \epsilon_{ijl} A_4 f_{,jl} &= 0, \quad \epsilon_{jkl} A_k f_{,jl} - \epsilon_{jl} A_4 f_{,jl} = 0 \\ i, k = 1, 2, 3, \quad j, l = 1, 2. \end{aligned} \quad (4)$$

The above system of four homogeneous equations must be singular in order to yield nontrivial solutions for A_k ($k = 1, 2, 3$) and A_4 , i.e.,

$$\begin{vmatrix} c_{i1k1} + (c_{i1k2} + c_{i2k1})p + c_{i2k2}p^2 & \epsilon_{1i1} + (e_{1i2} + e_{2i1})p + e_{2i2}p^2 \\ e_{1k1} + (e_{1k2} + e_{2k1})p + e_{2k2}p^2 & -[\epsilon_{11} + (e_{12} + e_{21})p + e_{22}p^2] \end{vmatrix} = 0. \quad (5)$$

Solving the above characteristic equation, we obtain eight eigenvalues, p 's, forming four conjugate pairs. In terms of these eigenvalues, a general expression for the displacements and electric potential can be written as

$$\nu_m = \sum_{\alpha=1}^4 A_{m\alpha} f_{\alpha}(z_{\alpha}) + \sum_{\alpha=1}^4 \bar{A}_{m\alpha} \bar{f}_{\alpha}(\bar{z}_{\alpha}), \quad m = 1, \dots, 4, \quad (6)$$

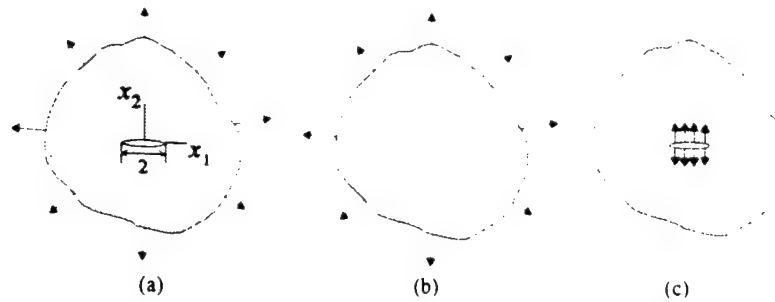


Fig. 1. Decomposition of problem for a piezoelectric material containing a planar crack for all three modes of fracture. (a) Original problem, (b) Far field loadings without a crack, (c) Crack surface loading with a crack.

$$\mathbf{v} = \begin{Bmatrix} u_k \\ \phi \end{Bmatrix}, \quad \mathbf{A} = \begin{bmatrix} A_{k\alpha} \\ A_{4\alpha} \end{bmatrix}, \quad k = 1, 2, 3, \quad \alpha = 1, \dots, 4, \quad (7)$$

where $z_\alpha = x_1 + p_\alpha x_2$, $\bar{z}_\alpha = x_1 + \bar{p}_\alpha x_2$ and the bar indicates complex conjugate.

Defining new stress functions, χ , and electric displacement function, κ , as

$$\sigma_{i1} = -\chi_{i,2}, \quad \sigma_{i2} = \chi_{i,1}, \quad D_1 = -\kappa_{,2}, \quad D_2 = \kappa_{,1}, \quad i = 1, 2, 3, \quad (8)$$

we can obtain the following equations using (1), (6) and (8).

$$\chi_i = \sum_\alpha L_{i\alpha} f_\alpha(z_\alpha) + \sum_\alpha \bar{L}_{i\alpha} \bar{f}_\alpha(\bar{z}_\alpha), \quad \kappa = \sum_\alpha W_\alpha f_\alpha(z_\alpha) + \sum_\alpha \bar{W}_\alpha \bar{f}_\alpha(\bar{z}_\alpha), \quad (9)$$

$$\begin{aligned} L_{i\alpha} &= (c_{i2k1} + p_\alpha c_{i2k2}) A_{k\alpha} + (e_{1i2} + p_\alpha e_{2i2}) A_{4\alpha}, \\ W_\alpha &= (e_{2k1} + p_\alpha e_{2k2}) A_{k\alpha} - (\varepsilon_{21} + p_\alpha \varepsilon_{22}) A_{4\alpha}. \end{aligned} \quad (10)$$

The above can be expressed symbolically as

$$\Phi_m = \sum_\alpha M_{m\alpha} f_\alpha(z_\alpha) + \sum_\alpha \bar{M}_{m\alpha} \bar{f}_\alpha(\bar{z}_\alpha), \quad m = 1, \dots, 4, \quad (11)$$

$$\Phi = \begin{Bmatrix} \chi_i \\ \kappa \end{Bmatrix} \text{ and } M = \begin{bmatrix} L_{i\alpha} \\ W_\alpha \end{bmatrix}, \quad i = 1, \dots, 3, \quad \alpha = 1, \dots, 4. \quad (12)$$

Consider an infinite piezoelectric medium containing a center crack of 2 units in length, see Fig. 1. The body is subjected to arbitrary far field mechanical and electrical loading. This problem can be considered as the superposition of the two sub-problems shown in Figs. 1(b) and (c), respectively.

For problem (c) in Fig. 1, consider the semi-infinite regions $x_2 \geq 0$ and $x_2 \leq 0$ separately. In $x_2 \geq 0$, the displacements and electric potential which have the form of (6) may be written by use of complex Fourier transformation as

$$v_m^+ = \sum_\alpha A_{m\alpha} \int_0^\infty F_\alpha^+ e^{i\rho z_\alpha} d\rho + \sum_\alpha \bar{A}_{m\alpha} \int_0^\infty \bar{F}_\alpha^+ e^{-i\rho \bar{z}_\alpha} d\rho, \quad (13)$$

where the superscript + represents the region $x_2 \geq 0$. The corresponding stress and electric displacement functions are

$$\Phi_m^+ = \sum_{\alpha} M_{m\alpha} \int_0^{\infty} F_{\alpha}^+ e^{i\rho z_{\alpha}} d\rho + \sum_{\alpha} \bar{M}_{m\alpha} \int_0^{\infty} \bar{F}_{\alpha}^+ e^{-i\rho z_{\alpha}} d\rho. \quad (14)$$

Similarly, in $x_2 \leq 0$, we write

$$\nu_m^- = \sum_{\alpha} A_{m\alpha} \int_0^{\infty} F_{\alpha}^- e^{-i\rho z_{\alpha}} d\rho + \sum_{\alpha} \bar{A}_{m\alpha} \int_0^{\infty} \bar{F}_{\alpha}^- e^{i\rho z_{\alpha}} d\rho, \quad (15)$$

$$\Phi_m^- = \sum_{\alpha} M_{m\alpha} \int_0^{\infty} F_{\alpha}^- e^{-i\rho z_{\alpha}} d\rho + \sum_{\alpha} \bar{M}_{m\alpha} \int_0^{\infty} \bar{F}_{\alpha}^- e^{i\rho z_{\alpha}} d\rho. \quad (16)$$

Assume that the faces of the crack are perfectly insulated, the boundary conditions for the problem are (i) stresses and electric displacements must be continuous outside the crack, and (ii) the free boundary conditions of the original problem along the crack surface must be satisfied. Free boundary conditions of crack surfaces include mechanical traction free and electrically insulated surface conditions such as

$$\sigma_{ij} n_j = 0 \quad \text{and} \quad D_i n_i = 0. \quad (17)$$

For the sub-problem in Fig. 1-(c), boundary conditions are

$$(i) \sigma_{i2}^+ = \sigma_{i2}^-, D_2^+ = D_2^- \quad \text{or} \quad \Phi_{m,1}^+ = \Phi_{m,1}^-, \quad |x_1| > 1, x_2 = 0 \quad (18)$$

$$\text{and, } u_k^+ = u_k^-, \phi^+ = \phi^- \quad \text{or} \quad \nu_m^+ = \nu_m^-$$

$$(ii) \sigma_{i2} = -\sigma_{i2}^{\infty}(x_1), D_2 = -D_2^{\infty}(x_1) \quad \text{or} \quad \Phi_{m,1} = -\mathbf{T}_m, \quad |x_1| < 1, x_2 = 0,$$

where, $\Phi = \{\sigma_{i2}^{\infty}(x_1) D_2^{\infty}(x_1)\}^T, i = 1, 2, 3$ are the solutions for the sub-problem Fig. 1(b) at $x_2 = 0$ and $|x_1| \leq 1$.

From the boundary condition (i), the following relations are obtained.

$$F_{\alpha}^+(\rho) = N_{\alpha n} \Psi_n(\rho), \quad F_{\alpha}^-(\rho) = N_{\alpha n} \bar{\Psi}_n(\rho), \quad (19)$$

$$\Psi_m(\rho) = \sum_{\alpha} M_{m\alpha} F_{\alpha}^+(\rho), \quad \sum_{\alpha} M_{m\alpha} N_{\alpha n} = \delta_{mn}, \quad m, n = 1, \dots, 4,$$

Applying the relations of (19) into (13)–(16), the boundary conditions become

$$\int_0^{\infty} \{\Psi_n(\rho) e^{i\rho x_1} d\rho - \bar{\Psi}_n(\rho) e^{i\rho x_1}\} d\rho = 0, \quad |x_1| > 1, \quad x_2 = 0, \quad (20)$$

$$\int_0^{\infty} \{\Psi_n(\rho) e^{i\rho x_1} d\rho - \bar{\Psi}_n(\rho) e^{i\rho x_1}\} \rho d\rho = iT_n, \quad |x_1| < 1, \quad x_2 = 0. \quad (21)$$

Equations (20) and (21) form two sets of dual integral equations which are to be solved to obtain Ψ_n . For the case where the remote applied stresses and electric displacements are

constant, the solutions for Ψ_n are obtained following Stroh's solutions for elastic materials [13, 14]. The corresponding v and Φ are given by

$$\nu_m = \frac{1}{2} \sum_{\alpha} \{ A_{m\alpha} N_{\alpha n} [(z_{\alpha}^2 - 1)^{1/2} - z_{\alpha}] + \bar{A}_{m\alpha} \bar{N}_{\alpha n} [(\bar{z}_{\alpha}^2 - 1)^{1/2} - \bar{z}_{\alpha}] \} T_n, \quad (22)$$

$$\Phi_m = \frac{1}{2} \sum_{\alpha} \{ M_{m\alpha} N_{\alpha n} [(z_{\alpha}^2 - 1)^{1/2} - z_{\alpha}] + \bar{M}_{m\alpha} \bar{N}_{\alpha n} [(\bar{z}_{\alpha}^2 - 1)^{1/2} - \bar{z}_{\alpha}] \} T_n. \quad (23)$$

Using relations given by (8) and adding the solution for Fig. 1(b), we obtain the stresses and electric displacements as

$$\begin{aligned} \sigma_{k1} = & -\frac{1}{2} \sum_{\alpha} \{ M_{k\alpha} N_{\alpha n} p_{\alpha} [z_{\alpha} (z_{\alpha}^2 - 1)^{-1/2} - 1] \\ & + \bar{M}_{k\alpha} \bar{N}_{\alpha n} \bar{p}_{\alpha} [\bar{z}_{\alpha} (\bar{z}_{\alpha}^2 - 1)^{1/2} - 1] \} T_n, \end{aligned} \quad (24)$$

$$\sigma_{k2} = \frac{1}{2} \sum_{\alpha} \{ M_{k\alpha} N_{\alpha n} z_{\alpha} (z_{\alpha}^2 - 1)^{-1/2} + \bar{M}_{k\alpha} \bar{N}_{\alpha n} \bar{z}_{\alpha} (\bar{z}_{\alpha}^2 - 1)^{1/2} \} T_n. \quad (25)$$

$$\begin{aligned} D_1 = & -\frac{1}{2} \sum_{\alpha} \{ M_{4\alpha} N_{\alpha n} p_{\alpha} [z_{\alpha} (z_{\alpha}^2 - 1)^{-1/2} - 1] \\ & + \bar{M}_{4\alpha} \bar{N}_{\alpha n} \bar{p}_{\alpha} [\bar{z}_{\alpha} (\bar{z}_{\alpha}^2 - 1)^{1/2} - 1] \} T_n, \end{aligned} \quad (26)$$

$$D_2 = \frac{1}{2} \sum_{\alpha} \{ M_{4\alpha} N_{\alpha n} z_{\alpha} (z_{\alpha}^2 - 1)^{-1/2} + \bar{M}_{4\alpha} \bar{N}_{\alpha n} \bar{z}_{\alpha} (\bar{z}_{\alpha}^2 - 1)^{-1/2} \} T_n, \quad (27)$$

$$k = 1, 2, 3, \quad n = 1, \dots, 4.$$

3. Near tip solutions

The stress and electric fields near the crack tip are of interest; they can be derived from the full field solutions. Let the origin of the polar coordinates, r and θ , be located at the right crack tip, see Fig. 2. Then

$$z_{\alpha} = 1 + r(\sin \theta + p_{\alpha} \cos \theta). \quad (28)$$

Take the radial distance r to be small compared to unity, then the full field solutions reduce to

$$\begin{aligned} \sigma_{k2} = & \frac{\sqrt{\pi}}{\sqrt{2\pi} r} \operatorname{Re} \left\{ \sum_{\alpha} M_{k\alpha} \frac{1}{\sqrt{\cos \theta + p_{\alpha} \sin \theta}} N_{\alpha n} T_n \right\}, \quad k = 1, 2, 3, \\ (29) \end{aligned}$$

$$D_2 = \frac{\sqrt{\pi}}{\sqrt{2\pi} r} \operatorname{Re} \left\{ \sum_{\alpha} M_{4\alpha} \frac{1}{\sqrt{\cos \theta + p_{\alpha} \sin \theta}} N_{\alpha n} T_n \right\}.$$

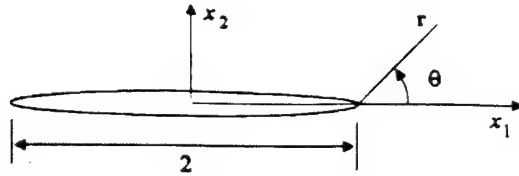


Fig. 2. Coordinate systems.

The square root singularity in r is evident in both stresses and electric displacements. Noting the reciprocal relationship between M and N , we obtain along $\theta = 0$

$$\begin{aligned}\sigma_{12}(\theta = 0) &= \frac{\sqrt{\pi}}{\sqrt{2\pi}r} \sigma_{12}^{\infty}, & \sigma_{22}(\theta = 0) &= \frac{\sqrt{\pi}}{\sqrt{2\pi}r} \sigma_{22}^{\infty}, \\ \sigma_{32}(\theta = 0) &= \frac{\sqrt{\pi}}{\sqrt{2\pi}r} \sigma_{32}^{\infty}, & D_2(\theta = 0) &= \frac{\sqrt{\pi}}{\sqrt{2\pi}r} D_2^{\infty}.\end{aligned}\quad (30)$$

Following the conventional definition, the stress and electric displacement intensity factors are given by

$$K_I = \sqrt{\pi} \sigma_{22}^{\infty}, \quad K_{II} = \sqrt{\pi} \sigma_{12}^{\infty}, \quad K_{III} = \sqrt{\pi} \sigma_{32}^{\infty}, \quad \text{and} \quad K_{IV} = \sqrt{\pi} D_2^{\infty}, \quad (31)$$

respectively. These intensity factors have been derived by Suo et al. [7]. It is interesting to note that along this plane, $\theta = 0$, the stress and electric fields are not coupled. In other words, the electric field alone cannot produce mechanical stresses in the crack plane ahead of the crack tip. Consequently, if the stress intensity factor is used to determine crack instability, the electric field should have no effect. Such a conclusion would contradict experimental findings [12, 13, 14].

To examine the possibility of change of crack propagation direction, the tangential stress, $\sigma_{\theta\theta}$, near the crack tip is investigated using the near tip solution. Mode I fracture of a PZT-4 medium is considered. The material constants for PZT-4 piezoelectric ceramic are listed in the Appendix. It is noted that material axes and analysis axes were denoted as X_1, X_2, X_3 and x_1, x_2, x_3 , respectively. In this case, for mode I, $X_2 - X_3$ is assigned to $x_1 - x_2$ coordinate in analysis. Figure 3 shows the tangential stress variation as a function of θ at a constant value of r for pure electrical or mechanical loading. Figure 4 shows the results for mixed loadings. It is evident that maximum tangential stress may occur at some angle from the crack plane under strong electric fields. This implies that crack propagation may deviate from its original plane even though mode I loadings are applied. This crack skewing mechanism is consistent with the experimental observation by McHenry and Koepke [12].

4. Mechanical strain energy release rate

Total potential energy release rate that includes mechanical and electrical energies during crack extension has been derived for use as a fracture criterion for piezoelectric materials

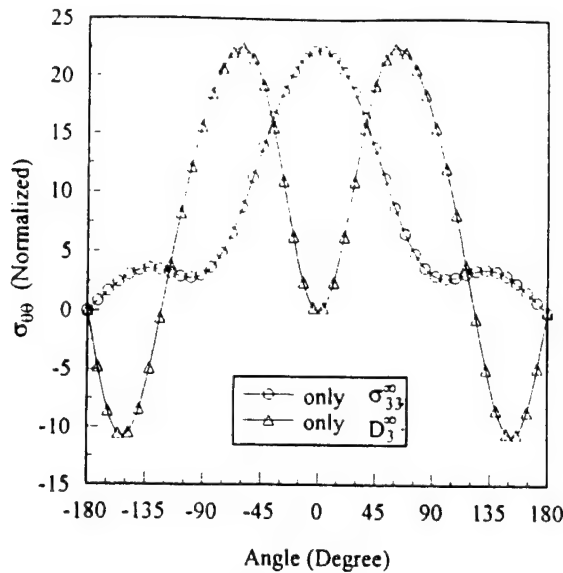


Fig. 3. Characteristics of tangential stresses at crack tip under pure electrical and mechanical loading.

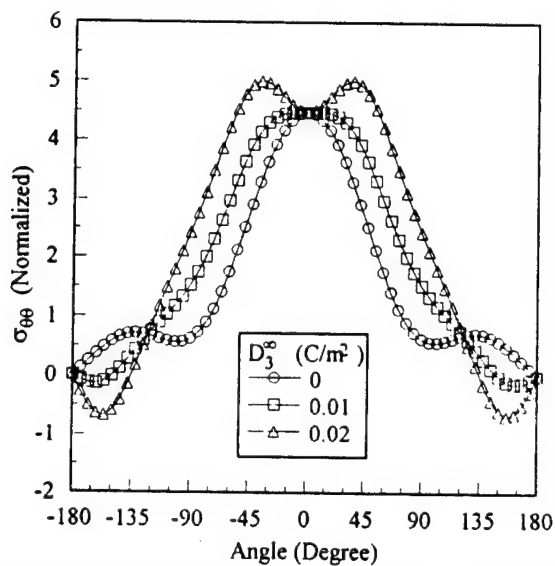


Fig. 4. Characteristics of tangential stresses at crack tip under mixed loading.

[4, 7, 8]. When used as the fracture criterion, this quantity failed to predict the effect of the electric field on the fracture of piezoelectric materials. In fact, if it assumes that fracture occurs when the total potential energy release rate reaches the critical value, it shows that the electric field always impedes crack growth in contradiction to the experimental evidence [12, 14].

Since fracture is a mechanical process, it may be more suitable to consider the mechanical strain energy release rate as the fracture criterion. The strain energy release rate can be calculated by the crack closure integral [20] as

$$G^M = \lim_{\delta \rightarrow 0} \frac{1}{\delta} \int_0^\delta \sigma_{i2}(x) u_i(\delta - x) dx, \quad (32)$$

where δ is the assumed crack extension. Using the general solutions given by (24–27), the mechanical strain energy release rates for all three modes of fracture can be calculated using the crack closure integral.

The crack opening displacements, Δu_k , can be written as

$$\Delta u_k = -2\sqrt{1-x_1^2} \operatorname{Im}(A_{k\alpha} N_{\alpha J}) T_J, \quad -1 \leq x_1 \leq 1. \quad (33)$$

Let $-x_1 = \xi$. Near the right crack tip, ξ is small and Δu_k becomes

$$\Delta u_k = -2\sqrt{2\xi} \operatorname{Im}(A_{k\alpha} N_{\alpha J}) T_J. \quad (34)$$

Using (29), (32), and (34), the strain energy release rate is obtained as

$$G^M = -\frac{1}{2}\pi T_i \operatorname{Im}(A_{i\alpha} N_{\alpha J}) T_J. \quad (35)$$

For comparison, the total energy release rate is also presented. We have

$$J = \int_{\Gamma} [H n_1 - \sigma_{ij} n_j u_{i,1} + D_i E_1 n_i] d\Gamma, \quad (36)$$

where $H = \frac{1}{2}c_{ijkl}s_{ij}s_{kl} - \frac{1}{2}\varepsilon_{ij}E_iE_j - e_{ikl}s_{kl}E_i$ is the electric enthalpy and s_{ij} indicates the strain tensor; Γ is an integration contour beginning at the lower crack surface and ending at the upper surface, and n is the unit normal vector to the contour. Similar to the J -integral for elastic materials [21], (36) can be shown to be path independent and equal to the crack closure integral, i.e.

$$J = G = \lim_{\delta \rightarrow 0} \frac{1}{\delta} \int_0^\delta \{\sigma_{i2}(x) u_i(\delta - x) + D_i(x) \phi_i(\delta - x)\} dx, \quad (37)$$

where G is the total energy release rate.

For convenience, we now use the principal material axes, X_1, X_2, X_3 , for PZT-4 as the coordinate system in the crack problem. The loadings for the three modes of fracture are depicted in Fig. 5. To use the solutions given in the previous section, the coordinates must be properly interpreted. For PZT-4 piezoelectric ceramics whose material constants are listed in the Appendix, the mechanical strain energy release rates (G^M) and the total energy release rates (G) for each mode of fracture are obtained as

$$\begin{aligned} G_I^M &= \frac{1}{2}\pi(1.48 \times 10^{-11} \sigma_{33}^{\infty 2} + 2.67 \times 10^{-2} \sigma_{33}^{\infty} D_3^{\infty}), \\ G_{II}^M &= \frac{1}{2}\pi(1.10 \times 10^{-11} \sigma_{13}^{\infty 2} + 2.59 \times 10^{-2} \sigma_{13}^{\infty} D_1^{\infty}), \\ G_{III}^M &= \frac{\pi}{2(c_{44}\varepsilon_{11} + e_{15}^2)}(\varepsilon_{11}\sigma_{23}^{\infty 2} + e_{15}\sigma_{23}^{\infty} D_2^{\infty}) \end{aligned} \quad (38)$$

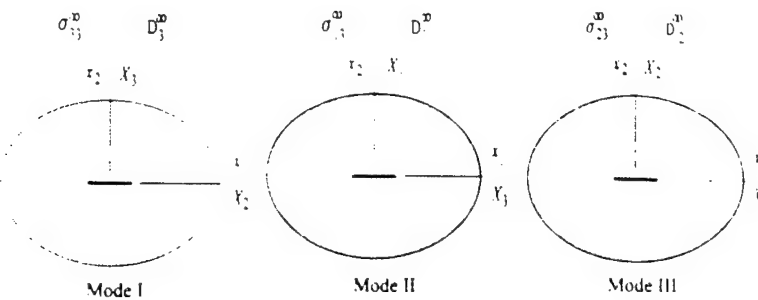


Fig. 5. Alignment of principal material axes for each mode of fracture.

$$= \frac{1}{2}\pi(1.80 \times 10^{-11}\sigma_{23}^{\infty 2} + 4.02 \times 10^{-2}\sigma_{23}^{\infty}D_2^{\infty}).$$

and

$$\begin{aligned} G_{\text{II}} &= \frac{1}{2}\pi[1.48 \times 10^{-11}\sigma_{33}^{\infty 2} + 2(2.67 \times 10^{-2}\sigma_{33}^{\infty}D_3^{\infty}) - 8.56 \times 10^7D_3^{\infty 2}], \\ G_{\text{III}} &= \frac{1}{2}\pi[1.10 \times 10^{-11}\sigma_{13}^{\infty 2} + 2(2.59 \times 10^{-2}\sigma_{13}^{\infty}D_1^{\infty}) - 1.14 \times 10^8D_1^{\infty 2}], \\ G_{\text{III}} &= \frac{\pi}{2(c_{44}\varepsilon_{11} + \varepsilon_{15}^2)}[\varepsilon_{11}\sigma_{23}^{\infty 2} + 2(e_{15}\sigma_{23}^{\infty}D_2^{\infty}) - c_{44}D_2^{\infty 2}] \\ &= \frac{1}{2}\pi[1.80 \times 10^{-11}\sigma_{23}^{\infty 2} + 2(4.02 \times 10^{-2}\sigma_{23}^{\infty}D_2^{\infty}) - 7.66 \times 10^7D_2^{\infty 2}], \end{aligned} \quad (39)$$

respectively.

The difference between the mechanical strain energy release rate and the total energy release rate is obvious. Note that the electrical energy term in G is always negative. Thus, it is possible to produce a negative energy release rate in the absence of mechanical loading or if the mechanical loading is small. On the other hand, the dependence of G^M on the electric displacement is linear. Thus, the electric field can add or subtract from the strain energy release rate depending on the electric loading direction.

In Fig. 6, the strain energy release rates for three different mode I electric loadings, $D_3^{\infty} = -2.0, 0.0$ and $2.0(\times 10^{-4}C/m^2)$, are shown. For the negative electric displacement, $D_3^{\infty} = -2.0(\times 10^{-4}C/m^2)$, the mechanical strain energy release rate becomes negative for $\sigma_{33}^{\infty} \leq 0.36(\text{MPa})$. Thus for loading $D_3^{\infty} = -2.0(\times 10^{-4}C/m^2)$ and $\sigma_{33}^{\infty} \leq 0.36(\text{MPa})$, the realistic mechanical strain energy release rate should be zero because the crack surfaces are in contact. A similar argument leads to the conclusion that $G_I^M = 0$ for $D_3^{\infty} = 0$ and $\sigma_{33}^{\infty} \leq 0$. In the case $D_3^{\infty} = 2.0(\times 10^{-4}C/m^2)$, the strain energy release rate becomes negative in the region $-0.36 \leq \sigma_{33}^{\infty} \leq 0(\text{MPa})$. However, crack surfaces are in contact only for $\sigma_{33}^{\infty} \leq -0.36(\text{MPa})$. Thus, G_I^M should be set equal to zero for applied stress less than $-0.36(\text{MPa})$.

Figure 7 shows the variations of the strain energy release rate for mode I plotted with varying electric loading for constant mechanical loadings. Since electric loading alone does not produce stresses in the $\theta = 0^\circ$ plane, the strain energy release rate is zero if the remote applied stress is absent. Due to the closure of crack surfaces, G_I^M should be set equal to zero when it becomes negative.

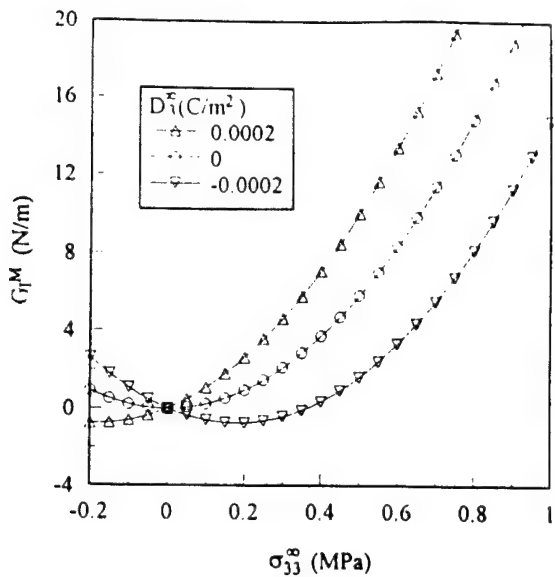
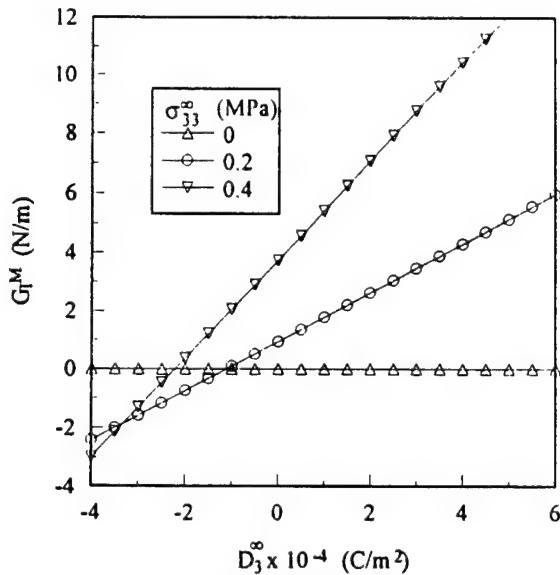
Fig. 6. G_1^M (N/m) under a constant electric loading D_3^∞ (C/m^2).Fig. 7. G_1^M (N/m) under a constant mechanical loading σ_{33}^∞ (MPa).

Figure 8 presents the result of mode III under three different constant electric loadings. In this case, the variations of G_{III}^M for positive and negative electric loadings with respect to the applied shear stress, respectively, are identical since crack surfaces can be displaced in either direction. Although it is not presented here, mode II shows a behavior similar to mode III. In the mode III case, since the crack surfaces can be displaced in both directions, the mechanical strain energy release rate can become negative for certain combinations of mechanical and electrical loadings. Figure 9 presents the results for three different mechanical

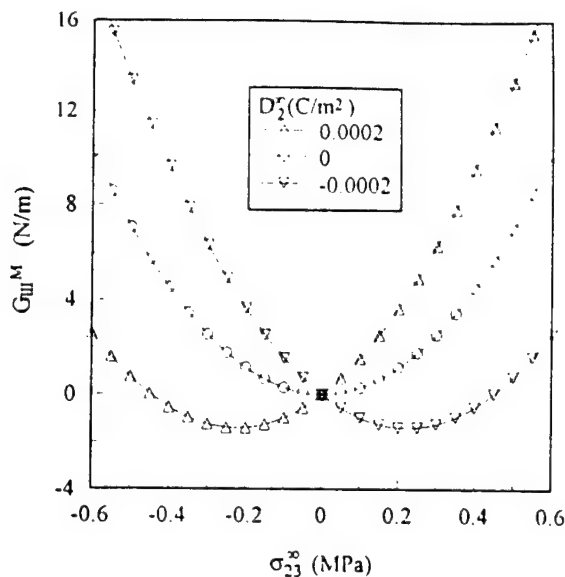


Fig. 8. G_{III}^M (N/m) under a constant electric loading D_2^∞ (C/m^2).

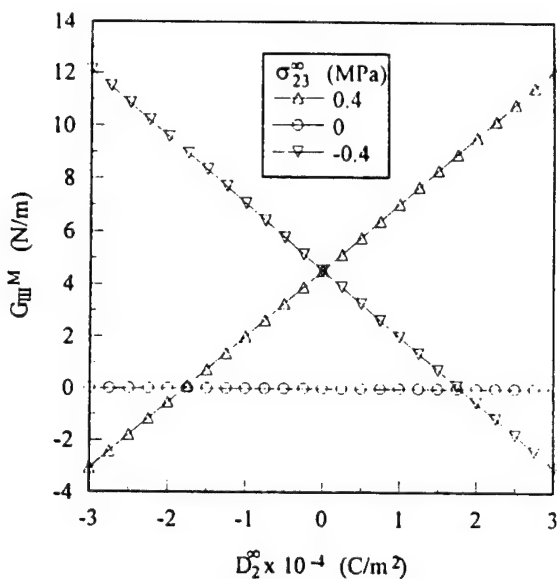


Fig. 9. G_{III}^M (N/m) under a constant mechanical loading σ_{23}^∞ (MPa).

loadings, $\sigma_{23}^\infty = -0.4, 0, 0, 0.4$ (MPa). Similar to the mode I case, the mechanical strain energy release rate vanishes without applied mechanical loading.

Figure 10 shows the comparison between the mode III total energy release rate (G_{III}) and the mechanical strain energy release rate (G_{III}^M) for varying electric field E_2^∞ . The total energy release rate indicates that the existence of electric fields always retards crack propagation regardless of the direction of the electric field applied. On the other hand, the strain energy release rate predicts that crack propagation can either be enhanced or retarded depending on the direction of the electric field.

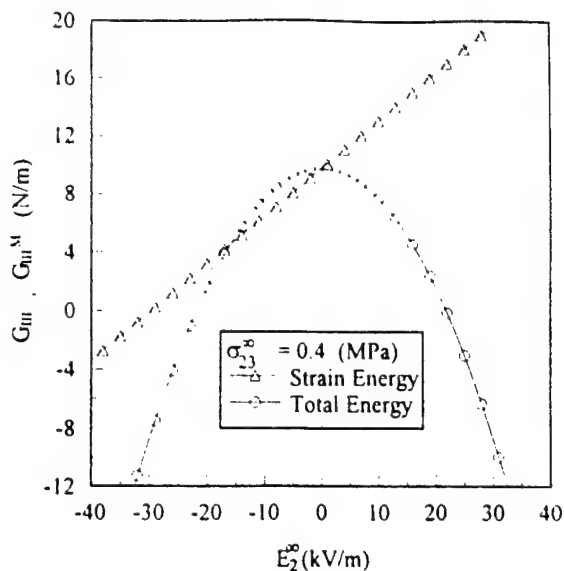


Fig. 10. Comparison between the total energy release rate (G_{III}) and the mechanical strain energy release rate (G_{III}^M) versus electric field under a constant mechanical loading $\sigma_{23}^{\infty} = 0.4$ (MPa).

5. Conclusions

Closed form solutions for all three modes of fracture were obtained for infinite piezoelectric materials containing a plane crack. The stress intensity factors and electric displacement factor defined in the conventional manner were found to be unsuitable for predicting crack instability under combined mechanical and electrical loading. Using the stress intensity factor alone as the fracture criterion, electrical loading would have no effect on fracture of the material.

Explicit expressions of the total potential energy release rate (including mechanical and electrical energies) and the mechanical strain energy release rate (including only mechanical energy) were derived for the PZT-4 piezoelectric ceramic for all three modes of fracture. The mechanical strain energy release rate is linearly dependent on the electric displacement implying that the strain energy release rate may increase or decrease depending on the electric loading direction. This result agrees qualitatively with the existing experimental observations. In contrast, the total energy release rate always decreases as the strength of the electric loading increases either in the positive or negative direction. Thus, the total energy release rate cannot be used directly as a fracture criterion for piezoelectric materials.

It is noted that analyses performed in this work are based on linear piezoelectricity. Singular behavior of stresses and the electric field near the crack tip may affect fracture behavior possibly through dielectric breakdown, local depoling and domain reversal although these activities are confined in a small region near the crack tip. Thus, the present linear piezoelectricity solution should be viewed in the same spirit as small scale yielding approximation adopted in linear elastic fracture mechanics.

Acknowledgment

This work was supported by AFOSR through grant F-49620-92-J-0457 to Purdue University. Drs. C.I. Jim Chang and Walter Jones were monitors of this program.

Appendix

Let X_3 be parallel to the poling direction. The constitutive relations for PZT-4 piezoelectric ceramic in contracted notations are given by

$$\begin{aligned} \left\{ \begin{array}{l} \sigma_{11} \\ \sigma_{22} \\ \sigma_{33} \\ \sigma_{23} \\ \sigma_{31} \\ \sigma_{12} \end{array} \right\} &= \left[\begin{array}{cccccc} c_{11} & c_{12} & c_{13} & 0 & 0 & 0 \\ c_{12} & c_{11} & c_{13} & 0 & 0 & 0 \\ c_{13} & c_{13} & c_{33} & 0 & 0 & 0 \\ 0 & 0 & 0 & c_{44} & 0 & 0 \\ 0 & 0 & 0 & 0 & c_{44} & 0 \\ 0 & 0 & 0 & 0 & 0 & (c_{11} - c_{12})/2 \end{array} \right] \left\{ \begin{array}{l} s_{11} \\ s_{22} \\ s_{33} \\ 2s_{23} \\ 2s_{31} \\ 2s_{12} \end{array} \right\} \\ &- \left[\begin{array}{ccc} 0 & 0 & \epsilon_{31} \\ 0 & 0 & \epsilon_{31} \\ 0 & 0 & \epsilon_{33} \\ 0 & \epsilon_{15} & 0 \\ \epsilon_{15} & 0 & 0 \\ 0 & 0 & 0 \end{array} \right] \left\{ \begin{array}{l} E_1 \\ E_2 \\ E_3 \end{array} \right\}, \\ \left\{ \begin{array}{l} D_1 \\ D_2 \\ D_3 \end{array} \right\} &= \left[\begin{array}{cccccc} 0 & 0 & 0 & 0 & \epsilon_{15} & 0 \\ 0 & 0 & 0 & \epsilon_{15} & 0 & 0 \\ \epsilon_{31} & \epsilon_{31} & \epsilon_{33} & 0 & 0 & 0 \end{array} \right] \left\{ \begin{array}{l} s_{11} \\ s_{22} \\ s_{33} \\ 2s_{23} \\ 2s_{31} \\ 2s_{12} \end{array} \right\} + \left[\begin{array}{ccc} \epsilon_{11} & 0 & 0 \\ 0 & \epsilon_{11} & 0 \\ 0 & 0 & \epsilon_{33} \end{array} \right] \left\{ \begin{array}{l} E_1 \\ E_2 \\ E_3 \end{array} \right\}, \end{aligned}$$

where

$$\begin{aligned} c_{11} &= 13.9 \times 10^{10} (N/m^2), & c_{12} &= 7.78 \times 10^{10} (N/m^2), & c_{13} &= 7.43 \times 10^{10} (N/m^2) \\ c_{33} &= 11.3 \times 10^{10} (N/m^2), & c_{44} &= 2.56 \times 10^{10} (N/m^2) \\ \epsilon_{31} &= -6.98 (C/m^2), & \epsilon_{33} &= 13.84 (C/m^2), & \epsilon_{15} &= 13.44 (C/m^2) \\ \epsilon_{11} &= 6.00 \times 10^{-9} (C/Vm), & \epsilon_{33} &= 5.47 \times 10^{-9} (C/Vm). \end{aligned}$$

References

1. V.Z. Parton, *Acta Astronautica* 3 (1976) 671–683.
2. R.M. McMeeking, *International Journal of Engineering Science* 28 (1990) 605–613.
3. V.Z. Parton and B.A. Kudryavtsev, *Electromagnetoelasticity*, Gordon and Breach Science Publishers, New York (1988).
4. Y.E. Pak, *Journal of Applied Mechanics* 57 (1990) 647–653.
5. H.A. Sosa and Y.E. Pak, *International Journal of Solids and Structures* 26 (1990) 1–15.
6. M.L. Williams, *Journal of Applied Mechanics* (1957) 109–114.
7. H.A. Sosa, *International Journal of Solids and Structures* 28 (1991) 491–505.
8. *Ibid.* 29 (1992) 2613–2622.
9. Z. Suo, C.-M. Kuo, D.M. Barnett and J.R. Willis, *Journal of the Mechanics and Physics of Solids* 40 (1992) 739–765.

10. G.P. Cherepanov, *Mechanics of Brittle Fracture*, McGraw-Hill, New York (1979).
11. Y.E. Pak and G. Herrmann, *International Journal of Engineering Science* 24 (1986) 1365-1374.
12. K.D. McHenry and B.G. Koepke, *Fracture Mechanics of Ceramics* 5 (1983) 337-352.
13. R.C. Pohanka and P.L. Smith, *Electronic Ceramics*, Marcel Dekker, New York (1988).
14. A.G. Tobin and Y.E. Pak, *SPIE* 1916 (1993) 78-86.
15. A.N. Stroh, *Philosophical Magazine* 3 (1958) 625-646.
16. A.N. Stroh, *Journal of Mathematics and Physics* 41 (1962) 77-103.
17. D.M. Barnett and J. Lothe, *Physica Status Solidi (b)* 67 (1975) 105.
18. W.F.J. Deeg, Ph.D. thesis, Stanford University (1980).
19. H.F. Tiersten, *Linear Piezoelectric Plate Vibrations*, Plenum Press, New York (1969).
20. G.R. Irwin, *Proceedings 1st Symposium Naval Structural Mechanics* (1960) 557-591.
21. J.R. Rice, *Journal of Applied Mechanics* 35 (1968) 376-389.

Fracture Criteria for Piezoelectric Ceramics

Seungbae Park and Chin-Teh Sun

School of Aeronautics and Astronautics, Purdue University, West Lafayette, Indiana 47907-1282

Fracture criteria for piezoelectric materials were investigated. Mode I and mixed mode fracture tests were performed on PZT-4 piezoelectric ceramics to verify the validity of the mechanical strain energy release rate as a fracture criterion. Experimental results indicated that crack extension could be aided or impeded by an electric field, depending on the field direction. Further, the direction of crack extension was studied. A crack closure method, together with finite element analysis, was introduced to calculate the mechanical strain energy release rate. The maximum mechanical strain energy release rate was used to predict fracture loads under combined mechanical and electrical loads. It was found that the mechanical strain energy release rate criterion is superior to other fracture criteria and predicts fracture loads fairly accurately.

I. Introduction

IN ADAPTIVE structures, piezoelectric ceramics are used as actuators, since they possess strong mechanical-electrical coupling. However, piezoelectric ceramics are very brittle and susceptible to fracture. Moreover, actuation forces may act as crack driving forces. The presence of cracks would degenerate mechanical as well as electrical performances of the actuator.

Mechanical and electrical fields of piezoelectric media containing a crack have been analyzed by several researchers.¹⁻⁵ However, the fracture behavior of piezoelectric media under mechanical and electrical loading is still ambiguous. Specifically, it is not clear whether the electric field impedes or enhances crack propagation. Efforts have been focused on the use of the total energy release rate as a fracture criterion. This criterion indicates that the presence of electric fields always impedes crack propagation. However, all available experimental observation indicates otherwise. Park and Sun⁶ proposed a new fracture criterion based on mechanical strain energy release rate. Since fracture is a mechanical process, it was thought that taking only mechanical strain energy released during crack extension as the fracture criterion is more logical.

Experimental efforts have been made to observe fracture behavior under both mechanical and electrical loadings. McHenry and Koepke⁷ measured crack propagation velocities under electric fields. They observed that electric fields increased crack speed, and crack propagation deviated from its original direction under a strong electric field. Tobin and Pak⁸ performed Vickers indentation tests and found that the apparent fracture toughness (K_{IC}) of the material was reduced or increased, depending on the direction of the applied electric field.

In this study, possible fracture criteria for piezoelectric ceramics, namely, the stress intensity factor, the total energy release rate and the mechanical strain energy release rate, are presented, and the suitability of each criterion is discussed. Mode I fracture experiments were conducted to verify the mechanical strain energy release rate using PZT-4 piezoelectric ceramic compact tension specimens. The results indicate that an electric field can either aid or retard crack propagation. A

crack closure method in conjunction with the finite element analysis is employed to calculate the mechanical strain energy release rate. The maximum mechanical strain energy release rate is used to predict the fracture loads under combined mechanical and electrical loads. Also, mixed mode fracture tests using unsymmetric three-point bending were performed. The direction of initial crack growth was investigated based on the direction of maximum mechanical strain energy release rate.

II. Possible Fracture Criteria

Using Stroh formulation,^{9,10} Park and Sun⁶ obtained closed-form solutions explicitly for all three modes of fracture for an infinite piezoelectric medium containing a center crack with electrically insulated surfaces.

From the solution obtained by Park and Sun,⁶ the near tip stresses and electric displacement for Mode I and Mode II are expressed in polar coordinates originated at the right crack tip (see Fig. 1) as

$$\sigma_{k3} = \frac{\sqrt{\pi a}}{\sqrt{2\pi r}} \operatorname{Re} \left\{ \sum_{\alpha}^3 M_{1(k-1)\alpha} \frac{1}{\sqrt{\cos \theta + p_{\alpha} \sin \theta}} N_{\alpha n} T_n \right\} \quad (k = 2, 3; \quad n = 1, 2, 3)$$

$$D_3 = \frac{\sqrt{\pi a}}{\sqrt{2\pi r}} \operatorname{Re} \left\{ \sum_{\alpha}^3 M_{3\alpha} \frac{1}{\sqrt{\cos \theta + p_{\alpha} \sin \theta}} N_{\alpha n} T_n \right\} \quad (1)$$

where $\mathbf{T} = \{\sigma_{23}^x, \sigma_{33}^x, D_3^x\}^T$ represents remote mechanical and electrical loadings, a is half crack length, p_{α} are eigenvalues of a characteristic equation, and \mathbf{M} and \mathbf{N} are coefficient matrices with inverse relations to each other.

Using the conventionally defined stress intensity factors and electric displacement intensity factor, stresses and electric displacement at the crack tip in the crack plane, $\theta = 0^\circ$, are given by

$$\sigma_{23} = \frac{K_{II}}{\sqrt{2\pi r}} \quad \sigma_{33} = \frac{K_I}{\sqrt{2\pi r}} \quad D_3 = \frac{K_W}{\sqrt{2\pi r}} \quad (2)$$

where

$$K_I = \sqrt{\pi a} \sigma_{33}^x \quad K_{II} = \sqrt{\pi a} \sigma_{23}^x \quad K_W = \sqrt{\pi a} D_3^x$$

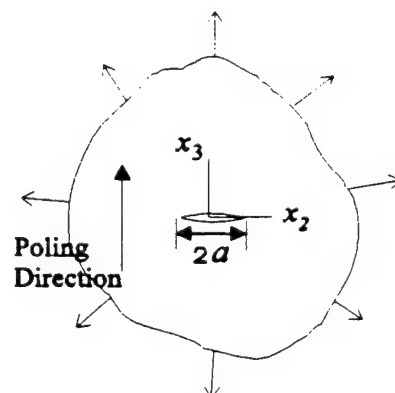


Fig. 1. Infinite piezoelectric medium containing a center crack with far-field loading.

S. M. Wiederhorn—contributing editor

Manuscript No. 193062. Received November 8, 1994; approved January 16, 1995. Supported by the Air Force Office of Scientific Research through Grant No. AFOSR-92-J-0457 to Purdue University, monitored by Drs. C. I. Jim Chang and Walter Jones.

Table I. Material Constants for PZT-4 Piezoelectric Ceramics

Elastic constants (N/m ²)				
C_{11}	C_{12}	C_{13}	C_{31}	C_{44}
13.9×10^{10}	7.78×10^{10}	7.43×10^{10}	11.3×10^{10}	2.56×10^{10}
Piezoelectric constants (C/m ²)				
e_{31}	e_{33}	e_{15}	ϵ_{11}	ϵ_{33}
-6.98	13.84	13.44	6.00×10^{-9}	5.47×10^{-9}

It is noted that stresses and electric displacement are uncoupled in this plane. This indicates that the electric loading alone cannot produce mechanical stress in the crack plane ahead of the crack tip and vice versa. If the stress intensity factor is used as a fracture criterion, the effect of the electric field cannot be accounted for. This leads us to conclude that stress intensity factor is not suitable as a fracture criterion for piezoelectric materials.

Another fracture criterion for piezoelectric materials is based on the total energy release rate. The total energy release rate (J) is derived in parallel with the path-independent J integral for elastic materials. It includes mechanical and electrical energies released as the crack propagates and is given by

$$J = \int_{\Gamma} [Hn_2 - \sigma_{ii}n_iu_{i,2} + D_iE_3n_i] d\Gamma \quad (i, j = 2, 3) \quad (3)$$

where $H = \frac{1}{2}c_{ijkl}s_{ij}s_{kl} - \frac{1}{2}\epsilon_{ij}E_iE_j - e_{iij}s_{ij}E_i$ is the electric enthalpy, Γ is an integration contour around the crack tip, \mathbf{n} is the unit normal vector to the contour, σ_{ij} , s_{ij} , and E_i represent stresses, strains, and electric fields, respectively, and c_{ijkl} , e_{iij} , and ϵ_{ij} represent elastic constants, piezoelectric constants, and dielectric permittivities, respectively. It is noted that the J integral given by Eq. (3) is also path-independent. Alternatively, J can be obtained by using the crack closure integral as⁶

$$J = G = \lim_{\delta \rightarrow 0} \frac{1}{2\delta} \int_0^{\delta} [\sigma_{ii}(x_2)\Delta u_i(\delta - x_2) + D_i(x_2)\Delta\phi(\delta - x_2)] dx_2 \quad (i = 2, 3) \quad (4)$$

where δ is the assumed crack extension and u_i and ϕ are displacements and electric potential, respectively.

Considering the mechanical process of fracture, Park and Sun⁶ proposed using the mechanical strain energy release rate as the fracture criterion for piezoelectric materials. The mechanical strain energy release rate includes only mechanical energy released as the crack extends. The mechanical strain energy release rate is defined by the mechanical part of the crack closure integral as

Mode I:

$$G_1^M = \lim_{\delta \rightarrow 0} \frac{1}{2\delta} \int_0^{\delta} \sigma_{33}(x_2)\Delta u_3(\delta - x_2) dx_2 \quad (5a)$$

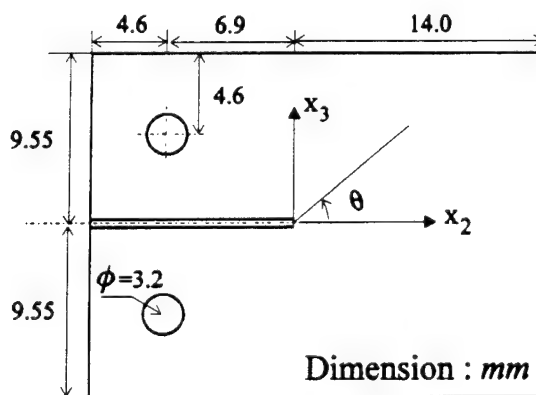


Fig. 2. Compact tension specimen, PZT-4

Mode II:

$$G_0^M = \lim_{\delta \rightarrow 0} \frac{1}{2\delta} \int_0^{\delta} \sigma_{23}(x_2)\Delta u_2(\delta - x_2) dx_2 \quad (5b)$$

Consider an infinite piezoelectric ceramic containing a center crack and subjected to Mode I remote loadings. As an example, material properties of PZT-4 piezoelectric ceramic were used. The poling direction is assumed to be parallel to the x_3 -axis. The mechanical strain energy release rate (G_1^M) and the total energy release rate (G_1) are obtained as⁶

$$G_1^M = \frac{\pi a}{2} (1.48 \times 10^{-11} \sigma_{33}^{z^2} + 2.67 \times 10^{-2} \sigma_{33}^{z^2} D_3^z) \quad (\text{N/m})$$

$$G_1 = \frac{\pi a}{2} [1.48 \times 10^{-11} \sigma_{33}^{z^2} + 2(2.67 \times 10^{-2} \sigma_{33}^{z^2} D_3^z) - 8.56 \times 10^7 D_3^{z^2}] \quad (\text{N/m}) \quad (6)$$

or

$$G_1^M = \frac{\pi a}{2} (2.12 \times 10^{-11} \sigma_{33}^{z^2} + 2.67 \times 10^{-10} \sigma_{33}^{z^2} E_3^z) \quad (\text{N/m})$$

$$G_1 = \frac{\pi a}{2} (2.76 \times 10^{-11} \sigma_{33}^{z^2} + 1.23 \times 10^{-10} \sigma_{33}^{z^2} E_3^z - 8.56 \times 10^{-9} E_3^{z^2}) \quad (\text{N/m}) \quad (7)$$

The result indicates that the mechanical strain energy release rate may be increased or decreased, depending on the direction of electric loading, implying that crack propagation may be enhanced or retarded. However, the total energy release rate is always negative in the absence of mechanical loading. Moreover, the presence of a strong electric loading always reduces the total energy release rate, implying that electric loading always impedes crack propagation. It is noted that these interpretations of the results are based on linear piezoelectricity and there may exist factors beyond the scope of linear piezoelectricity that would affect fracture through the singular behavior of stresses and the electric field near the crack tip such as dielectric breakdown and local depoling.

III. Experiment

Mode I and mixed mode fracture tests for PZT-4 piezoelectric ceramic were performed. The purpose of these tests was to verify the validity of the mechanical strain energy release rate

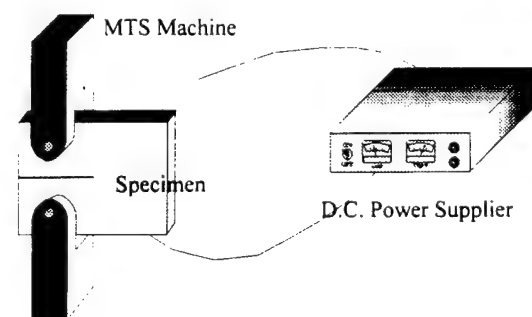


Fig. 3. Test setup for Mode I fracture test using compact tension specimens.

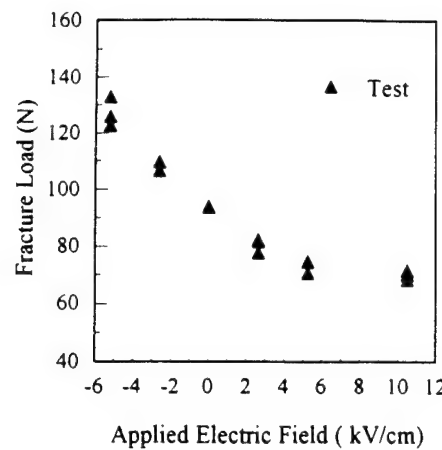


Fig. 4. Fracture loads under various electric fields for compact tension specimens.

as a fracture criterion for piezoelectric ceramics. Attention was focused on the effect of electric fields on fracture.

(1) Mode I Fracture

The specimen was commercially supplied PZT-4. It was obtained as poled with dimensions of 25.4 mm \times 19.1 mm \times 5.1 mm. Poling was done along the axis of the 19.1 mm dimension, and electrodes were coated in silver on top and bottom surfaces. Material properties for PZT-4 are listed in Table I. The side surfaces of the specimen were polished with 9 μm grain size diamond abrasive. Subsequently, compact tension specimens were made with the dimensions shown in Fig. 2. The crack was created by cutting with a 0.46 mm thick diamond wheel perpendicular to the poling direction in a depth of 10.5 mm. To better approximate an ideal crack, the crack tip was further cut by a sharp razor blade with diamond abrasive, resulting in a final crack length of 11.5 mm.

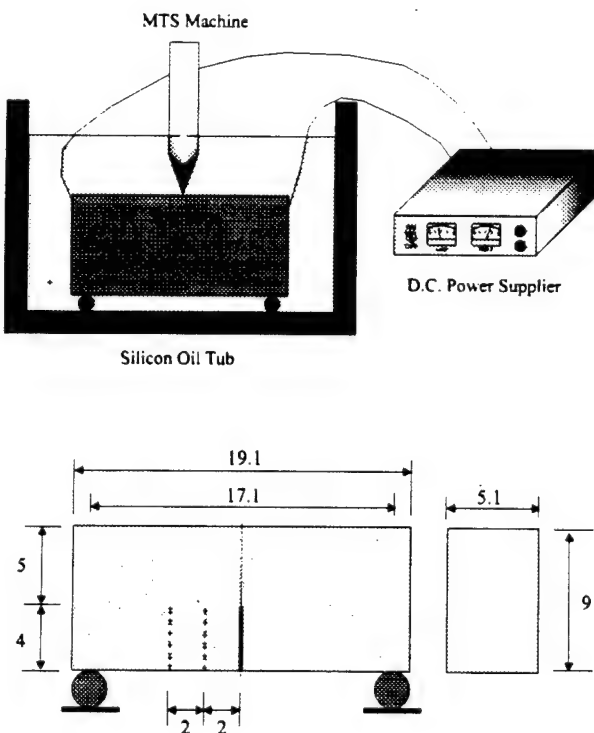


Fig. 5. Experimental setup and dimensions of specimen for mixed mode fracture test.

Figures 2 and 3 depict the specimen and setup for the experiment, respectively. The procedure of testing was to increase the tensile load under a certain electric field until fracture occurred. To generate electric fields, a power supplier which can produce up to 50 kV in dc was used. Mechanical loading was applied by the crosshead displacement control of the MTS machine. The crosshead speed was 0.0013 mm/s. During initial exploratory tests, electric discharging between electrodes through the air was observed when the electric field exceeded 5 kV/cm. To prevent this and to enforce an insulated crack surface boundary condition, the specimen was immersed in a tub filled with silicone oil.

Figure 4 shows the fracture initiation loads under different electric fields obtained from the experiment. It is evident that the electric field significantly affects the fracture load. Moreover, positive electric fields, which tend to open the crack, reduce the fracture load, while negative electric fields increase it.

Using a Vickers diamond indenter, Tobin and Pak⁸ performed indentation tests on PZT-8 specimens and found that a positive electric field would reduce the apparent fracture toughness (K_{Ic}) of a crack perpendicular to the poling direction. On the other hand, a negative field would increase apparent toughness. Their observation is consistent with the present results.

(2) Mixed Mode Fracture

Most mixed mode fracture experiments were performed using oblique crack specimens. Due to the limitation of the size of piezoelectric ceramics, it is difficult to make the oblique crack specimen an experimental model. The symmetric three-point bend specimen has been used extensively in obtaining Mode I plane strain fracture toughness, K_{Ic} . The three-point bend specimen with an unsymmetrical crack was adopted for mixed mode fracture.

Specimens were cut to 19.1 mm \times 9 mm \times 5.1 mm dimension, and poling direction was placed along the 19.1 mm dimension. Surfaces of the specimen were polished with 9 μm grain size diamond abrasive paste. Cracks were introduced using a 0.46 mm thick diamond wheel cutter at three different locations, i.e., the midspan, 2 mm, and 4 mm from the midspan. As was done in preparing the Mode I compact tension specimen, the crack tip was refined further by a razor blade with diamond abrasive paste. The final depth of the crack was 4 mm.

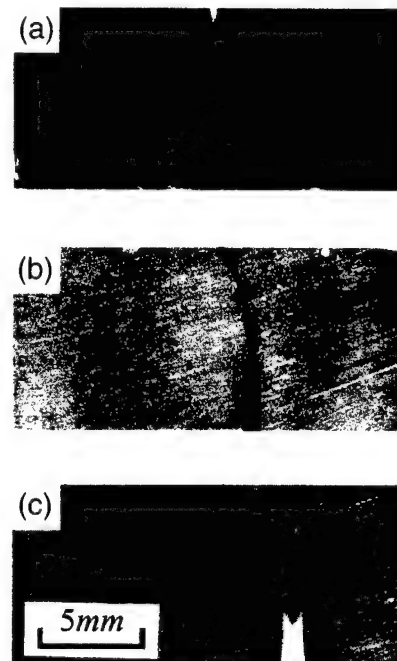


Fig. 6. Typical fracture paths for the three different crack locations in the three-point bending test under 5 kV/cm: (a) center crack, (b) 2 mm off-center, and (c) 4 mm off-center crack.

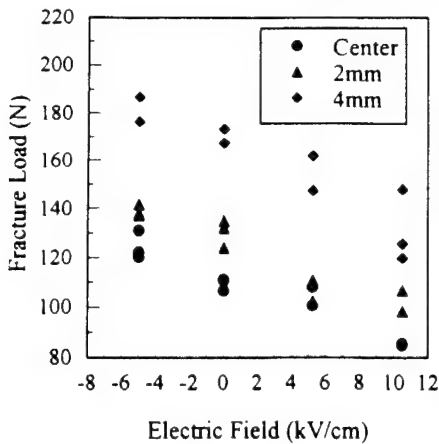


Fig. 7. Fracture loads for various crack locations and electric fields in the unsymmetric three-point bending test.

Figure 5 shows the three-point bend setup and specimen. It is noted that the poling direction is parallel to the span of the bending setup. The prepared specimen was placed on the silicone oil tub which was mounted on the MTS machine. The entire setup including indenter was made of Plexiglas to avoid electric discharging. Critical loads which caused fracture were measured for each set of specimens for various electric fields. For each electric field and crack location, three tests were performed.

Figure 6 shows typical fractured specimens under the electric field of 5 kV/cm. Figure 7 presents fracture initiation loads for various electric fields. Center-cracked specimens produced Mode I fracture and exhibited the same fracture behavior as the compact tension specimens. Specifically, positive electric fields decreased fracture load, whereas negative electric fields increased it. The specimens with an off-center crack also exhibited the same trend.

IV. Finite Element Analysis

In the experiments, fracture loads were measured. To determine the corresponding energy release rate, we resorted to finite element analysis. Four-node multifield plane elements in ANSYS¹¹ were used in the analysis. The mechanical strain energy release rate was calculated using the modified crack closure method.¹²⁻¹⁴ The concept of the crack closure integral is that if a crack extends by a small amount Δa , the energy released in the process is equal to the work required to close the crack to its original length.

Figure 8 illustrates the finite element mesh near the crack tip. Let the internal nodal forces at node (d) contributed jointly by elements 1 and 2 be denoted by $F_2^{(d)}$ and $F_3^{(d)}$, and the nodal displacements at node (b) and (c) be $u_2^{(b)}, u_3^{(b)}$ and $u_2^{(c)}, u_3^{(c)}$, respectively. The work done for crack closure in a mixed mode problem can be obtained as

$$G^M = G_I^M + G_{II}^M = \frac{1}{2\Delta a} [F_2^{(d)}(u_3^{(c)} - u_3^{(b)}) + F_3^{(d)}(u_2^{(c)} - u_2^{(b)})] \quad (8)$$

Similarly, the total energy release rate can be obtained by adding the electrical crack closure energy to the mechanical strain energy release rate. We have

$$G = G^M + \frac{1}{2\Delta a} [Q^{(d)}(\phi^{(c)} - \phi^{(b)})] \quad (9)$$

where $Q^{(d)}$ is the nodal charge of elements 1 and 2 at node (d).

It is obvious from Eqs. (8) and (9) that nodal forces, displacements, electric charges, and potentials are needed in the finite element analysis. However, ANSYS does not provide the nodal charge, Q , as an output option. For the calculation of nodal forces, F , and charges, Q , used in Eqs. (8) and (9), the stiffness matrix for an element was obtained as¹⁵

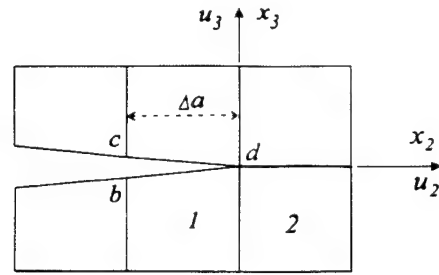


Fig. 8. Finite element mesh for the crack closure integral.

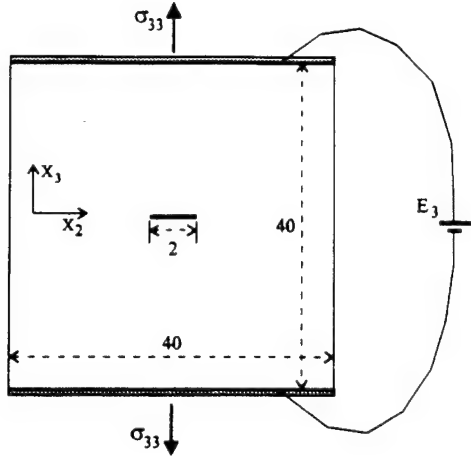


Fig. 9. Finite element model for a piezoelectric medium containing a center crack under both mechanical and electrical loading.

$$\begin{bmatrix} \mathbf{K}_{uu} & \mathbf{K}_{u\phi} \\ \mathbf{K}_{\phi u} & \mathbf{K}_{\phi\phi} \end{bmatrix} \begin{bmatrix} \mathbf{u} \\ \phi \end{bmatrix} = \begin{bmatrix} \mathbf{F} \\ \mathbf{Q} \end{bmatrix} \quad (10)$$

where \mathbf{u} and ϕ are nodal displacements and potentials, respectively, and

$$\begin{aligned} \mathbf{K}_{uu} &= \int_V \mathbf{A}_u^T \mathbf{c} \mathbf{A}_u \, dV & \mathbf{K}_{\phi\phi} &= \int_V \mathbf{A}_\phi^T \mathbf{e}^T \mathbf{A}_\phi \, dV \\ \mathbf{K}_{\phi u} &= \int_V \mathbf{A}_\phi^T \mathbf{e} \mathbf{A}_u \, dV & \mathbf{K}_{u\phi} &= \int_V \mathbf{A}_u^T \mathbf{e} \mathbf{A}_\phi \, dV \end{aligned} \quad (11)$$

in which \mathbf{c} , \mathbf{e} , and $\mathbf{\epsilon}$ denote elastic constants, piezoelectric constants, and dielectric permittivities, respectively, and

$$\mathbf{A}_u = \begin{bmatrix} \frac{\partial N_i}{\partial x} & 0 \\ 0 & \frac{\partial N_i}{\partial y} \\ \frac{\partial N_i}{\partial y} & \frac{\partial N_i}{\partial x} \end{bmatrix} \quad \mathbf{A}_\phi = - \begin{bmatrix} \frac{\partial N_i}{\partial x} \\ \frac{\partial N_i}{\partial y} \end{bmatrix} \quad (12)$$

where N_i are interpolation functions.

From the finite element analysis, the nodal displacements, \mathbf{u} , and the electric potentials, ϕ , are obtained. Equation (10) yields the nodal forces and charge for each element from which the quantities needed in Eqs. (8) and (9) are obtained.

An example finite element analysis was performed to verify the validity of the modified crack closure method in calculating the mechanical strain energy release rate for piezoelectric materials under combined loading. The example considered was a finite center-cracked piezoelectric medium with both mechanical and electrical loadings for Mode I fracture. The finite element mesh, specimen dimensions, and loading conditions are shown in Fig. 9. It is noted that the lateral dimensions of the medium are much larger than the crack size. Thus, the near tip

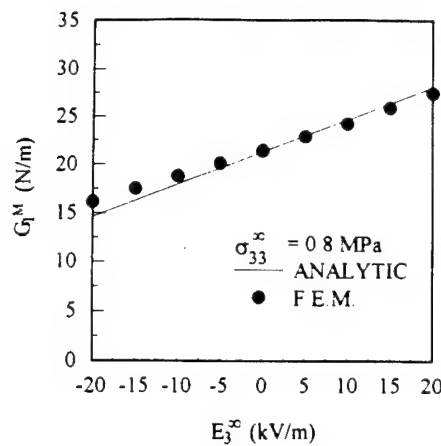


Fig. 10. Comparison of the mechanical strain energy release rate between analytic solution and finite element solution.

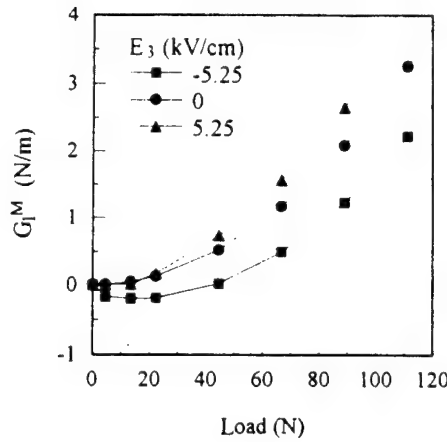


Fig. 11. Mechanical strain energy release rate for different electric fields in the compact tension specimen.

solution should be nearly the same as that for the infinite medium. The mechanical strain energy release rate obtained by finite element analysis was compared with the analytic solution for an infinite piezoelectric medium, Eq. (7). The comparison shown in Fig. 10 indicates that the finite element solution is quite accurate.

V. Data Analysis and Discussion

(1) Mode I Fracture

The compact tension specimen was analyzed first using the finite element method. Figure 11 plots the mechanical strain energy release rate for increasing mechanical loads under different electric fields. For a given load, the mechanical strain energy release rate is higher for positive electric fields and lower for negative electric fields. For the negative electric field case, the mechanical strain energy release rate is negative if the mechanical load is less than 40 N. From the solution for the crack surface displacements, it was noted that in this region of negative strain energy release rate, the crack surfaces penetrate each other. If the mutual penetration of crack surfaces is prevented by requiring surface contact, then the mechanical strain energy release rate should become zero rather than assume negative values.

Using the fracture load for $E_3 = 0$ given by Fig. 4, the critical value of the strain energy release rate, $G_{IC}^M = 2.34$ (N/m), was obtained using the finite element program. Using this critical value, G_{IC}^M , the fracture loads for other applied electric fields were calculated and shown in Fig. 12. For comparison, the fracture loads predicted according to the total energy release

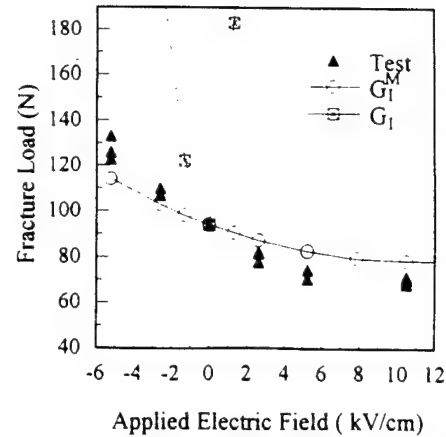


Fig. 12. Comparison of predictions and experimental fracture loads in Mode I fracture tests using compact tension specimens.

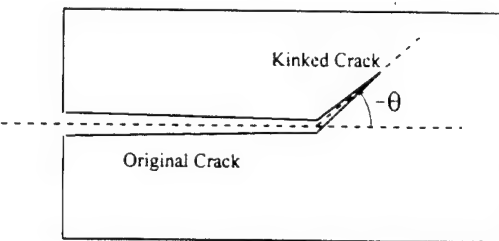


Fig. 13. Kinked crack model for variation of the mechanical strain energy release rate with crack branching direction.

rate are also included in the figure. The superiority of the mechanical strain energy release rate over the total energy release rate criterion is apparent. It is easy to see that the mechanical strain energy release rate criterion predicts the effect of the electric field quite accurately.

(2) Mixed Mode Fracture

With the finite element model, the critical loads were predicted for specimens with cracks at various distances from the midspan. In the prediction of critical loads for mixed mode fracture, it is necessary to investigate directions of crack growth, since the crack would not grow in a self-similar manner. By modeling the kinked crack tip as shown in Fig. 13, the direction of maximum strain energy release rate (G_{max}^M) was obtained. It is noted that G^M is composed of Mode I and Mode II, i.e., $G^M = G_I^M + G_{II}^M$. Models with 2 mm and 4 mm off-center cracks under the electric field of 5 kV/cm were chosen as examples.

Figures 14 and 15 show the variations of mechanical energy release rate versus crack branching angle for 2 mm and 4 mm off-center cracks, respectively. For the 2 mm off-center crack, G_{max}^M occurs at 2.5°, while G_{max}^M occurs at 7.5°. Similarly, G_{max}^M occurs at 5°, while G_{max}^M occurs at 10° for the 4 mm off-center model. Experimental measurements of the directions of initial crack growth were $3^\circ \pm 1^\circ$ and $5^\circ \pm 1^\circ$ for the 2 mm and 4 mm off-center cracks, respectively. Since the mechanical strain energy release rate shown in Figs. 14 and 15 is not sensitive to the crack branching direction, a conclusion cannot be drawn on the crack growth direction.

We assumed that the crack would propagate along the direction of G_{max}^M with $G_{max}^M = G_{IC}^M = 2.34$ (N/m) which was obtained by Mode I compact tension test. Figures 16–18 show comparisons of predicted fracture initiation loads with experimental results for the three unsymmetric three-point bending specimens. They show good agreement. The mechanical strain energy release rate accounts for electric field effects very well.

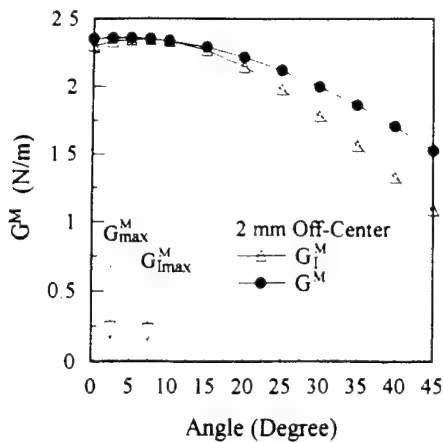


Fig. 14. Variation of the mechanical strain energy release rate with crack branching direction for 2 mm off-center crack.

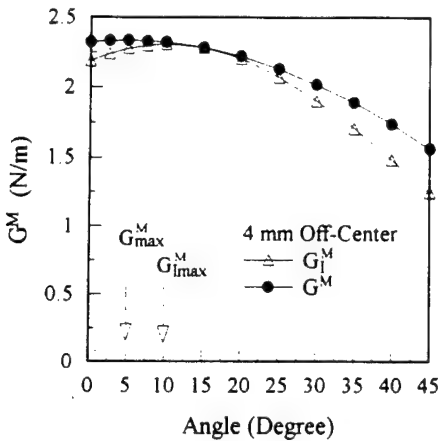


Fig. 15. Variation of the mechanical strain energy release rate with crack branching direction for 4 mm off-center crack.

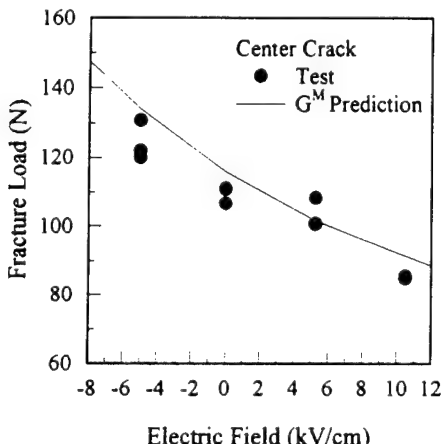


Fig. 16. Comparison of fracture loads for center crack.

VI. Conclusion

From the results of the present study, the following conclusions have been obtained.

- The mechanical strain energy release rate is a good fracture criterion for piezoelectric ceramics.
- Stress intensity factors and the total energy release rate are not suitable for describing the fracture behavior of piezoelectric ceramics.

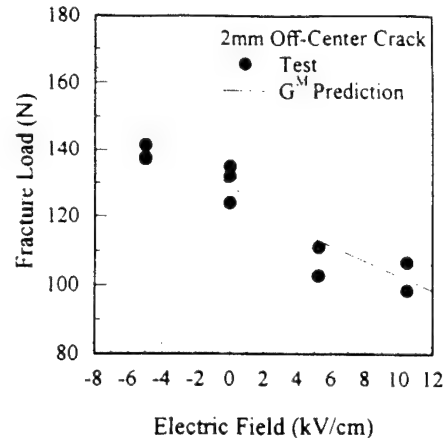


Fig. 17. Comparison of fracture loads for 2 mm off-center crack.

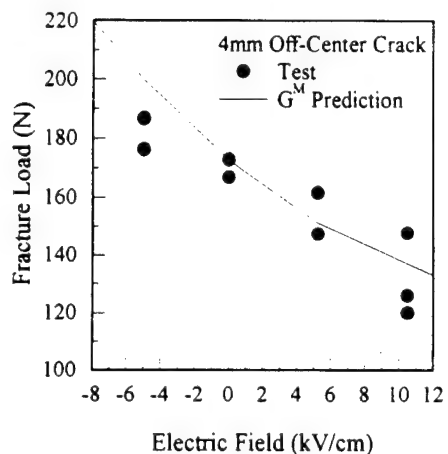


Fig. 18. Comparison of fracture loads for 4 mm off-center crack.

• Positive electrical fields aid crack propagation, while negative electric fields impede crack propagation. In other words, positive electric fields decrease the apparent fracture toughness of piezoelectric ceramics, while negative electric fields increase it.

References

- V. Z. Parton and B. A. Kudryavtsev, *Electromagnetoelasticity*, Gordon and Breach, New York, 1988.
- W. F. J. Deeg, "The Analysis of Dislocation, Crack and Inclusion Problem in Piezoelectric Solids," Ph.D. Thesis, Stanford University, Stanford, CA, 1980.
- Y. E. Pak, "Crack Extension Force in a Piezoelectric Material," *J. Appl. Mech.*, **57**, 647-53 (1990).
- H. A. Sosa and Y. E. Pak, "Three Dimensional Eigenfunction Analysis of a Crack in a Piezoelectric Material," *Int. J. Solids Struct.*, **26** [1] 1-15 (1990).
- Z. Suo, C.-M. Kuo, D. M. Barnett, and J. R. Willis, "Fracture Mechanics for Piezoelectric Ceramics," *J. Mech. Phys. Solids*, **40** [4] 739-65 (1992).
- S. B. Park and C. T. Sun, "Effect of Electric Field on Fracture of Piezoelectric Ceramics," *Int. J. Fract.*, in press.
- K. D. McHenry and B. G. Koepke, "Electric Field Effects on Subcritical Crack Growth in PZT," *Fract. Mech. Ceram.*, **5**, 337-52 (1983).
- A. G. Tobin and Y. E. Pak, "Effect of Electric Fields on Fracture Behavior of PZT Ceramics," *Proc. SPIE, Smart Struct. Mater.*, **1916**, 78-86 (1993).
- A. N. Stroh, "Dislocation and Cracks in Anisotropic Elasticity," *Philos. Mag.*, **3**, 625-46 (1958).
- A. N. Stroh, "Steady State Problems in Anisotropic Elasticity," *J. Math. Phys.*, **41**, 77-103 (1962).
- ANSYS, Revision 5.0, Swanson Analysis Systems, Houston, PA, 1992.
- G. R. Irwin, "Analysis of Stresses and Strains near the End of a Crack Traversing a Plate," *J. Appl. Mech.*, **24**, 557-91 (1957).
- E. F. Rybicki and M. F. Kanninen, "A Finite Element Calculation of Stress Intensity Factors by a Modified Crack Closure Integral," *Eng. Fract. Mech.*, **9**, 931-38 (1977).
- C. J. Jih and C. T. Sun, "Evaluation of a Finite Element Based Crack-Closure Method for Calculating Static and Dynamic Strain Energy Release Rate," *Eng. Fract. Mech.*, **37** [2] 313-22 (1990).
- H. Allix and T. J. R. Hughes, "Finite Element Method for Piezoelectric Vibration," *Int. J. Num. Meth. Eng.*, **2**, 151-57 (1970). □

**Determination of Fracture Toughness of Piezoceramics
Under the Influence of Electric Field Using Vickers Indentation**

C. T. Sun and S. B. Park

School of Aeronautics and Astronautics
Purdue University
West Lafayette, Indiana 47907-1282

ABSTRACT

Vickers indentation is a popular method for determining fracture toughness of brittle materials. Although this method depends on an empirical formula relating the stress intensity factor (or toughness) to the indentation parameters, it is simple and economical. In this study, the Vickers indentation method was used to determine the apparent fracture toughness of PZT-4 piezoceramic under the influence of electric fields. The mechanical strain energy release rate associated with the crack produced by the Vickers indenter was derived. Using the analytical mechanical strain energy release rate for an infinite piezoelectric medium with a center crack and far field in-plane mechanical and electrical loadings, the mechanical strain energy release rate was obtained for Vickers indentation, which involves the out-of-plane indentation load. The effect of the electric field is properly included. The accuracy of the proposed formula was verified by experimental results.

Keywords : Piezoelectric ceramic, Crack, Fracture, Strain energy release rate, Vickers indentation

1. INTRODUCTION

Due to the characteristics of strong coupling between mechanical and electric fields, man made piezoelectric ceramics are used as actuation devices in adaptive structural applications. However, piezoelectric ceramics are very brittle and susceptible to fracture during service. Moreover, once a crack exists in a piezoelectric medium, actuation forces may act as crack driving forces and the presence of cracks would degenerate mechanical as well as electrical performance of the material and finally cause the failure in structural integrity. Accordingly, the fracture behavior of these materials must be understood to assure safe usage of these materials.

Several researchers¹⁻⁸ have performed analyses of piezoelectric materials containing a crack. Unlike non-piezoelectric materials, there are electric field effects on fracture of piezoelectric materials. Due to this phenomenon, fracture criteria for non-piezoelectric materials such as stress intensity factors, etc., are not directly applicable. Some effort has been made to establish the fracture criterion for piezoelectric materials. Similar to the path independent integral of Cherepanov⁹, the total potential energy release rate was derived and used to account for the electric field effect on fracture.^{1,4,8,10} However, fracture behavior according to the total potential energy release rate does not agree with experimental observations.¹¹⁻¹³ Recently Park and Sun¹⁴⁻¹⁶ proposed the mechanical strain energy release rate as a fracture criterion for piezoelectric materials. The validity of this criterion was verified by fracture experiment using compact tension and three point bending PZT-4 piezoceramic specimens.

Compared with conventional fracture toughness testing methods, Vickers indentation technique¹⁷⁻²¹ offers a simple and economic alternative. Extensive work was performed to use the crack length which is measured directly in determining the critical stress intensity factor, K_C . Tobin and Pak¹³ applied the indentation test to piezoelectric ceramics to observe the effect of electric field on fracture. They measured indentation-induced cracks under an electric field and calculated stress intensity factors. With that they could show only qualitative fracture behavior under electric fields.

In this study, quantitative fracture was predicted using Vickers indentation technique. Since an indentation induced crack is relatively small compared to the specimen size, it can be considered as a crack in an infinite plate. Accordingly, for the prediction of indentation induced crack, the expression of the mechanical strain energy release rate for a center cracked infinite plate obtained analytically was tried. The differences of loading conditions, i.e., in-plane stress applied at far field for analytical solution and out-of-plane indentation load for indentation tests, was overcome through the stress intensity factor.

2. ANALYSIS

2.1. Fracture Criteria for Piezoelectric Materials

Park and Sun¹⁵ obtained closed form solutions explicitly for all three modes of fracture for an infinite piezoelectric medium containing a center crack with electrically insulated surfaces. From the solution obtained, the near tip stresses and electric displacement for Mode I and Mode II are expressed at the crack tip in the crack plane, $\theta = 0$, as

$$\sigma_{23} = \frac{K_{II}}{\sqrt{2\pi r}}, \quad \sigma_{33} = \frac{K_I}{\sqrt{2\pi r}}, \quad D_3 = \frac{K_{IV}}{\sqrt{2\pi r}} \quad (1)$$

$$\text{where } K_I = \sqrt{\pi a} \sigma_{33}^\infty, \quad K_{II} = \sqrt{\pi a} \sigma_{23}^\infty, \quad K_{IV} = \sqrt{\pi a} D_3^\infty$$

Both mechanical and electrical loading were imposed parallel to the x_3 -axis which was the poling direction, and a center crack was imbedded perpendicular to the poling direction. It is noted that stresses and electric displacement are uncoupled in this plane. This indicates that the electric loading alone cannot produce mechanical stress in the crack plane ahead of the crack tip and vice versa. If the stress intensity factor is used as a fracture criterion, the effect of the electric field cannot be accounted for. On the other hand, experimental results indicate that the apparent fracture toughness of piezoelectric materials is affected by electric fields. This leads us to conclude that the stress intensity factor is not suitable as a fracture criterion for piezoelectric materials.

For some time, researchers have attempted to use the total potential energy release rate to account for the effect of an electric field on toughness without success. In terms of the total potential energy release rate, the electric field (either positive or negative) always enhances toughness. This contradicts the experimental observation. Recently, the present authors^{15,16} have proposed the use of the mechanical strain energy release rate to measure the fracture toughness of piezoelectric ceramics in the presence of electric fields. This concept was proven by fracture experiments using compact tension specimens and three point bending specimens.

For an infinite PZT-4 piezoelectric ceramic containing a center crack and subjected to Mode I remote loadings, the mechanical strain energy release rate (G_I^M) was obtained as¹⁶

$$G_I^M = \frac{\pi a}{2} (148 \times 10^{-11} \sigma_{33}^\infty)^2 + 2.67 \times 10^{-2} \sigma_{33}^\infty D_3^\infty \quad (N/m) \quad (2)$$

$$\text{or} \quad G_I^M = \frac{\pi a}{2} (2.12 \times 10^{-11} \sigma_{33}^\infty)^2 + 2.67 \times 10^{-10} \sigma_{33}^\infty E_3^\infty \quad (N/m) \quad (3)$$

It is noted that the problem is a plane strain and the poling direction is assumed to be parallel to the x_3 -axis. The result indicates that the mechanical strain energy release rate is increased or decreased depending on the direction of electric loading, implying that crack propagation may be enhanced or retarded.

2.2. Vickers Indentation

For the Vickers indentation test, since the indentation induced crack is small compared to the dimension of specimen, an attempt was made to relate Vickers indentation with analytic solutions for center cracked infinite plate with far field loadings.

For isotropic, homogeneous materials, explicit equations for the radial crack evolution by a sharp indenter have been empirically formulated by many researchers^{17,18}. For a sufficiently well defined crack, i.e., $a \gg D$, where a and D are, respectively, measured crack length and one half diagonal length of the indentation pyramid, the stress intensity factor (K) can be expressed in terms of material constants, indentation load and indentation induced crack length such as¹⁷

$$K = 0.016 \left(\frac{E}{H} \right)^{\frac{1}{2}} P a^{-\frac{3}{2}} , \quad H = \frac{P \sin(\alpha/2)}{2D^2} \quad (4)$$

where P is the applied indentation load in Newton and E and H are expressed in N/m^2 and represent Young's modulus and Vickers hardness, respectively; α is the apex angle of the Vickers diamond indenter and is normally 136° .

From the stress intensity factor obtained using Eq. (4), the mechanical strain energy release rate for piezoelectric materials without electric field can be obtained via the relationship of the stress intensity factor and the strain energy release rate for homogeneous, non-piezoelectric materials. However, to account for the electric field effects on fracture of piezoelectric materials, it is needed to use the mechanical strain energy release rate criterion as a fracture criterion instead of using the stress intensity factor alone.

It is attempted to relate the stress intensity factor, which is composed of the indentation load and the measured indentation produced crack length on the indentation surface, to the mechanical strain energy release rate for piezoelectric materials, Eq. (3). The expression of mechanical strain energy release rate for center cracked infinite plate with far field loadings, Eq. (3), cannot be directly related to the case of Vickers indentation test since the former deals with in-plane far field mechanical loading, σ_{33}^∞ , whereas the latter deals with out-of-plane indentation load, P . Hence, it is necessary to relate the indentation load indirectly with the mechanical strain energy release rate.

Following the conventional definition, define stress intensity factor, K_I , as

$$K_I = \sqrt{\pi a} \sigma_{33}^\infty \quad (5)$$

Equation (3) can be written in terms of the stress intensity factor as

$$G_I^M = \frac{1}{2} (2.12 \times 10^{-11} K_I^2 + 2.67 \times 10^{-10} \sqrt{\pi a} E_3^\infty K_I) \quad (6)$$

Substituting Eq. (4) into Eq. (6), the mechanical strain energy release rate in terms of the indentation load and electric field applied can be obtained as

$$G_I^M = 2.71 \times 10^{-15} \left(\frac{E}{H} \right) P^2 a^{-3} + 3.78 \times 10^{-12} \left(\frac{E}{H} \right)^{\frac{1}{2}} P E_3^\infty a^{-1} \quad (7)$$

Using this equation, the mechanical strain energy release rate can easily be obtained by measuring crack (a) and a half diagonal (D) after indentation.

3. EXPERIMENTAL PROCEDURE

PZT-4 piezoelectric ceramics were used for test materials. Material properties are listed in Table 1. As received materials were $50.8 \times 19.1 \times 5.1$ (mm) plate and the poling was done along the axis of 19.1 (mm) dimension. They were cut in $20 \times 5 \times 5.1$ (mm) dimension holding 5 mm in poling direction. Since the crack size of indentation is small, it is particularly important to polish the indenting surface. Specimens were polished in several steps. Starting from the 600 grit silicon carbide polishing wheel, specimens went through finer grit sized wheels and finished with a $0.5 \mu m$ grain sized Alumina polishing pad. It is noted that all the cutting and polishing processes were done in water.

Silver paint was used as electrodes which were applied on the surfaces perpendicular to the poling axis. Electric wires were soldered to the electrodes. Soldering was done for 5 seconds with $150^\circ C$ solder to avoid local depolarization by exceeding the Curie temperature.

<u>Elastic Constants</u> (N / m^2)	$c_{11} = 13.9 \times 10^{10}$, $c_{12} = 7.78 \times 10^{10}$, $c_{13} = 7.43 \times 10^{10}$, $c_{33} = 11.3 \times 10^{10}$, $c_{44} = 2.56 \times 10^{10}$
<u>Piezoelectric Constants</u> (C / m^2)	<u>Dielectric Permittivities</u> (C / Vm)
$e_{31} = -6.98$, $e_{33} = 13.84$, $e_{15} = 13.44$	$\epsilon_{11} = 6.00 \times 10^{-9}$, $\epsilon_{33} = 5.47 \times 10^{-9}$
<u>Density</u> (kg / m^3) : 7.55×10^3	<u>Curie Temperature</u> : $300^\circ C$
<u>Static Tensile Strength</u> (MPa) : 75.8	

Table 1. Material properties of PZT-4 piezoelectric ceramics

A silicon oil tub was mounted on a typical Vickers indentation facility and tests were performed in the silicon oil tub to prevent electric discharging through the air. Figure 1 shows the experimental setup. To generate electric fields, a power supplier which can produce up to 50kV in D.C. was used. The peak indentation load was applied via a dashpot mounted for 10 seconds, then, unloaded rapidly in 1 second under a certain electric field. Due to the limitation of facility, the minimum indentation load used was 4.45N.

Tests were conducted in various electric fields both positive and negative to investigate electric field effect on crack growth. For each level of electric field and indentation load, 25 to 30 indentations were performed, and crack lengths parallel and perpendicular to the poling were measured. Crack lengths were measured with the calibrated eyepiece mounted on the indenter. Figure 2 shows dimensions of indentation-induced cracks.

There are several factors to consider in obtaining reliable data from the indentation test. The ambient condition of the indentation test is one of the significant factors¹⁷. Specifically, the indentation performed in silicon oil produced shorter cracks than the one performed in the air. It is thought that moisture in the air and friction between the contact surfaces may affect crack growth. Another factor is the delayed time for crack length measurement after completion of indentation. It has been reported that post-indentation slow crack growth could occur¹⁷. In this study, the crack length was measured immediately after indentation.

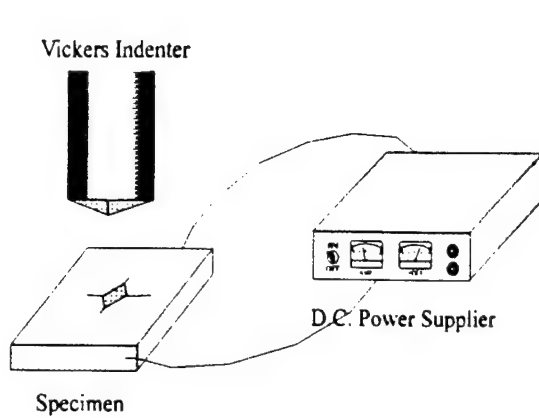


Fig. 1. Experimental setup for indentation tests.

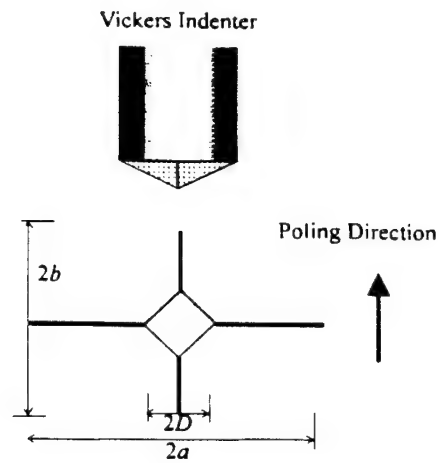


Fig. 2. Dimensions of crack formed by Vickers indenter.

4. RESULTS AND DISCUSSION

Figure 3 shows a typical indentation shape for PZT-4 piezoelectric ceramic. It is noted that there is significant anisotropy in the crack pattern; i.e., crack growth perpendicular to the poling direction is significantly greater than the one parallel to the poling direction. This anisotropic material property was induced during the poling process. As shown in the figure, a well developed half penny-shaped crack was formed beneath the indentation surface.

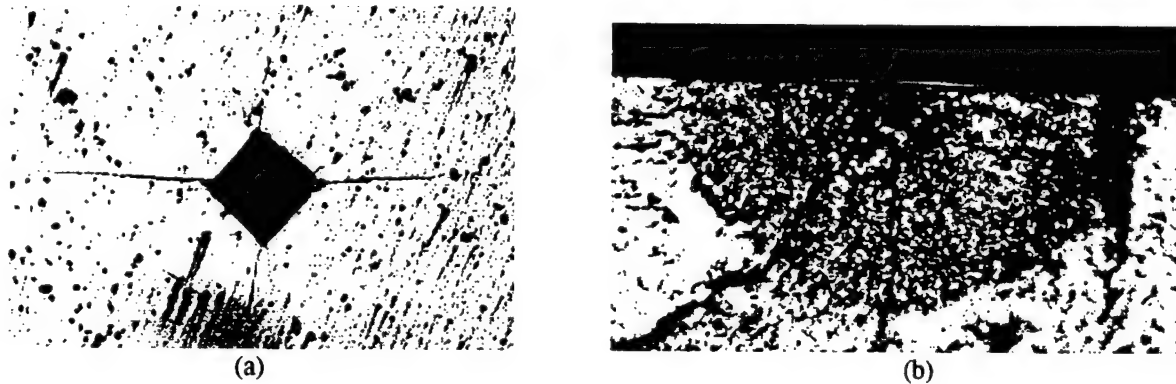
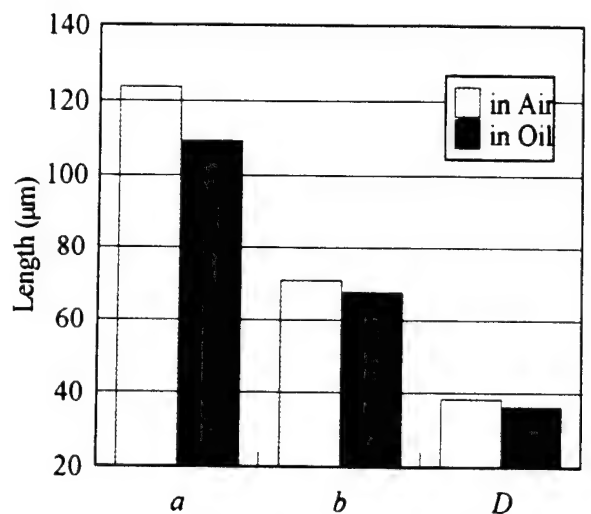


Fig. 3. Typical indentation induced crack (a) indentation surface, (b) beneath the surface.

Indentation tests without electric field were performed both in air and in silicon oil. Figure 4 shows the resulted half diagonal length of indentation (D), and crack lengths transverse to the poling (a) and parallel to the poling (b). The results indicate that cracks produced in the air are longer than cracks produced in oil. To assess the effect of the electric field, data obtained from tests performed in oil were used. The relation between indentation load(P) and a half diagonal length(D) was plotted in Fig. 5. Recalling Eq. (4), the linear relation of these parameters in logarithm scale with a slope of 1/2 means it has a constant Vickers hardness (H) regardless of indentation load, i.e., $H=1.57(GPa)$.

Tables 2 and 3 list variations of the crack length along with different electric fields for 4.45N and 22.24N indentation loads, respectively. Evidently, crack growth perpendicular to the poling direction is affected by the electric field whereas the crack growth parallel to the poling direction is not since the electric field near the crack tip is not disturbed by the crack parallel to the poling. Due to the anisotropy induced by the poling process, the electric effect is maximized in the plane perpendicular to the poling direction²¹. This study focuses on the crack perpendicular to the poling direction.



a : perpendicular to poling ; b : parallel to poling

D : a half diagonal of indentation.

Fig. 4. Indentation crack length in air and oil at 4.45 N load.

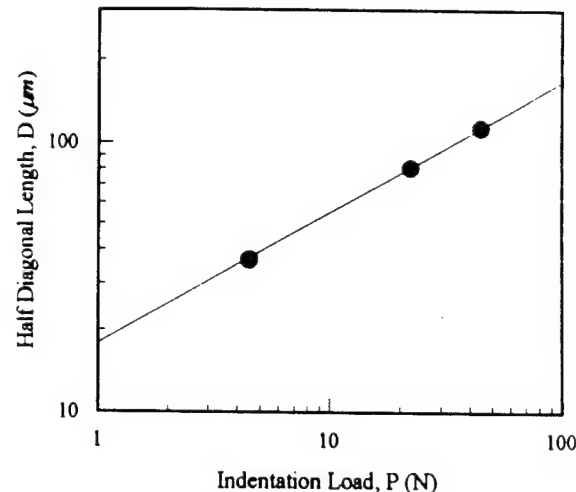


Fig. 5. A half diagonal length(D) under various indentation load in log-log scale.

P=4.45N			
E_3° (kV/cm)	a (μm)	b (μm)	D (μm)
-7.5	103.09 ± 1.77	68.23 ± 2.19	35.68 ± 0.83
-5.0	107.08 ± 3.78	69.37 ± 3.01	36.03 ± 0.74
0.0	109.08 ± 1.97	69.96 ± 2.83	36.46 ± 0.75
5.0	116.59 ± 2.69	68.12 ± 3.33	35.85 ± 0.69
7.5	125.03 ± 2.98	69.53 ± 2.22	35.50 ± 0.80

Table 2. Indentation crack length under various electric fields with 4.45N indentation load.

P=22.24N			
E_3° (kV/cm)	a (μm)	b (μm)	D (μm)
-5.0	315.94 ± 8.97	175.79 ± 8.24	82.13 ± 2.25
-2.5	314.65 ± 9.04	172.40 ± 7.75	83.17 ± 1.44
0.0	301.71 ± 4.39	168.03 ± 5.65	80.79 ± 1.41
2.5	320.34 ± 9.55	167.49 ± 7.65	78.13 ± 1.46
5.0	349.12 ± 9.29	182.21 ± 7.48	82.58 ± 2.64

Table 3. Indentation crack length under various electric fields with 22.24N indentation load.

$P=44.48N$			
$E_3^o (kV/cm)$	$a (\mu m)$	$b (\mu m)$	$D (\mu m)$
0.0	466.14 ± 6.98	263.79 ± 9.80	113.57 ± 1.59

Table 4. Indentation crack length with 44.48N indentation load.

For the 4.45N indentation load, see Table 2, a positive electric field increased crack growth, implying reduced apparent fracture toughness, and a negative electric field decreased crack growth. These phenomena agree qualitatively with the observations of fracture in the compact tension test. Using PZT-8 piezoelectric ceramic specimens, Tobin and Pak¹³ performed Vickers indentation tests and observed a behavior similar to the present results. For the 22.24N load case, see Table 3, the trend was similar to the 4.45N load case for positive electric fields. However, the inverting crack growth under negative electric fields is inconsistent with the 4.45N load case.

From Eq. (4) and the results of the indentation test given by Tables 2 and 3, it is concluded that the hardness, H , is not affected by the electric field and the indentation load since the diagonal length, $2D$, of the indentation pyramid remains constant for electric fields. Using Eq. (7) and the measured crack lengths, $a = 109.08(\mu m)$, $a = 301.71(\mu m)$, and $a = 466.14(\mu m)$ in the absence of electric field for $P=4.45N$, 22.24N and 44.48N, respectively, the critical strain energy release rates are obtained as

$$\begin{aligned} G_{Kc}^M &= 2.18(N/m) \quad \text{for } P=4.45N \\ G_{Kc}^M &= 2.53(N/m) \quad \text{for } P=22.24N \\ G_{Kc}^M &= 2.71(N/m) \quad \text{for } P=44.48N \end{aligned} \quad (8)$$

These results exhibit about -7, 7, 16% difference compared to the value $G_{Kc}^M = 2.34(N/m)$ obtained from the compact tension tests by Park and Sun¹⁶. It is thought that internal stresses induced by the poling and polishing process might have caused the measured fracture toughness to be dependent on the indentation load. Using the equilibrium equations, a formula was proposed¹⁹ to account for the effect of internal stresses as

$$K_{Kc} = K_{Kc}^0 + 2\sqrt{a/\pi}\sigma_i \quad (9)$$

where σ_i is the normal internal stress parallel to the poling direction, and K_{Kc}^0 is the intrinsic fracture toughness. Using this relation, the internal stress can be obtained from the slope of K_{Kc} versus \sqrt{a} . Figure 6 shows the linear relation between stress intensity factor, K_{Kc} , and a square root of crack length, \sqrt{a} . As a result, we obtain $\sigma_i = 4.15(MPa)$. It is worth noting that σ_i includes residual stresses from the machining or manufacturing and intrinsic internal stresses from the poling procedure. Only the portion of machining and manufacturing induced residual stresses can be removed by a proper annealing process.

Taking the critical strain energy release rates from the indentation test given by Eq. (8), the crack lengths under electric fields were predicted for each indentation loading using Eq. (7) and measured crack lengths. Figures 7 and 8 show the predicted crack length versus the electric field for 4.45N and 22.24N indentation loads, respectively. It is seen that the predictions agree with the experimental results very well for positive electric fields. However, the predictions deviate from the experimental data significantly for negative electric fields, especially for the case of the larger indentation load.

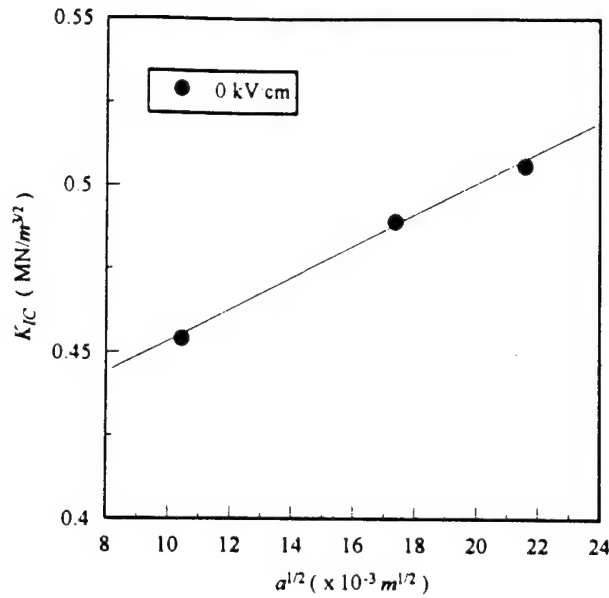


Fig. 6. Stress intensity factor under different indentation loads or crack lengths without electric field.

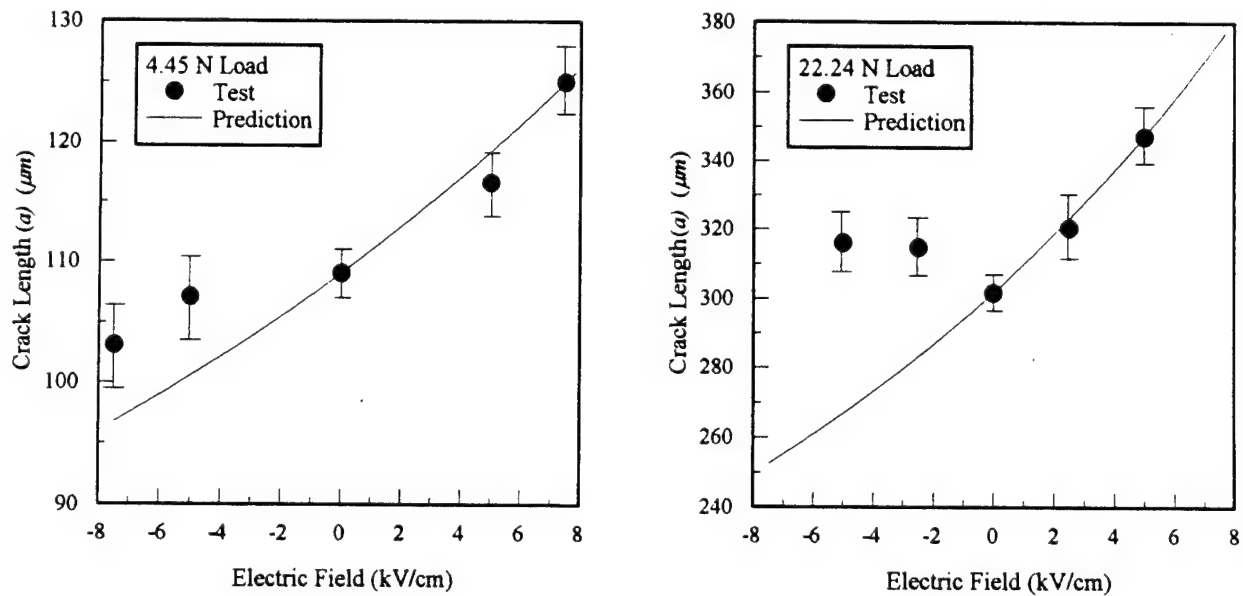


Fig. 7. Prediction of crack length under electric field using the mechanical strain energy release criterion for $P=4.45\text{N}$.

Fig. 8. Prediction of crack length under electric field using the mechanical strain energy release criterion for $P=22.24\text{N}$.

A possible explanation for this deviation is as follows. In calculating the mechanical strain energy release rate, crack surfaces were modeled as insulated boundary conditions. Considering the low electric permittivity of air or silicon oil, this assumption can be justified for the compact tension test performed by present authors¹⁶ since

the width of the machine notched initial crack was large enough and crack surfaces were always opened both under positive and negative electric fields. For the Vickers indentation test under positive electric fields, both the indentation load and electric field tend to open the crack. However, the specimen is in contraction under a negative electric field and the indentation-produced crack surfaces might be in contact. Cao and Evans²² suggested a wedging mechanism for the contact in the indentation-induced crack that may produce additional crack growth.

ACKNOWLEDGMENT

This work was supported by AFOSR through grant F 49620-92-J-0457 to Purdue University.

REFERENCES

1. V. Z. Parton, B.A. Kudryavtsev, *Electromagnetoelasticity*, Gordon and Breach Science Publishers, New York, 1988.
2. R.M. McMeeking, "A J-Integral for the Analysis of Electrically Induced Mechanical Stress at Cracks in Elastic Dielectrics", *Int. J. Engng Sci.*, **28**, No. 7, 605-613, 1990.
3. W. F. J. Deeg, "The analysis of Dislocation, Crack, and Inclusion Problems in Piezoelectric Solids", Ph.D. Thesis, Stanford Univ., 1980.
4. Y. E. Pak, "Crack Extension Force in a Piezoelectric Material", *J. Appl. Mech.*, **57**, 647-653, 1990.
5. H. A. Sosa, Y. E. Pak, "Three Dimensional Eigenfunction Analysis of a Crack in a Piezoelectric Material", *Int. J. Solids Structures.*, **26** [1], 1-15, 1990.
6. H.A. Sosa, "Plane Problems in Piezoelectric Media with Defects", *Int. J. Solids Structures.*, **28**, 491-505, 1991.
7. H.A. Sosa, "On the Fracture Mechanics of Piezoelectric Solids", *Int. J. Solids Structures.*, **29**, 2613-2622, 1992.
8. Z. Suo, C.-M. Kuo, D. M. Barnett, J. R. Willis, "Fracture Mechanics for Piezoelectric Ceramics", *J. Mech. Phys. Solids*, **40**, [4], 739-765, 1992.
9. G.P. Cherepanov, *Mechanics of Brittle Fracture*, McGraw-Hill., New York, 1979.
10. Y.E. Pak and G. Herrmann, , "Conservation Laws and the Material Momentum Tensor for the Elastic Dielectric", *Int. J. Engng. Sci.*, **24**, No. 8, 1365-1374, 1986.
11. K.D. McHenry and B.G. Koepke, "Electric Field Effects on Subcritical Growth in PZT", *Fracture Mech. of Ceramics*, **5**, 337-352, 1983.
12. R.C. Pohanka and P.L. Smith, "Recent Advances in Piezoelectric Ceramics" in *Electronic Ceramics*, 45-146, Marcel Dekker, New York, 1988.
13. A.G. Tobin and Y.E. Pak, "Effect of Electric Fields on Fracture Behavior of PZT Ceramics", *Proc. of SPIE, Smart Structures and Materials*, **1916**, 78-86, 1993.

14. S. B. Park, C. T. Sun, "Crack Extension in Piezoelectric Materials", *Proc. of SPIE, Smart Structures and Materials*, **2189**, 357-368, Orlando, Florida, 1994.
15. S. B. Park, C. T. Sun, "Effect of Electric Field on Fracture of Piezoelectric Ceramics", accepted for publication in *Int. J. Fracture*.
16. S. B. Park, C. T. Sun, "Fracture Criteria for Piezoelectric Ceramics", accepted for publication in *J. Am. Cer. Soc.*
17. G.R. Anstis, P. Chantikul, B.R. Lawn and D.B. Marshall, "A Critical Evaluation of Indentation Techniques for Measuring Fracture Toughness: I, Direct Measurements", *J. Am. Cer. Soc.*, **64**, 533-538, 1981.
18. G.R. Anstis, P. Chantikul, B.R. Lawn and D.B. Marshall, "A Critical Evaluation of Indentation Techniques for Measuring Fracture Toughness: II, Strength Method", *J. Am. Cer. Soc.*, **64**, 539-543, 1981.
19. D.B. Marshall and B.R. Lawn, "An Indentation Technique for Measuring Stress in Tempered Glass Surfaces", *J. Am. Cer. Soc.*, **60**, 86-87, 1977.
20. K. Okazaki, "Mechanical Behavior of Ferroelectric Ceramics", *J. Am. Cer. Soc. Bulletin*, **63**, No. 9, 1150-1157, 1984.
21. G.G. Pisarenko, V.M. Chushko, and S.P. Kovalev, "Anisotropy of Fracture Toughness of Piezoelectric Ceramics", *J. Am. Cer. Soc.*, **68**, 259-265, 1985.
22. H. Cao and A.G. Evans, "Electric-Field-Induced Fatigue Crack Growth in Piezoelectrics", *J. Am. Cer. Soc.*, **77**, 1783-1786, 1994.

Use of thickness-shear mode in adaptive sandwich structures

C T Sun and X D Zhang

School of Aeronautics and Astronautics, Purdue University, West Lafayette, IN 47907-1282, USA

Received 15 March 1995, accepted for publication 1 June 1995

Abstract. A new adaptive sandwich structure is constructed using the shear mode of piezoelectric materials. A comparative study of the sandwich structure and the corresponding surface-mounted actuation structure is performed using finite-element analysis. The effects of actuator length and location on actuation performance of the structures are studied. The stress distributions under mechanical and electrical loads are investigated for both the sandwich beam and the surface-mounted actuation beam. It is shown that the stress level within the actuators is more severe for the surface-mounted actuation beam than for the sandwich. Also, the interface-stress distribution between actuator and host structure is analysed. It is shown that sandwich construction offers many advantages over conventional surface-mounted actuation constructions.

1. Introduction

An increasing number of practical applications for piezoelectric actuators have been proposed and demonstrated in recent years [1, 2]. They are finding application in ultrasonics, shape control, active vibration control and other areas. To meet the demands of engineering practice, many analytical models [3, 4] have been proposed to describe and predict the interaction between piezoelectric actuators and host structures.

Piezoelectric actuators in an adaptive structure are either surface-mounted or embedded in the host structure. Surface-mounted actuators are susceptible to damage inflicted by contact with foreign objects. Furthermore, placed at the extreme thickness positions of the structure, the actuator would be subjected to high bending stresses which may prove detrimental to the brittle piezoceramic material. Embedding actuators in composite structures is possible. However, to accommodate the actuator, the composite material must be cut or removed, causing possible reduction in stiffness, strength and durability of the host structure. Moreover, to produce deflection in beams, plates or shells using surface-mounted actuators, the actuator must induce bending strains in the structure. Since these structures are intended for taking bending loads, they are usually made of high-modulus materials. It is obvious that to produce bending strains, and thus deflections, large actuation forces are required. In view of the foregoing, efficient actuation must be realized in a deformation mode that does not require significant bending strains in the host structure.

Sandwich structures consisting of stiff facing sheets and a relatively soft lightweight core such as honeycomb or rigid foam are highly efficient in bending. Deflection

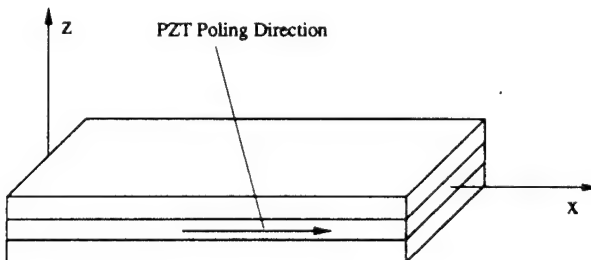


Figure 1. Schematic diagram of the adaptive sandwich beam.

of a sandwich structure is contributed by bending and transverse shear deformations. Due to the lower stiffness of the core, it would be easier to actuate the transverse shear deformation mode to produce the deflection of the sandwich structure. This characteristic leads us to the idea of a new adaptive structure. The proposed adaptive sandwich structure consists of stiff facing sheets with a piezoelectric core as shown in figure 1. The piezoelectric core is positioned in such a way that an electric field in the thickness direction would generate the thickness (or transverse) shear deformation of the core. The transverse shear deformation in the core would give rise to the desired transverse deflection of the sandwich. This new sandwich construction offers many advantages over conventional surface-mounted constructions. For example, stresses in the piezoelectric core are much lower for achieving the same deflection of the structure. Moreover, the sandwich offers much better structural bending stiffness than the conventional designs.

In order to demonstrate the effectiveness of the new adaptive sandwich structure, the corresponding surface-

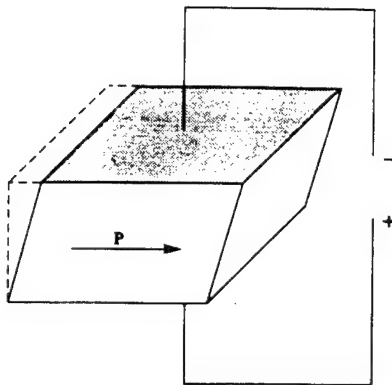


Figure 2. Shear mode of the piezoelectric core.

mounted actuation structure is used as a reference throughout the study. Unlike the sandwich, the poling direction of the surface-mounted actuator is in the z direction. The applied electric field is also parallel to the z direction. A sandwich structure with a small piezoelectric patch and its surface-mounted counterpart are studied using finite-element analysis. Specifically, the effects of piezoelectric actuator location, actuator length, and stress distribution within the actuator under mechanical and electrical loads are investigated.

2. Adaptive sandwich structure

The underlying principle of sandwich construction can be illustrated as follows. In a sandwich construction (see figure 1), the top and bottom layers are stiff facing sheets, and the central layer is a piezoelectric core in which the poling direction of the piezoelectric material is arranged along the x direction. When an electric field is applied along the z direction, the piezoelectric core will produce a pure shear deformation which is the driving force for the transverse deflection of the sandwich construction. The shear deformation of the core is depicted in figure 2.

Due to the high density and the brittleness of piezoceramics, it is impractical to cover the entire structure with piezoelectric layers. In practice, small patches are used. In this study, the core of the sandwich structure is assumed to consist of a small amount of piezoceramic, and the rest of rigid foam or honeycomb.

The schematic diagram of the sandwich is shown in figure 3(a). Most of the core is rigid foam material, and only a small portion of the core is occupied by the piezoelectric material. In order to verify the effectiveness of the sandwich structure, its actuation behavior is compared with the corresponding surface-mounted actuation beam, as shown in figure 3(b). The total thickness of the two piezoelectric patches in the surface-mounted beam is equal to the thickness of the piezoelectric core in the sandwich beam, and the beam thickness of the surface-mounted case is equal to the sum of thicknesses of the top and bottom sheets of the sandwich beam.

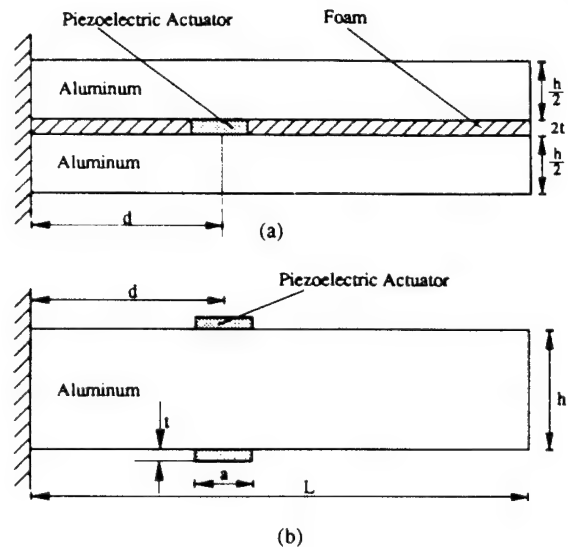


Figure 3. Adaptive sandwich beam and surface-mounted actuation beam.

3. Electric-field-induced deflection

The geometries of the sandwich beam and the surface-mounted actuation beam are shown in figure 3. Both structures are fixed at the end $x = 0$, and free at $x = L$. Static voltages are applied at the top and bottom surfaces of the piezoelectric actuators to produce actuation forces. The geometrical parameters of both structures are assumed to be $L = 10$ cm, $h = 1.6$ cm and $t = 0.1$ cm. The voltage applied on the piezoelectric core in the sandwich beam is $V_1 = 20$ V, and the voltage applied on the surface-mounted actuators is $V_2 = 10$ V. Thus, the electric field intensities in the actuators for both structures are identical.

The non-piezoelectric layers of both structures are assumed to be aluminium, and the actuators are PZT5H piezoceramics. The mechanical properties of the two materials are listed in table 1. The rigid foam has a density of 32 kg m^{-3} , a Young's modulus of 35.3 MPa, and a shear modulus of 12.76 MPa.

The finite-element analysis is performed using the ANSYS code. Four-node linear plane-strain coupled elements are used for the piezoelectric actuator; and four-node linear plane-strain structural elements are used for the remaining part of the structure. To begin with, the length of the piezoelectric actuators is chosen to be a fixed length $a = 1$ cm. The effect of actuator location (d) on the transverse displacement at the right tip is studied first. For the sandwich beam, the model consists of 16×100 elements for the two covering sheets, 4×90 for the foam material, and 4×10 for the actuator. For the surface-mounted beam, the model consists of 16×100 elements for the beam and 2×10 for each actuator. The transverse displacements at the right tip corresponding to different actuator locations are shown in figure 4. It is clear from figure 4 that the optimum location of the actuator for the sandwich beam is at 15% of the beam length from the fixed end, and is at the fixed end for the surface-mounted actuation beam. It is also shown that for actuator length $a = 1$ cm, the maximum tip

Table 1. Mechanical properties for computer simulation.

PZT5H					A1				
GPa					C m ⁻²		GPa		
C_{11}^E	C_{12}^E	C_{13}^E	C_{33}^E	C_{44}^E	θ_{31}	θ_{33}	θ_{15}	E	ν
126	79.5	84.1	117	23	-6.5	23.3	17.0	70.3	0.34

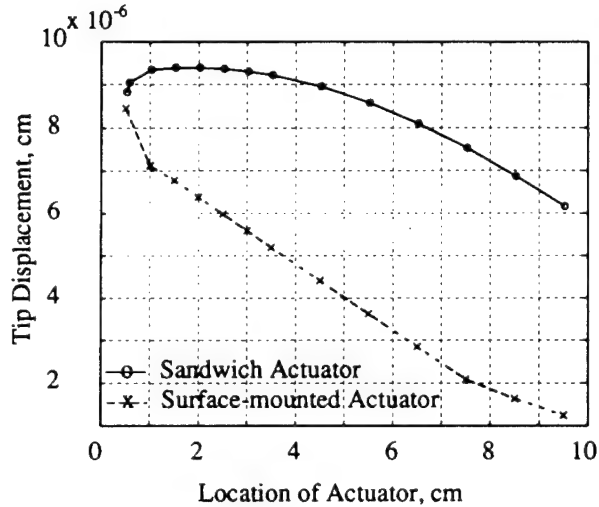


Figure 4. Effect of actuator location on tip deflection.

displacement for the sandwich structure is much larger than that for the surface-mounted beam.

The effect of actuator length on the actuation performance of the two structures is investigated. The central location of the actuators for both beams is fixed at $d = 1.5$ cm. The transverse displacements at the free tip for different actuator lengths are shown in figure 5. It is seen that the tip displacement increases with increasing length of the actuators for the surface-mounted beam, while the tip displacement levels off with increasing actuator length for the sandwich structure. This result indicates that the sandwich structure is efficient with relatively small actuators. For longer actuators (> 1 cm) the induced tip displacement is larger for the surface-mounted beam than that for the sandwich structure.

4. Stress distribution

Very fine meshes are required for an accurate analysis of the stress field. In order to avoid excess computation time, the dimensions of the two beams are altered to $L = 2$ cm, $t = 0.1$ cm and $h = 0.4$ cm. The length of the piezoelectric actuator is assumed to be $a = 1$ cm. The central location of the actuator is placed at $d = 1$ cm from the fixed end ($x = 0$). Figure 6 shows the typical finite-element meshes.

4.1. Stress distributions due to mechanical loading

The stress distributions along the thickness under mechanical loading for the two structures are analysed. The piezoelectric actuators are open-circuited. A concentrated

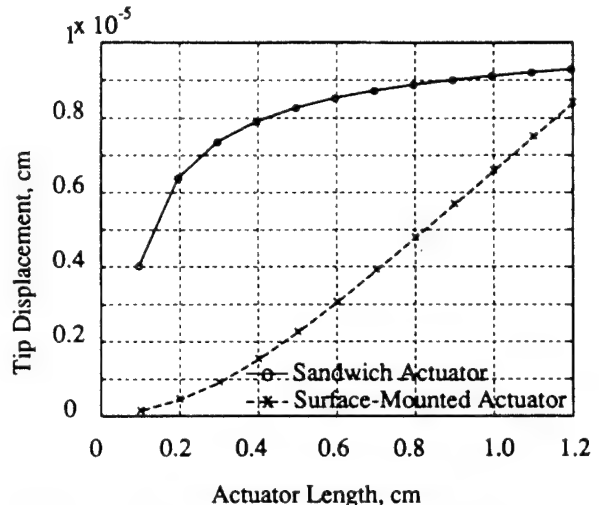


Figure 5. Effect of actuator length on tip deflection for small actuator.

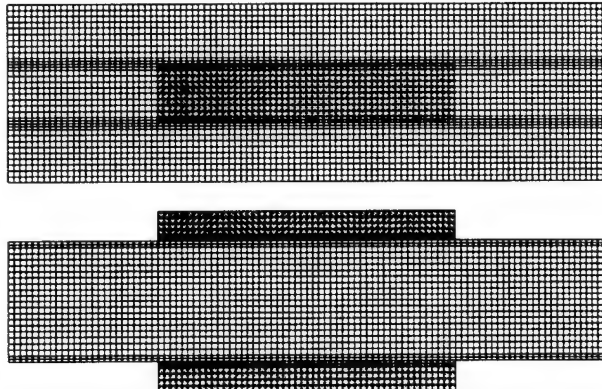


Figure 6. Finite-element models for stress calculations.

transverse load $P = 100$ N is applied at the free end of the beam. The axial (bending)-stress and shear-stress distributions at $x = 1$ cm for the two structures are shown in figures 7 and 8, respectively. All the stresses are taken from the Gauss points. As seen from figure 7, the overall axial-stress distributions for both structures are similar. However, the stress levels within the actuators for the two structures are very different due to their different locations along the thickness directions. For the sandwich structure, the actuator sustains the lowest bending stress level within the structure, because the piezoelectric core is located near the neutral plane of the beam. For the surface-mounted actuation beam, the piezoelectric actuators bear the largest bending stress level in the structure, since the actuators are located at the furthest locations from the neutral plane.

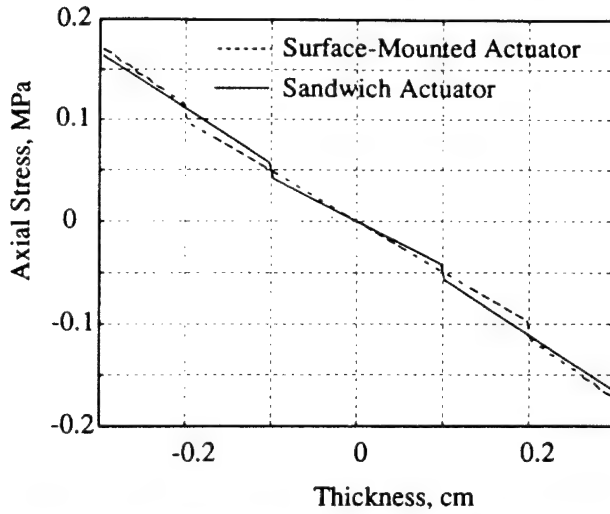


Figure 7. Axial stress distribution through the thickness at $d = 1$ cm under mechanical loading.

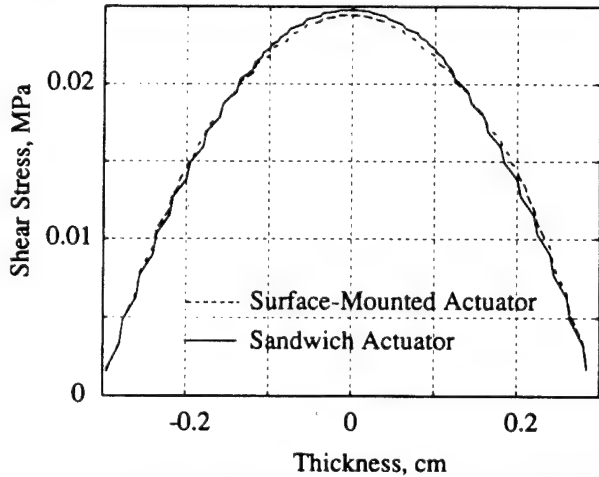


Figure 8. Shear stress distribution through the thickness at $d = 1$ cm under mechanical loading.

From figure 8, the shear-stress level within the actuator for the sandwich structure is larger than that for the surface-mounted actuation beam. However, the overall shear-stress level is much lower than the overall bending-stress level for both structures. In general, for slender beams, the transverse shear stress is small compared with the bending stress. Therefore, it is concluded that the stress level within the actuators is much more severe for the surface-mounted actuation beam than for the sandwich structure.

4.2. Stress distributions due to electrical loading

To study the stress distributions under electrical loading, no mechanical loads are applied. However, a static voltage of $V_1 = 20$ V is applied at the top and bottom surfaces of the piezoelectric core for the sandwich case, and a voltage of $V_2 = 10$ V is applied at each of the actuators for the surface-mounted actuation beam.

The axial stress distributions through the thickness at location $d = 1$ cm for the two beams are shown in figure 9.

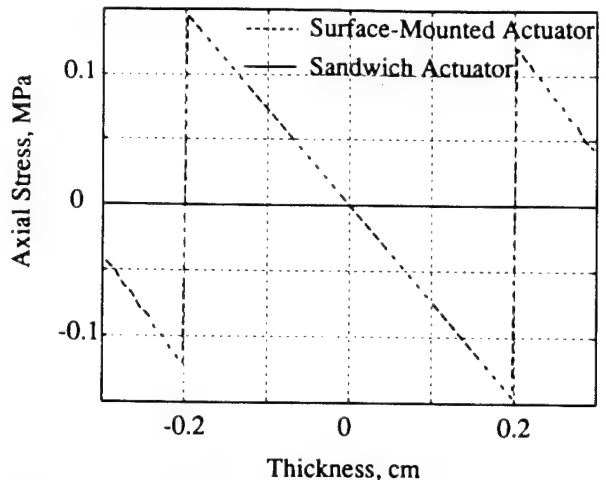


Figure 9. Axial stress distribution through the thickness at $d = 1$ cm under electrical loading.

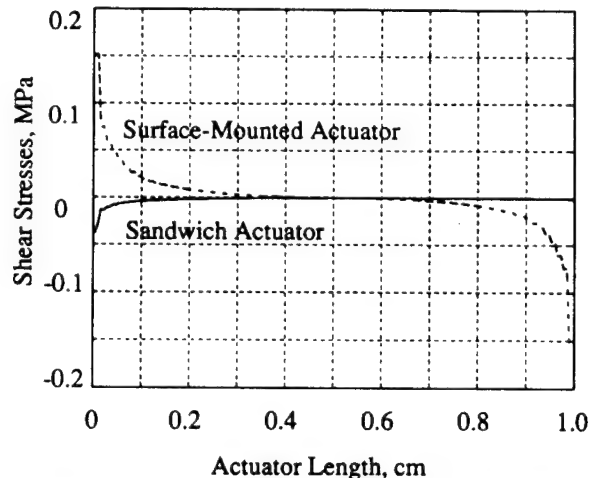


Figure 10. Interface-shear-stress distribution along the length of the actuator.

It is evident that the level of axial stress in the surface-mounted actuators is very high, and is very small in the piezoelectric core of the sandwich beam. The shear stresses for both structures are negligible at this location.

4.3. Interface stresses due to electrical loading

Of interest also are the interface stresses between the actuator and the host structure, since the actuation force is transmitted by the interface. Electrical loading alone is considered. Figures 10 and 11 show the distributions of the interface shear stress and normal stress, respectively. Stress concentrations near the ends of the actuator are evident. However, for the sandwich beam, the stress concentration occurs only at the left end of the actuator. This is a result of the fact that the left end of the sandwich beam is fixed and the load transfer from the actuator to the face sheets takes place at the left end of the actuator. Moreover, interface stresses in the sandwich beam are much lower and, consequently, debonding is less likely.

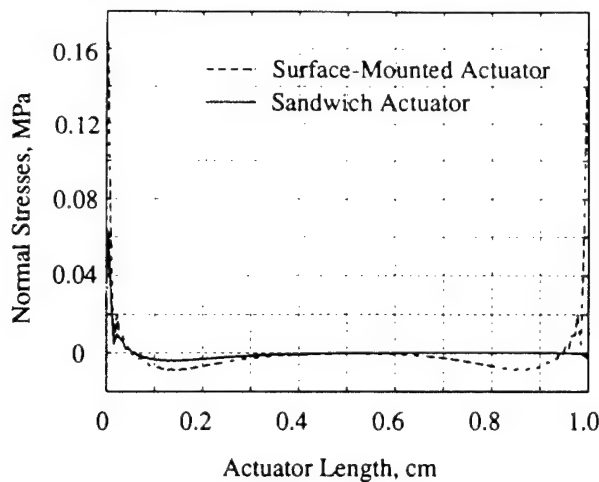


Figure 11. Interface-normal-stress distribution along the length of the actuator.

5. Discussion and conclusion

According to the results shown in figure 5, it is clear that the present adaptive sandwich structure and the surface-mounted actuation structure have different actuation characteristics. For short actuators with large thickness ratios (ratios of the total thickness of the host structure to the total thickness of the actuators), the actuation performance of the sandwich beam is superior to that of the surface-mounted actuation structure. However, with the length of actuators increased or the thickness ratio reduced, the induced tip deflection of the surface-mounted actuation structure will exceed that of the sandwich beam. As shown in figure 5, the tip deflection for the sandwich beam reaches a saturated value, and cannot be significantly increased by increasing the actuator length. For the surface-mounted case, however, the tip deflection increases with increasing the actuator length, thus providing a greater actuation capability.

From engineering practice, the two actuation schemes

may be suitable for different applications. For vibration control, the sandwich beam is more suitable for the high-frequency, small-amplitude case. The surface-mounted actuation structure may be used for the low-frequency, large-amplitude case. Although the actuation performance for the surface-mounted case increases with increasing the actuator length, the structure will suffer significant weight penalties due to the high density of piezoceramics. Furthermore, the additional mass may alter the dynamic behavior of the host structure. From the weight consideration, the sandwich beam is more efficient than the surface-mounted actuation structure.

The greatest advantage provided by the adaptive sandwich beam is its lower stresses in the actuator and along the interface between the actuator and the host structure. Since piezoceramics are very brittle, high stresses are detrimental to the structural integrity of the actuator. Long-term usage of the actuator can be ensured if stresses in the actuator are low. Low interface stresses would minimize the likelihood of debonding of the actuator from the host structure.

Acknowledgment

This work was supported by AFOSR through grant F 49620-92-J-0457 to Purdue University.

References

- [1] Crawley E and de Luis J 1987 Use of piezoceramic actuators as elements of intelligent structures *AIAA J.* **25** 1373-85
- [2] Uchino K 1986 Electrostrictive actuators: materials and applications *Ceram. Bull.* **65** 647-52
- [3] Crawley E and Anderson E 1989 Detailed models of piezoelectric actuation of beams *Proc. 30th AIAA/ASME/SAE Structures, Structural Dynamics, and Materials Conference* (Washington, DC, 1989) pp 2000-10
- [4] Lee C K 1990 Theory of laminated piezoelectric plates for the design of distributed sensors/actuators. part I: governing equations and reciprocal relationships *J. Acous. Soc. Am.* **87** 1144-58

Formulation of an Adaptive Sandwich Beam

X.D. Zhang and C.T. Sun

School of Aeronautics and Astronautics
Purdue University
West Lafayette, Indiana 47907-1282

ABSTRACT

A new adaptive sandwich structure is constructed using the shear mode of piezoelectric materials. Governing equations for the proposed beam and its surface-mounted counterpart are derived based on the variational principle. Static solutions of a cantilever sandwich beam and its corresponding surface-mounted beam are obtained based on the derived general formulations. The theoretical formulations are verified by finite element analysis. Furthermore, stress distributions of the two types of adaptive beams are also theoretically investigated. It is shown that sandwich construction offers many advantages over conventional actuation structure.

Keywords: piezoceramic, adaptive structure, sandwich beam

1 INTRODUCTION

An increasing number of applications of piezoelectric actuators have been proposed and demonstrated in recent years.^{1,2} Many analytical models have been proposed to describe and predict the interactions between piezoelectric actuators and host structures. From the force equilibrium consideration, Crawley and deLuis¹ developed a uniform strain model for a beam with piezoelectric actuators bonded on the surface or embedded in it. The model also incorporated shear lag effects of the adhesive layer between the piezoelectric actuator and the beam. Later, Crawley and Anderson³ proposed a Bernoulli-Euler beam model based on the assumption that the entire cross-section of both host structure and actuators undergoes consistent Bernoulli-Euler strains. By comparing the two models, it was shown that the uniform-strain model can accurately predict extension but not bending and that the Bernoulli-Euler model can accurately predict both. Lee⁴ treated induced strain as equivalent thermal effects and presented a model based on classical laminate theory. Recently, Leibowitz and Vinson⁵ proposed a similar but more general model which may include elastic layers, soft core layers or piezoelectric layers using Hamilton's principle.

Piezoelectric actuators in an adaptive structure are either surface-bonded or embedded in the host structure. Although effective in actuation, surface-bonded actuators are susceptible to damage inflicted by contact with surrounding objects. Furthermore, being placed at extreme thickness positions of the structure, the actuator would be subjected to high bending stresses which may prove to be detrimental to the brittle piezoceramic material. Embedding actuators in composite structures is possible. However, to accommodate the actuator, the composite material must be cut and removed, causing possible reduction in stiffness, strength, and durability of the host structure.

Recently, Sun and Zhang⁶ proposed an adaptive sandwich structure consisting of stiff facing sheets and a piezoelectric core. The piezoelectric core is positioned in such a way that an electric field in the thickness direction would generate the thickness (or transverse) shear deformation of the core. The transverse shear deformation in the core would give rise to the desired transverse deflection of the sandwich. This new sandwich construction offers many advantages over conventional surface-mounted constructions. For example, stresses in the piezoelectric core are much lower for achieving the same deflection of the structure. Moreover, the sandwich offers much better structural bending stiffness than do conventional designs.

In order to demonstrate the effectiveness of the new adaptive sandwich structure, the corresponding surface-mounted actuation structure is used as a reference throughout this study. Formulations of the sandwich structure with a piezoelectric layer and its surface-mounted counterpart are derived using variational principles. The stress distributions of two structures are obtained using these equations. These formulations are verified by finite element analysis.

2 PRELIMINARY CONSIDERATIONS

For piezoelectric ceramics (with 6mm symmetry), the materials are transversely isotropic. The constitutive relation can be represented in terms of the reduced tensor notation with respect to 1-2-3 axes of piezoelectric material:

$$\left\{ \begin{array}{l} D_1 \\ D_2 \\ D_3 \\ \sigma_1 \\ \sigma_2 \\ \sigma_3 \\ \sigma_4 \\ \sigma_5 \\ \sigma_6 \end{array} \right\} = \left[\begin{array}{ccccccc} \epsilon_1^S & 0 & 0 & 0 & 0 & 0 & 0 & e_{15} & 0 \\ 0 & \epsilon_1^S & 0 & 0 & 0 & 0 & e_{15} & 0 & 0 \\ 0 & 0 & \epsilon_3^S & e_{31} & e_{31} & e_{33} & 0 & 0 & 0 \\ 0 & 0 & -e_{31} & c_{11}^E & c_{12}^E & c_{13}^E & 0 & 0 & 0 \\ 0 & 0 & -e_{31} & c_{12}^E & c_{11}^E & c_{13}^E & 0 & 0 & 0 \\ 0 & 0 & -e_{33} & c_{13}^E & c_{13}^E & c_{33}^E & 0 & 0 & 0 \\ 0 & -e_{15} & 0 & 0 & 0 & 0 & c_{44}^E & 0 & 0 \\ -e_{15} & 0 & 0 & 0 & 0 & 0 & 0 & c_{44}^E & 0 \\ 0 & 0 & 0 & 0 & 0 & 0 & 0 & 0 & c_{66}^E \end{array} \right] \left\{ \begin{array}{l} E_1 \\ E_2 \\ E_3 \\ \epsilon_1 \\ \epsilon_2 \\ \epsilon_3 \\ \epsilon_4 \\ \epsilon_5 \\ \epsilon_6 \end{array} \right\} , \quad (1)$$

where σ_i , ϵ_i , D_i and E_i are the components of the reduced stress tensor, reduced strain tensor, electric displacement vector and the electric field vector, respectively. The coefficients c_{ij}^E are the elastic constants measured at constant electric field. The components e_{ij} denote piezoelectric constants. The coefficients ϵ_i^S represent the components of the dielectric permittivity tensor measured at constant strain. In the above equation, the 3-direction is always the poling direction, and the 1-2 plane is an isotropic plane.

For simplicity in notation, the superscripts in the above equation will be henceforth omitted. The electric field-electric potential relations are given by

$$E_k = -\psi_{,k} , \quad (2)$$

where ψ is the electric potential function.

Hamilton's principle for variations of the independent kinematic variables at any time interval $[t_0, t_1]$ can be written as⁷

$$\delta \int_{t_0}^{t_1} L dt + \int_{t_0}^{t_1} \delta W dt = 0 , \quad (3)$$

where L is the Lagrangian for a system, and δW denotes the virtual work done by the external forces.

Let a piezoelectric body with surface S and volume V be subjected to a prescribed surface traction t_k and surface charge per unit area $\bar{\sigma}$. The total virtual work δW is

$$\delta W = \int_S (t_k \delta u_k - \bar{\sigma} \delta \psi) dS , \quad (4)$$

where $t_k \delta u_k$ represents the virtual work per unit area done by the prescribed surface traction in a small virtual displacement of the surface; $\bar{\sigma} \delta \psi$ denotes the electrical analog of the virtual work per unit area done by the prescribed surface charge $\bar{\sigma}$ in a small variation $\delta \psi$ of the electrical potential ψ .

The Lagrangian L for the piezoelectric body is defined by⁷

$$L = \int_V \left[\frac{1}{2} \rho \dot{u}_j \dot{u}_j - H(\varepsilon_{kl}, E_k) \right] dV , \quad (5)$$

where \dot{u}_j is the time derivative of the displacement u_j , $H(\varepsilon_{kl}, E_k)$ is the electrical enthalpy which is an energy quantity similar to strain energy.

From the thermodynamic argument, it is shown that electrical enthalpy is a function of only the infinitesimal strain-tensor components ε_{kl} and the electrical-field intensity E_k . The simplest form of electrical enthalpy which is compatible with thermodynamics can be constructed for linear theory as

$$H = \frac{1}{2} c_{ijkl} \varepsilon_{ij} \varepsilon_{kl} - e_{ijk} E_i \varepsilon_{jk} - \frac{1}{2} \varepsilon_{ij} E_i E_j . \quad (6)$$

Substituting the constitutive equations of the piezoelectric materials into the above equation, the electrical enthalpy can be simplified as

$$H = \frac{1}{2} \sigma_{ij} \varepsilon_{ij} - \frac{1}{2} E_i D_i . \quad (7)$$

Combining Eqns. (3), (4), (5) and (7), one may arrange the variational principle for the piezoelectric media as follows

$$\delta \int_{t_0}^{t_1} \int_V \left[\frac{1}{2} \rho \dot{u}_j \dot{u}_j - \frac{1}{2} \sigma_{ij} \varepsilon_{ij} + \frac{1}{2} E_i D_i \right] dV dt + \int_{t_0}^{t_1} \int_S (t_k \delta u_k - \bar{\sigma} \delta \psi) dS dt = 0 . \quad (8)$$

The above equation will be used directly in our formulation.

3 FORMULATIONS OF A PIEZOELECTRIC SANDWICH BEAM AND A SURFACE-MOUNTED ACTUATION BEAM

3.1 Formulation of a Piezoelectric Sandwich Beam

The underlying principle of sandwich construction can be illustrated as follows. In a sandwich construction (see Fig. 1), the top and bottom layers are stiff facing sheets, and the central layer is a piezoelectric core in which the poling direction of the piezoelectric material is arranged along the x-direction. When an electric field is applied along the z-direction, the piezoelectric core will produce a pure shear deformation which is the driving force for the transverse deflection of the sandwich construction. The shear deformation of the core is depicted in Fig. 2.

In this section, a set of fully-coupled electromechanical governing equations for the sandwich beam is formulated. In order to simplify the formulation procedure, the following assumptions are introduced:

1. In each layer, the normal stress, σ_z , is assumed to vanish.
2. Each layer is in a state of plane strain parallel to the x-z plane.
3. The piezoelectric material for this application is assumed to be transversely isotropic. The piezoelectric constants are e_{31} , e_{33} and e_{15} .
4. The interfaces between different layers are perfectly bonded.
5. The transverse displacements (i.e., the displacement along the z-direction) in the layers are equal.
6. The top and bottom layers are assumed to be linear elastic Bernoulli-Euler beams, namely, the transverse shear strains in the layers will be neglected. The

central core is assumed to be a Timoshenko beam, which allows transverse shear deformation.

7. The sandwich beam is assumed to have unit width.
8. The two surfaces of piezoelectric layer are entirely covered with electrode. Therefore, the electric potential will be independent of axial location.

Consider the k th layer of the sandwich beam. The displacement field and the electrical potential in this layer are assumed to be of the form

$$\begin{cases} \bar{u}^{(k)} &= u^{(k)}(x, t) + z^{(k)} \phi^{(k)}(x, t) \\ \bar{w}^{(k)} &= w(x, t) \\ \bar{\psi}^{(k)} &= \psi^{(k)}(t) + z^{(k)} \psi_1^{(k)}(t), \end{cases} \quad (9)$$

where $z^{(k)}$ is the thickness-coordinate with the origin located at the mid-plane of the k th layer, $\phi^{(k)}$ gives the rotation of the cross-section, $\psi^{(k)}$ and $\psi_1^{(k)}$ denote the electrical potential and its gradient at the mid-plane of the k th layer, respectively, whereas $u^{(k)}$ and $w^{(k)}$ represent the displacements at the mid-plane of the k th layer in the x - and z -directions, respectively. In the above equations, the electrical potential and its gradient are set to vanish for the non-piezoelectric layers.

The above expressions for the displacements in each layer can be used to calculate the strain components. According to assumption 6, the strain components can be obtained as

$$\begin{cases} \varepsilon_x^{(k)} &= \frac{\partial u^{(k)}}{\partial x} - z^{(k)} \frac{\partial^2 w}{\partial x^2} \\ \gamma_{xz}^{(k)} &= 0, \end{cases} \quad (10)$$

for $k = 1, 3$ (the face sheets). Note that for the Bernoulli-Euler beam, $\phi^{(k)} = -\frac{\partial w}{\partial x}$.

For the piezoelectric core, the strain components can be similarly written as

$$\begin{cases} \varepsilon_x^{(c)} &= \frac{\partial u^{(c)}}{\partial x} + z^{(c)} \frac{\partial \phi^{(c)}}{\partial x} \\ \gamma_{xz}^{(c)} &= \phi^{(c)} + \frac{\partial w}{\partial x}, \end{cases} \quad (11)$$

where superscript (c) instead of "2" is used.

The electrical potential for the top and bottom layers vanishes as stated before. The electrical variables are involved only in the piezoelectric core. For simplicity, superscript (c) for electrical variables is neglected. The electrical field intensity for the piezoelectric core can be obtained using Eqs. (2) and (9)

$$\begin{cases} E_x = 0 \\ E_y = 0 \\ E_z = -\psi_1 . \end{cases} \quad (12)$$

The reduced stress-strain relation for the face sheets is

$$\sigma_x^{(k)} = Q_{11}^{(k)} \varepsilon_x^{(k)} \quad (k = 1, 3) , \quad (13)$$

where $Q_{11}^{(k)} = c_{11}^{(k)} - \frac{c_{13}^{(k)2}}{c_{33}^{(k)}}$. Using Eq. (1) and assumptions 1 and 2, the constitutive equations for the piezoelectric core can be derived. We have

$$\begin{cases} \sigma_x^{(c)} = Q_{33}^E \varepsilon_x^{(c)} \\ \sigma_{xz}^{(c)} = Q_{55}^E \gamma_{xz}^{(c)} - e_{15} E_z , \end{cases} \quad (14)$$

for the stress components and

$$\begin{cases} D_x = e_{33}^x \varepsilon_x^{(c)} \\ D_y = 0 \\ D_z = \epsilon_{11} E_z + e_{15} \gamma_{xz}^{(c)} , \end{cases} \quad (15)$$

for the electrical-displacement components, where

$$\begin{aligned} Q_{33}^E &= c_{33} - \frac{c_{13}^2}{c_{11}} & e_{33}^x &= e_{33} - \frac{c_{13} e_{31}}{c_{11}} \\ Q_{55}^E &= c_{55} & \epsilon_{33}^x &= \epsilon_{33} + \frac{e_{31}^2}{c_{11}} , \end{aligned}$$

are newly defined material constants.

The kinetic energy per unit length of the k th layer can be obtained as

$$T^{(k)} = \frac{1}{2} \rho_k \int_{-\frac{t_k}{2}}^{\frac{t_k}{2}} [(\dot{\bar{u}}^{(k)})^2 + \dot{w}^2] dz^{(k)} , \quad (16)$$

where t_k and ρ_k are the thickness and the density of the k th layer, respectively. The local kinetic energy $T^{(k)}$ can be expressed in terms of the displacement components at the mid-plane of the k th layer, $u^{(k)}$, $w^{(k)}$ ($= w$), and the rotation $\phi^{(k)}$ by integrating the above expression

$$T^{(k)} = \frac{1}{2} \rho_k t_k [(\dot{u}^{(k)})^2 + \dot{w}^2] + \frac{1}{24} \rho_k t_k^3 (\dot{\phi}^{(k)})^2. \quad (17)$$

Note that for the face sheets ($k = 1, 3$), $\phi^{(k)} = -\frac{\partial w}{\partial x}$. The total kinetic energy per unit length of the sandwich beam is

$$T = \sum_k T^{(k)}. \quad (18)$$

A similar expression for the electrical enthalpy of the sandwich beam based upon Eqs. (10-15) can be written as

$$H = \sum_k H^{(k)}, \quad (19)$$

where

$$H^{(k)} = \frac{1}{2} Q_{11}^{(k)} t_k (\frac{\partial u^{(k)}}{\partial x})^2 + \frac{1}{24} Q_{11}^{(k)} t_k^3 (\frac{\partial^2 w}{\partial x^2})^2, \quad (20)$$

for $k = 1, 3$, and

$$\begin{aligned} H^{(c)} = & \frac{1}{2} Q_{33}^E t_c (\frac{\partial u^{(c)}}{\partial x})^2 + \frac{1}{24} Q_{33}^E t_c^3 (\frac{\partial \phi^{(c)}}{\partial x})^2 + \frac{1}{2} Q_{55}^E t_c (\phi^{(c)} + \frac{\partial w}{\partial x})^2 \\ & + e_{15} \psi_1 t_c (\phi^{(c)} + \frac{\partial w}{\partial x}) - \frac{1}{2} \epsilon_{11} \psi_1^2 t_c, \end{aligned} \quad (21)$$

for the piezoelectric core.

In order to simplify the formulation, the top and bottom face sheets are assumed to have the same thickness, t , the same mass density, ρ , and the same mechanical properties ($Q_{11}^{(1)} = Q_{11}^{(3)} = Q_{11}$). The thickness and mass density of the piezoelectric core are denoted as t_c and ρ_c , respectively. The interface condition on the displacements given by Eqs. (9) leads to

$$\begin{cases} u^{(1)} = u^{(c)} + \frac{t}{2} \frac{\partial w}{\partial x} - \frac{t_c}{2} \phi^{(c)} \\ u^{(3)} = u^{(c)} - \frac{t}{2} \frac{\partial w}{\partial x} + \frac{t_c}{2} \phi^{(c)}. \end{cases} \quad (22)$$

Using the above equation, $u^{(1)}$ and $u^{(3)}$ can be eliminated from Eqs. (18) and (19). Accordingly, the kinetic-energy function T and the electrical enthalpy of the sandwich beam can be written in terms of the in-plane displacement $u^{(c)}$, transverse displacement w , local rotation $\phi^{(c)}$, and the electrical field variable ψ_1 . The result is

$$T = (\rho t + \frac{1}{2} \rho_c t_c) \dot{u}^{(c)2} + \frac{1}{3} \rho t^3 (\frac{\partial^2 w}{\partial x \partial t})^2 + (\rho t + \frac{1}{2} \rho_c t_c) (\dot{w})^2 \\ (\frac{\rho t t_c^2}{4} + \frac{\rho_c t_c^3}{24}) \dot{\phi}^{(c)2} - \frac{\rho t^2 t_c}{2} \frac{\partial^2 w}{\partial x \partial t} \dot{\phi}^{(c)}, \quad (23)$$

and

$$H = (Q_{11} t + \frac{1}{2} Q_{33}^E t_c) (\frac{\partial u^{(c)}}{\partial x})^2 + \frac{1}{3} Q_{11} t^3 (\frac{\partial^2 w}{\partial x^2})^2 - \frac{1}{2} Q_{11} t^2 t_c \frac{\partial^2 w}{\partial x^2} \frac{\partial \phi^{(c)}}{\partial x} \\ + (\frac{1}{4} Q_{11} t t_c^2 + \frac{1}{24} Q_{33}^E t_c^3) (\frac{\partial \phi^{(c)}}{\partial x})^2 + \frac{1}{2} Q_{55}^E t_c (\phi^{(c)} + \frac{\partial w}{\partial x})^2 \\ + \epsilon_{15} \psi_1 t_c (\phi^{(c)} + \frac{\partial w}{\partial x}) - \frac{1}{2} \epsilon_{11} \psi_1^2 t_c. \quad (24)$$

According to Eq. (4), the total virtual work δW done by the applied forces and prescribed surface charge for the sandwich beam can be assumed as follows

$$\delta W = \int_0^L q \delta w dx + \sum_{k=1}^3 M^{(k)} \delta \phi^{(k)} |_0^L + \sum_{k=1}^3 N^{(k)} \delta u^{(k)} |_0^L + \sum_{k=1}^3 Q^{(k)} \delta w^{(k)} |_0^L, \quad (25)$$

where q denotes the pressure acting along the transverse direction; $M^{(k)}$, $N^{(k)}$ and $Q^{(k)}$ represent the applied moment, axial force and transverse shear force in the k th layer, respectively.

Substituting Eqs. (23-25) into Eq. (8), one may obtain the variational form of the sandwich beam as

$$\delta \int_{t_0}^{t_1} \int_0^L \{ (\rho t + \frac{1}{2} \rho_c t_c) \dot{u}^{(c)2} + \frac{1}{3} \rho t^3 (\frac{\partial^2 w}{\partial x \partial t})^2 + (\rho t + \frac{1}{2} \rho_c t_c) (\dot{w})^2 \\ + (\frac{\rho t t_c^2}{4} + \frac{\rho_c t_c^3}{24}) \dot{\phi}^{(c)2} - \frac{\rho t^2 t_c}{2} \frac{\partial^2 w}{\partial x \partial t} \dot{\phi}^{(c)} - (Q_{11} t + \frac{1}{2} Q_{33}^E t_c) (\frac{\partial u^{(c)}}{\partial x})^2 \\ - \frac{1}{3} Q_{11} t^3 (\frac{\partial^2 w}{\partial x^2})^2 + \frac{1}{2} Q_{11} t^2 t_c \frac{\partial^2 w}{\partial x^2} \frac{\partial \phi^{(c)}}{\partial x} - (\frac{1}{4} Q_{11} t t_c^2 + \frac{1}{24} Q_{33}^E t_c^3) (\frac{\partial \phi^{(c)}}{\partial x})^2 \\ - \frac{1}{2} Q_{55}^E t_c (\phi^{(c)} + \frac{\partial w}{\partial x})^2 - \epsilon_{15} \psi_1 t_c (\phi^{(c)} + \frac{\partial w}{\partial x}) + \frac{1}{2} \epsilon_{11} \psi_1^2 t_c \} dx dt \quad (26)$$

$$+ \int_{t_0}^{t_1} \left[\int_0^L q \delta w dx + M \delta \phi^{(c)} |_0^L + M_1 \delta \left(\frac{\partial w}{\partial x} \right) |_0^L + N \delta u^{(c)} |_0^L + Q \delta w |_0^L \right] dt = 0 .$$

where $M = M^{(c)} - (N^{(1)} - N^{(3)}) \frac{t_c}{2}$, $M_1 = -M^{(1)} - M^{(3)} + (N^{(1)} - N^{(3)}) \frac{t}{2}$, $N = N^{(1)} + N^{(c)} + N^{(3)}$ and $Q = Q^{(1)} + Q^{(c)} + Q^{(3)}$. By taking variation of the above equation and collecting terms for different independent kinematic variables, the equations of motion of the sandwich beam are obtained as follows

$$\begin{aligned} (2Q_{11}t + Q_{33}^E t_c) \frac{\partial^2 u^{(c)}}{\partial x^2} &= (2\rho t + \rho_c t_c) \frac{\partial^2 u^{(c)}}{\partial t^2} \\ \left(\frac{1}{2} Q_{11} t t_c^2 + \frac{1}{12} Q_{33}^E t_c^3 \right) \frac{\partial^2 \phi^{(c)}}{\partial x^2} - \frac{1}{2} Q_{11} t^2 t_c \frac{\partial^3 w}{\partial x^3} - Q_{55}^E t_c (\phi^{(c)} + \frac{\partial w}{\partial x}) \\ + \frac{1}{2} \rho t^2 t_c \frac{\partial^3 w}{\partial x \partial t^2} - e_{15} t_c \psi_1 &= \left(\frac{\rho t t_c^2}{2} + \frac{\rho_c t_c^3}{12} \right) \frac{\partial^2 \phi^{(c)}}{\partial t^2} \quad (27) \\ \frac{2}{3} \rho t^3 \frac{\partial^4 w}{\partial x^2 \partial t^2} - \frac{2}{3} Q_{11} t^3 \frac{\partial^4 w}{\partial x^4} + \frac{1}{2} Q_{11} t^2 t_c \frac{\partial^3 \phi^{(c)}}{\partial x^3} + Q_{55}^E t_c \left(\frac{\partial \phi^{(c)}}{\partial x} + \frac{\partial^2 w}{\partial x^2} \right) \\ - \frac{\rho t^2 t_c}{2} \frac{\partial^3 \phi^{(c)}}{\partial x \partial t^2} + q &= (2\rho t + \rho_c t_c) \frac{\partial^2 w}{\partial t^2} , \end{aligned}$$

and associated boundary conditions at $x = 0, L$ are

$$\begin{aligned} N &= [(2Q_{11}t + Q_{33}^E t_c) \frac{\partial u^{(c)}}{\partial x}] \text{ or } \delta u^{(c)} = 0 \\ M &= \left[\left(\frac{1}{2} Q_{11} t t_c^2 + \frac{1}{12} Q_{33}^E t_c^3 \right) \frac{\partial \phi^{(c)}}{\partial x} - \frac{1}{2} Q_{11} t^2 t_c \frac{\partial^2 w}{\partial x^2} \right] \text{ or } \delta \phi^{(c)} = 0 \\ M_1 &= \left[-\frac{1}{2} Q_{11} t^2 t_c \frac{\partial \phi^{(c)}}{\partial x} + \frac{2}{3} Q_{11} t^3 \frac{\partial^2 w}{\partial x^2} \right] \text{ or } \delta \left(\frac{\partial w}{\partial x} \right) = 0 \quad (28) \\ Q &= \left[\frac{2}{3} \rho t^3 \frac{\partial^3 w}{\partial x \partial t^2} - \frac{\rho t^2 t_c}{2} \frac{\partial^2 \phi^{(c)}}{\partial t^2} - \frac{2}{3} Q_{11} t^3 \frac{\partial^3 w}{\partial x^3} + \frac{1}{2} Q_{11} t^2 t_c \frac{\partial^2 \phi^{(c)}}{\partial x^2} \right. \\ &\quad \left. + Q_{55}^E t_c (\phi^{(c)} + \frac{\partial w}{\partial x}) + e_{15} t_c \psi_1 \right] \text{ or } \delta w = 0 . \end{aligned}$$

The above expressions yield the necessary boundary conditions and the natural boundary conditions.

3.2 Formulation of a Surface-Mounted Actuation Beam

For surface-mounted actuation beams, the poling directions of two piezoelectric layers are assumed to be along the z-direction. The electric potentials applied to the two piezoelectric layers have the same magnitude but opposite directions. Similar to

the above formulation of an adaptive sandwich beam, the governing equations of a surface-mounted actuation beam can be obtained as follows

$$(2Q_{11}^E t + Q_{11} t_c) \frac{\partial^2 u^{(c)}}{\partial x^2} = (2\rho t + \rho_c t_c) \frac{\partial^2 u^{(c)}}{\partial t^2} - [\frac{1}{6} Q_{11}^E t^3 + \frac{1}{2} Q_{11}^E (t + t_c)^2 t + \frac{1}{12} Q_{11} t_c^3] \frac{\partial^4 w}{\partial x^4} + [\frac{1}{6} \rho t^3 + \frac{1}{2} \rho (t + t_c)^2 t + \frac{1}{12} \rho_c t_c^3] \frac{\partial^4 w}{\partial x^2 \partial t^2} + q = (2\rho t + \rho_c t_c) \frac{\partial^2 w}{\partial t^2}, \quad (29)$$

where Q_{11} is the reduced stiffness of the host structure, and

$$Q_{11}^E = c_{11} - \frac{c_{13}^2}{c_{33}} \quad e_{31}^X = e_{31} - \frac{c_{13} e_{33}}{c_{33}},$$

are newly defined material constants. Unlike the sandwich beam, t_c and t refer to the thickness of the host structure and the thickness of each actuator for the surface-mounted case, respectively.

The corresponding boundary conditions at $x = 0, L$ can be obtained as

$$\begin{aligned} N &= [(2Q_{11}^E t + Q_{11} t_c) \frac{\partial u^{(c)}}{\partial x}] \quad \text{or} \quad \delta u^{(c)} = 0 \\ M &= [(\frac{1}{6} Q_{11}^E t^3 + \frac{1}{2} Q_{11}^E (t + t_c)^2 t + \frac{1}{12} Q_{11} t_c^3) \frac{\partial^2 w}{\partial x^2} + e_{31}^X (t + t_c) t \psi_1] \\ &\quad \text{or} \quad \delta(\frac{\partial w}{\partial x}) = 0 \\ Q &= [(\frac{1}{6} \rho t^3 + \frac{1}{2} \rho (t + t_c)^2 t + \frac{1}{12} \rho_c t_c^3) \frac{\partial^3 w}{\partial x \partial t^2} \\ &\quad - (\frac{1}{6} Q_{11}^E t^3 + \frac{1}{2} Q_{11}^E (t + t_c)^2 t + \frac{1}{12} Q_{11} t_c^3) \frac{\partial^3 w}{\partial x^3}] \quad \text{or} \quad \delta w = 0. \end{aligned} \quad (30)$$

4 VERIFICATION OF THE FORMULATIONS

Figure 3 shows the geometries of an adaptive sandwich beam and a surface-mounted actuation beam. Both beams are fixed at the end $x = 0$, and free at the end $x = L$. In order to verify the effectiveness of the sandwich structure, the actuation behavior of the sandwich beam is compared with that of the corresponding surface-mounted actuation beam. The total thickness of the two piezoelectric layers

in the surface-mounted beam is equal to the thickness of the piezoelectric core in the sandwich beam, and the beam thickness of the surface-mounted case is equal to the sum of thicknesses of the top and bottom sheets of the sandwich beam.

The static solutions of the two beams under a concentrated load and electrical voltage are formulated. The above formulations are verified by comparing the static analytical solutions of the two beams with the corresponding finite element results.

4.1 Adaptive Sandwich Beam

It is very difficult to find general solutions for fully coupled electromechanical governing equations of the sandwich beam. For the adaptive sandwich beam, a concentrated load, Q , is applied at the free end. Voltage is applied at the top and bottom surfaces of piezoelectric core as an actuation force. Considering the static case, the time derivatives of all variables in the formulation are subject to vanish. According to Eqs. (27), the equations of motion for this static sandwich beam can be obtained as

$$\begin{aligned} \frac{\partial^2 u^{(c)}}{\partial x^2} &= 0 \\ -\frac{2}{3} Q_{11} t^3 \frac{\partial^4 w}{\partial x^4} + \frac{1}{2} Q_{11} t^2 t_c \frac{\partial^3 \phi^{(c)}}{\partial x^3} + Q_{55}^E t_c (\frac{\partial \phi^{(c)}}{\partial x} + \frac{\partial^2 w}{\partial x^2}) &= 0 \quad (31) \\ (\frac{1}{2} Q_{11} t t_c^2 + \frac{1}{12} Q_{33}^E t_c^3) \frac{\partial^2 \phi^{(c)}}{\partial x^2} - \frac{1}{2} Q_{11} t^2 t_c \frac{\partial^3 w}{\partial x^3} \\ - Q_{55}^E t_c (\phi^{(c)} + \frac{\partial w}{\partial x}) + e_{15} E_z t_c &= 0. \end{aligned}$$

Assuming that the piezoelectric core is insulated on both ends, appropriate boundary conditions for the cantilever sandwich beam can be obtained as

$$\begin{aligned} u^{(c)}_{|x=0} &= 0 & \phi^{(c)}_{|x=0} &= 0 & w_{|x=0} &= 0 & \frac{\partial w}{\partial x} &= 0 \\ N = \frac{\partial u^{(c)}}{\partial x} &= 0 & M_1 = [-\frac{1}{2} Q_{11} t^2 t_c \frac{\partial \phi^{(c)}}{\partial x} + \frac{2}{3} Q_{11} t^3 \frac{\partial^2 w}{\partial x^2}]_{|x=L} &= 0 \\ M = [(\frac{1}{2} Q_{11} t t_c^2 + \frac{1}{12} Q_{33}^E t_c^3) \frac{\partial \phi^{(c)}}{\partial x} - \frac{1}{2} Q_{11} t^2 t_c \frac{\partial^2 w}{\partial x^2}]_{|x=L} &= 0 \quad (32) \\ Q = [-\frac{2}{3} Q_{11} t^3 \frac{\partial^3 w}{\partial x^3} + Q_{55}^E t_c (\phi^{(c)} + \frac{\partial w}{\partial x}) + \frac{1}{2} Q_{11} t^2 t_c \frac{\partial^2 \phi}{\partial x^2} - e_{15} E_z t_c]_{|x=L} & \end{aligned}$$

By applying the boundary conditions, Eqs. (32), to Eqs. (31), a set of static analytical solutions for the cantilever sandwich beam can be obtained as follows

$$\begin{aligned}
 u^{(c)} &= 0 \\
 \phi^{(c)} &= K_6 \left\{ 1 - \frac{\cosh[\lambda(L-x)]}{\cosh(\lambda L)} \right\} + \frac{K_5}{K_4} \left(\frac{1}{2}x - L \right) x Q \\
 w &= \frac{K_1 K_6}{K_2} \left\{ x + \frac{\sinh[\lambda(L-x)]}{\lambda \cosh(\lambda L)} - \frac{\tanh(\lambda L)}{\lambda} \right\} \\
 &\quad + \frac{1}{2K_2} \left(\frac{K_1 K_5}{K_4} - 1 \right) \left(\frac{1}{3}x^2 - Lx \right) x Q,
 \end{aligned} \tag{33}$$

where

$$\begin{aligned}
 K_1 &= \frac{1}{2} Q_{11} t t_c (t_c + t) + \frac{1}{12} Q_{33}^E t_c^3 \\
 K_2 &= \frac{1}{6} Q_{11} t^2 (4t + 3t_c) \\
 K_3 &= \frac{1}{6} Q_{11} t^2 t_c^2 + \frac{1}{9} Q_{33}^E t t_c^3 \\
 K_4 &= \frac{1}{3} (4t + 3t_c) Q_{55}^E t_c \left(1 + \frac{K_1}{K_2} \right) \\
 K_5 &= \frac{1}{3K_2} (4t + 3t_c) Q_{55}^E t_c \\
 K_6 &= \frac{1}{3K_4} (4t + 3t_c) e_{15} E_z t_c + \frac{K_3 K_5}{K_4^2} Q + \frac{t_c}{K_4} Q \\
 \lambda &= \sqrt{\frac{K_4}{K_3}}
 \end{aligned}$$

are newly defined parameters.

The top and bottom layers of the sandwich beam are assumed to be aluminum, and the central piezoelectric core is considered to be PZT5H material. The mechanical properties of the two materials are shown in Table 1. The material constant Q_{11} can be calculated as $Q_{11} = \frac{E}{1 - \nu^2}$ for this case. The geometrical parameters of the sandwich beam are assumed to be $L = 10\text{ cm}$, $t = 0.8\text{ cm}$ and $t_c = 0.2\text{ cm}$. The voltage applied between the top and bottom surfaces of the piezoelectric core is $V = 20\text{ volts}$; accordingly, the electric field intensity within the piezoelectric core can be expressed as $E_z = \frac{V}{t_c}$. Substituting the above numerical data into Eqs. (33),

the transverse displacement, w , and local rotation, $\phi^{(c)}$, can be obtained, as shown in Fig. 4 and Fig. 5, respectively.

To verify the above theoretical model, finite element analysis is performed using ANSYS code. Four-node linear plane-strain coupled elements are used for the piezoelectric actuator; and four-node linear plane-strain structural elements are used for the remaining part of the structure. The numerical data and boundary conditions shown above are used in the analysis. The transverse displacement variations along the axial locations by finite element analysis are also plotted in Fig. 4. It is clear that the theoretical solutions match very well with the finite element results. Specifically, the transverse displacement at the right tip for the finite element analysis is $1.1791 \times 10^{-5} \text{ cm}$. Compared to the theoretical solution ($1.1961 \times 10^{-5} \text{ cm}$), it has a relative error of only 1.42%.

The variation of axial displacement along the transverse direction is shown in Fig. 6. It is clear that the axial displacement varies linearly along the transverse direction. This is in agreement with the displacement assumption of Eqs. (9). For the axial location of $x < 1 \text{ cm}$, the amplitude of the axial displacement distributions through the thickness increases along the axial location. For the axial location of $x \geq 1 \text{ cm}$, the axial displacement distributions through the thickness are the same as shown in Fig. 6. These results correspond to the variations of local rotation, $\phi^{(c)}$, along axial locations (see Fig. 5). Therefore, it is concluded that the proposed theoretical model can accurately predict behavior of the sandwich beam.

4.2 Surface-Mounted Actuation Beam

For the surface-mounted actuation beam, a concentrated load, Q , is applied at the free end. The voltages applied on the two piezoelectric layers have the same magnitude

but opposite directions. The time derivatives of all variables in the formulation are subject to vanish for the static case. From Eq. (29), the governing equations of the surface-mounted actuation beam can be simplified as

$$\begin{cases} \frac{\partial^2 u^{(c)}}{\partial x^2} = 0 \\ \frac{\partial^4 w}{\partial x^4} = 0 \end{cases} \quad (34)$$

The appropriate boundary conditions for the cantilever surface-mounted beam can be written as

$$\begin{aligned} u^{(c)}|_{x=0} &= 0 & w|_{x=0} &= 0 & \frac{\partial w}{\partial x}|_{x=0} &= 0 & N = \frac{\partial u^{(c)}}{\partial x}|_{x=L} &= 0 \\ Q &= \left[-\left(\frac{1}{6} Q_{11}^E t^3 + \frac{1}{2} Q_{11}^E (t + t_c)^2 t + \frac{1}{12} Q_{11} t_c^3 \right) \frac{\partial^3 w}{\partial x^3} \right]_{x=L} & (35) \\ M &= \left[\left(\frac{1}{6} Q_{11}^E t^3 + \frac{1}{2} Q_{11}^E (t + t_c)^2 t + \frac{1}{12} Q_{11} t_c^3 \right) \frac{\partial^2 w}{\partial x^2} - e_{31}^X (t + t_c) t E_z \right]_{x=L} = 0. \end{aligned}$$

Using the above governing equations and the associated boundary conditions, a set of static analytical solutions of the surface-mounted actuation beam can be given as

$$\begin{cases} u^{(c)} = 0 \\ w = -\frac{Q}{6EI} x^3 + \frac{1}{2EI} [Q L + e_{31}^X (t + t_c) t E_z] x^2, \end{cases} \quad (36)$$

where

$$EI = \frac{1}{6} Q_{11}^E t^3 + \frac{1}{2} Q_{11}^E (t + t_c)^2 t + \frac{1}{12} Q_{11} t_c^3.$$

The geometrical parameters of the surface-mounted actuation beam are assumed to be $L = 10\text{ cm}$, $t = 0.1\text{ cm}$ and $t_c = 1.6\text{ cm}$. The voltage applied to each of the piezoelectric actuators is $V = 10\text{ volts}$. Setting $Q = 0$ and substituting the numerical data into Eqs. (36), the transverse displacement, w , is plotted as shown in Fig. 7. Analogous to the sandwich beam, the corresponding finite element results are also shown in Fig. 7. It is clear that the theoretical solution agrees very well with the finite element analysis. It should be noted that Eqs. (36) are exactly the so-called *Bernoulli-Euler model* by Crawley and Anderson³ under plane strain conditions if $Q = 0$.

5 STRESS DISTRIBUTIONS

In the above, the static solutions of the adaptive sandwich beam and the surface-mounted actuation beam have been obtained. Using these results, the stress distributions within the two beams can be calculated.

For the adaptive sandwich beam, the stress distribution can be obtained using Eqs. (9-14) and Eq. (33)

$$\sigma_x = \begin{cases} Q_{11} \left[-\frac{t_f}{2} \frac{\partial \phi^{(c)}}{\partial x} + (z + t + \frac{t_f}{2}) \frac{\partial^2 w}{\partial x^2} \right] & -\frac{t_f}{2} - t \leq z \leq -\frac{t_f}{2} \\ Q_{33}^E z \frac{\partial \phi^{(c)}}{\partial x} & -\frac{t_f}{2} \leq z \leq \frac{t_f}{2} \\ Q_{11} \left[\frac{t_f}{2} \frac{\partial \phi^{(c)}}{\partial x} + (z - t - \frac{t_f}{2}) \frac{\partial^2 w}{\partial x^2} \right] & \frac{t_f}{2} \leq z \leq \frac{t_f}{2} + t \end{cases} \quad (37)$$

where $\frac{\partial \phi^{(c)}}{\partial x}$ and $\frac{\partial^2 w}{\partial x^2}$ can be obtained as

$$\begin{aligned} \frac{\partial \phi^{(c)}}{\partial x} &= K_6 \frac{\lambda \sinh[\lambda(L - x)]}{\cosh(\lambda L)} - \frac{K_5}{K_4} (L - x) Q \\ \frac{\partial^2 w}{\partial x^2} &= \frac{K_1}{K_2} \frac{\partial \phi^{(c)}}{\partial x} + \frac{1}{K_2} (L - x) Q. \end{aligned}$$

The above formulation can be used to calculate the stress distribution at any location under either a mechanical force or an electrical load or both. Setting $Q = 0$, the stress distribution under an electrical load is calculated as shown in Fig. 8. It is clear that axial stress exists only for the range of $x < 1\text{ cm}$ and vanishes for $x \geq 1\text{ cm}$. This result also corresponds to variations of the local rotation, $\phi^{(c)}$, along the axial locations. As shown in Fig. 5, the local rotation, $\phi^{(c)}$, reached a saturated value at $x = 1\text{ cm}$; this means that the variation rate of the local rotation, $\frac{\partial \phi^{(c)}}{\partial x}$, diminishes for $x \geq 1\text{ cm}$. According to Eq. (37), axial stress vanishes for $x \geq 1\text{ cm}$ when no mechanical load is applied.

For the surface-mounted actuation beam, the stress distribution can be similarly

obtained as

$$\sigma_x = \begin{cases} -Q_{11}^E z \frac{\partial^2 w}{\partial x^2} - e_{31}^X E_z & -\frac{t_f}{2} - t \leq z \leq -\frac{t_f}{2} \\ -Q_{11} z \frac{\partial^2 w}{\partial x^2} & -\frac{t_f}{2} \leq z \leq \frac{t_f}{2} \\ -Q_{11}^E z \frac{\partial^2 w}{\partial x^2} + e_{31}^X E_z & \frac{t_f}{2} \leq z \leq \frac{t_f}{2} + t \end{cases} \quad (38)$$

where

$$\frac{\partial^2 w}{\partial x^2} = -\frac{Q}{EI} x + \frac{1}{EI} [Q L + e_{31}^X (t + t_c) t E_z].$$

Equation (38) may be used to calculate the stress distribution of the surface-mounted actuation beam at any location under either a mechanical force or an electrical load or both. Setting $Q = 0$, the stress distribution under an electrical load is calculated as shown in Fig. 9. It should be noted that the axial stress distributions are identical for any axial location. To verify the stress formulation for the surface-mounted actuation beam, the stress distribution through the thickness at $x = 5\text{ cm}$ is compared with the finite element results, as shown in Fig. 10. It is clear that the analytical solution agrees very well with the finite element analysis.

6 DISCUSSION AND CONCLUSION

A new adaptive sandwich structure is constructed using the shear mode of piezoelectric materials. Governing equations for the proposed structure and its surface-mounted counterpart are derived based on the variational principle. The static solutions of a cantilever sandwich beam and its corresponding surface-mounted beam are obtained based on the derived general formulations. The theoretical formulation is verified by finite element analysis. Furthermore, stress distributions of the two structures are also theoretically characterized.

The greatest advantage provided by the adaptive sandwich beam is its lower stresses in the actuator. Since piezoceramics are very brittle, high stresses are detri-

mental to the structural integrity of the actuator. According to the results shown in Fig. 8 and Fig. 9, it is evident that under electrical loading the level of axial stress in the surface-mounted actuators is very high, and is negligible in the piezoelectric core of the sandwich beam. The shear stresses for both structures under electrical loading are negligible. For the case under mechanical loading, the overall axial-stress distributions for both structures are similar.⁶ However, the stress levels within the actuators for the two structures are very different due to their different locations along the thickness directions. For the sandwich structure, the actuator sustains the lowest bending stress level within the structure because the piezoelectric core is located near the neutral plane of the beam. For the surface-mounted actuation beam, the piezoelectric actuators bear the largest bending stress level in the structure since the actuators are located at the farthest locations from the neutral plane.

Due to the high density and the brittleness of piezoelectric materials, it is impractical to use an entire piezoelectric layer in adaptive structures. If an entire piezoelectric layer is employed in a large structure, the flexibility of the structure will be dramatically reduced. However, the above formulations provide a basis for further study of an adaptive sandwich with small piezoelectric patches.

ACKNOWLEDGMENT

This work was supported by AFOSR through grant F 49620-92-J-0457 to Purdue University.

7 REFERENCES

- [1] E. Crawley and J. de Luis, 1987, "Use of piezoceramic actuators as elements of intelligent structures", *AIAA Journal*, Vol. 25, pp. 1373-1385.
- [2] K. Uchino, 1986, "Electrostrictive actuators: materials and applications", *Ceramic Bulletin*, Vol. 65, pp. 647-652.
- [3] E. Crawley and E. Anderson, "Detailed models of piezoelectric actuation of beams", *Proceedings of 30th AIAA/ASME/SAE Structures, Structural Dynamics, and Material Conference*, Washington, DC, April 1989, pp. 2000-2010.
- [4] C. K. Lee, 1990, "Theory of laminated piezoelectric plates for the design of distributed sensors/actuators. part I: governing equations and reciprocal relationships", *Journal of Acoustical Society of America*, Vol. 87, pp. 1144-1158.
- [5] M. Leibowitz and J. R. Vinson, 1993, "The Use of Hamilton's Principle in Laminated Piezoelectric and Composite Structures", *Adaptive Structures and Material System AD-Vol. 35*, Paper Presented at the 1993 ASME Winter Annual Meeting, New Orleans, Louisiana, November 28-December 3, 1993, pp. 257-167.
- [6] C. T. Sun and X. D. Zhang, 1995, "Use of Thickness-Shear Mode in Constructing Adaptive Sandwich Structure", *Smart Materials and Structures*, Vol. 4, pp. 202-206.
- [7] H. F. Tiersten, 1969, *Linear Piezoelectric Plate Vibrations*, Plenum Press, New York, New York, pp. 33-39.

Table 1: Mechanical Properties for Computer Simulation

PZT5H								Al	
GPa					C/m ²			GPa	
c_{11}	c_{12}	c_{13}	c_{33}	c_{44}	e_{31}	e_{33}	e_{15}	E	ν
126	79.5	84.1	117	23	-6.5	23.3	17.0	70.3	0.345

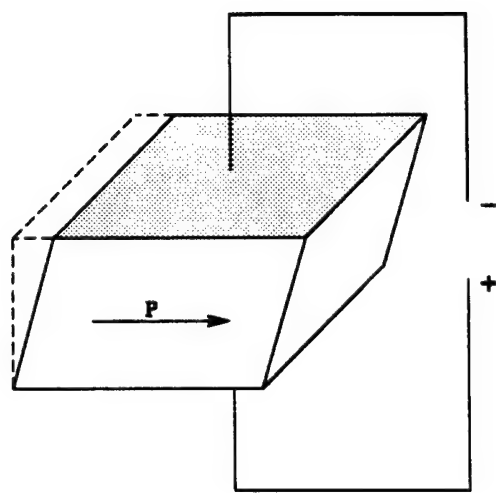


Figure 1: Shear Mode of the Piezoelectric Core

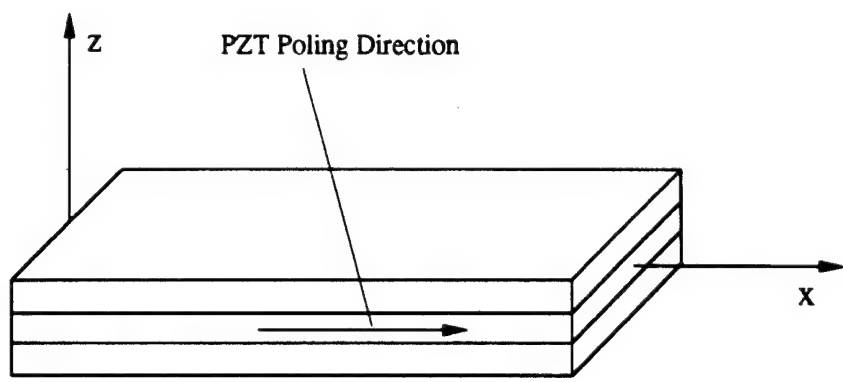


Figure 2: Schematic Diagram of the Sandwich Beam

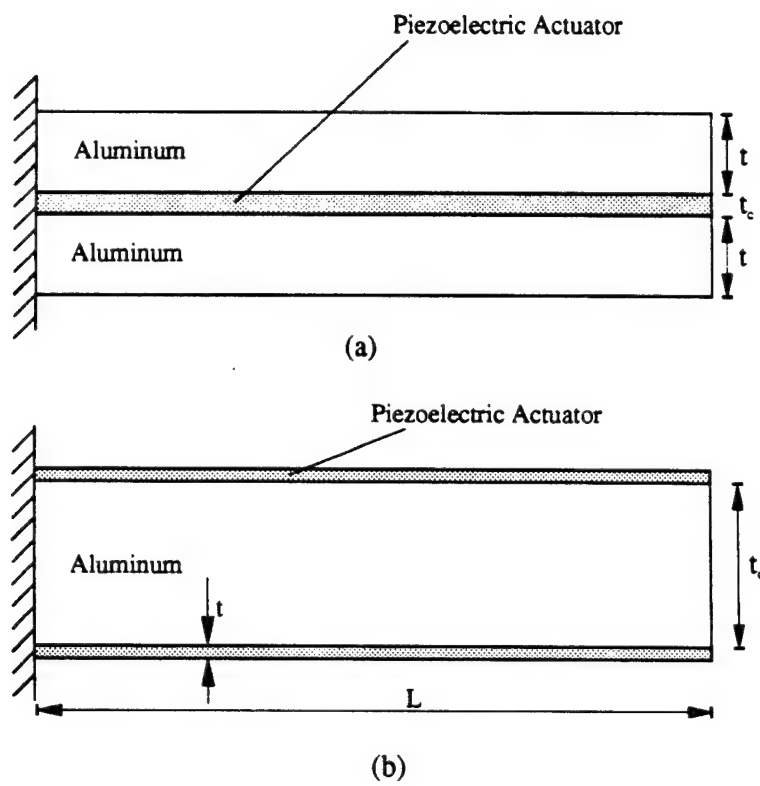


Figure 3: Adaptive Sandwich Beam (a) and Surface-Mounted Actuation Beam (b) of Unit Width

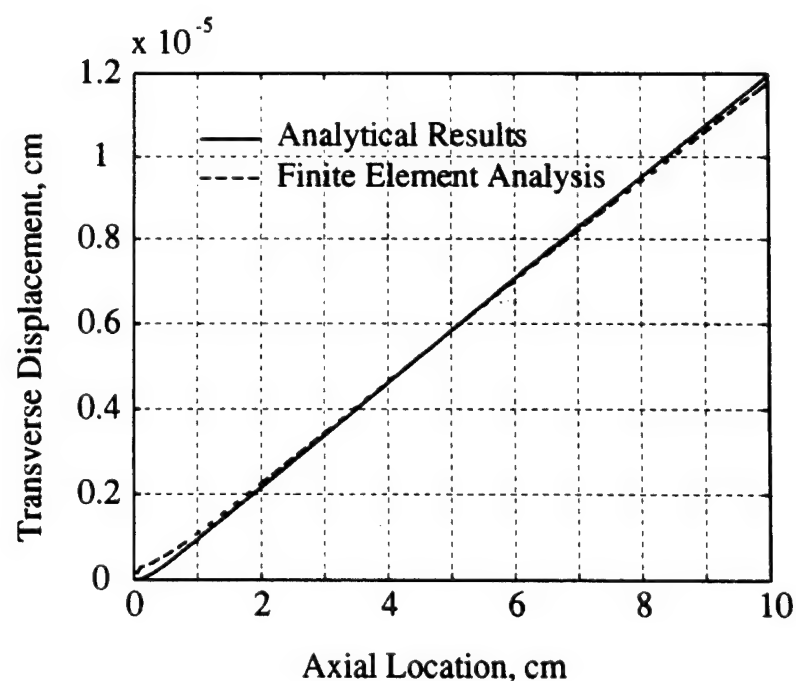


Figure 4: Transverse Displacement vs. Axial Location for the Sandwich Beam

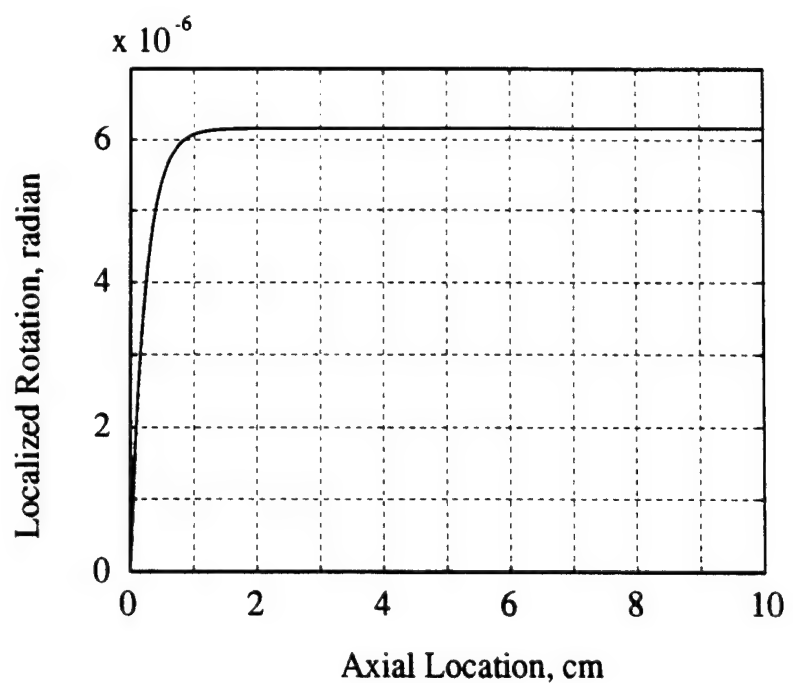


Figure 5: Local Rotation vs. Axial Location for the Sandwich Beam

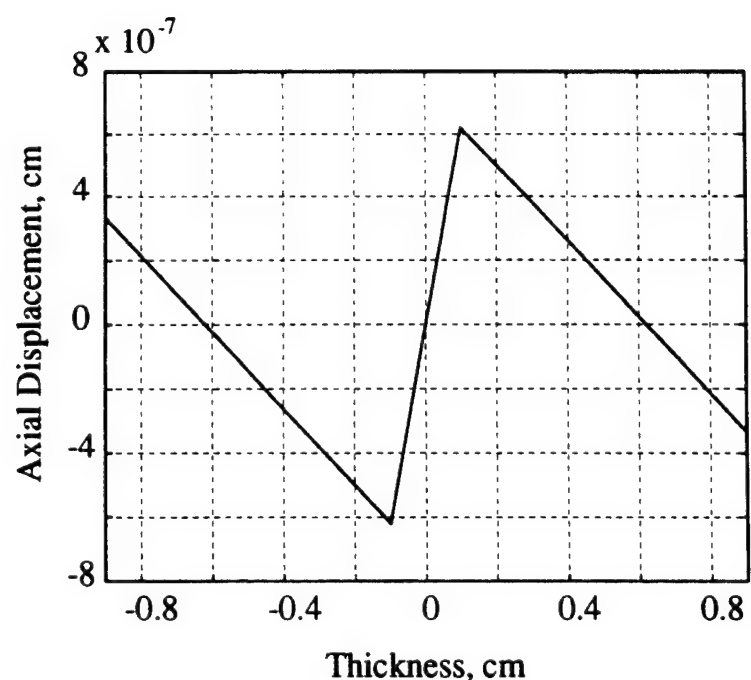


Figure 6: Axial Displacement of the Sandwich Beam By Finite Element Analysis

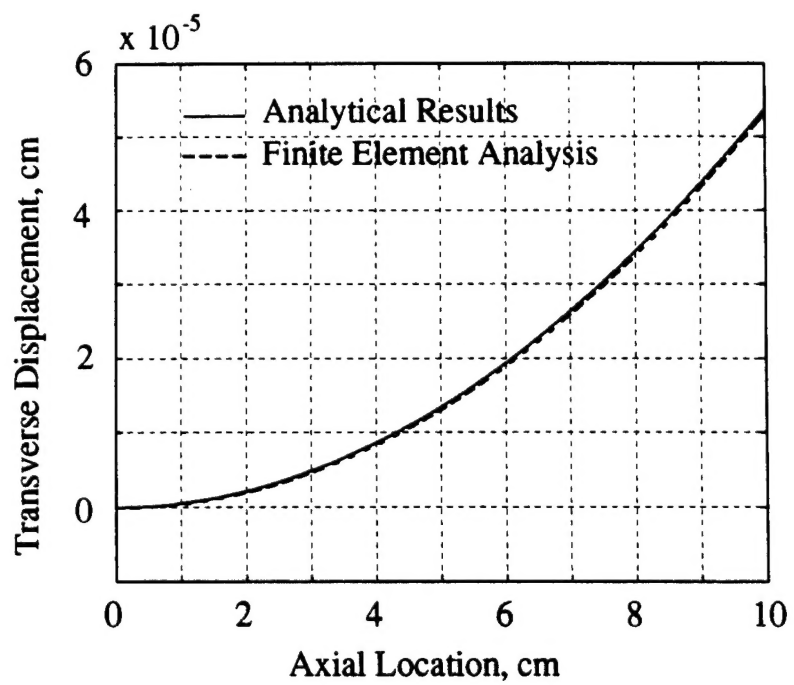


Figure 7: Transverse Displacement vs. Axial Location for the Surface-mounted Actuation Beam

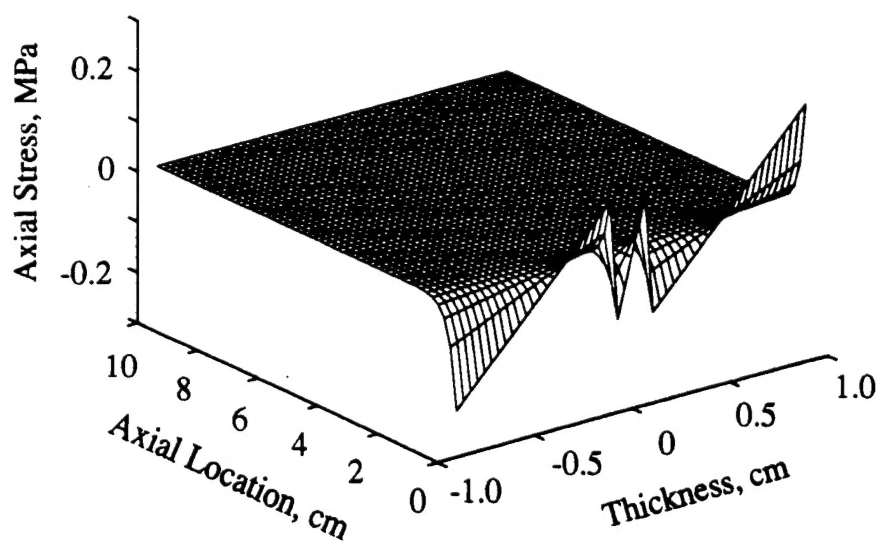


Figure 8: Stress Distribution of the Sandwich Beam Under an Electrical Load

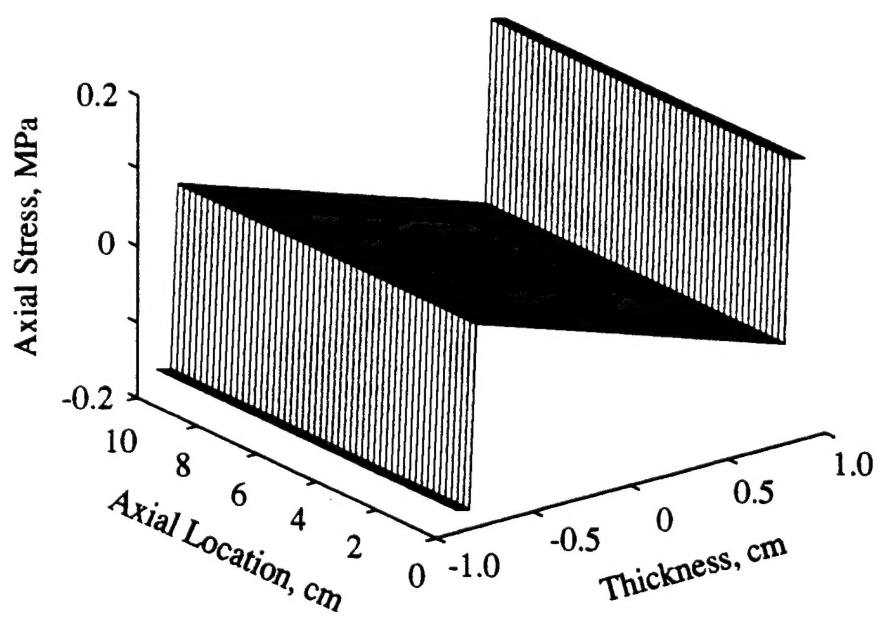


Figure 9: Stress Distribution of the Surface-Mounted Beam Under an Electrical Load

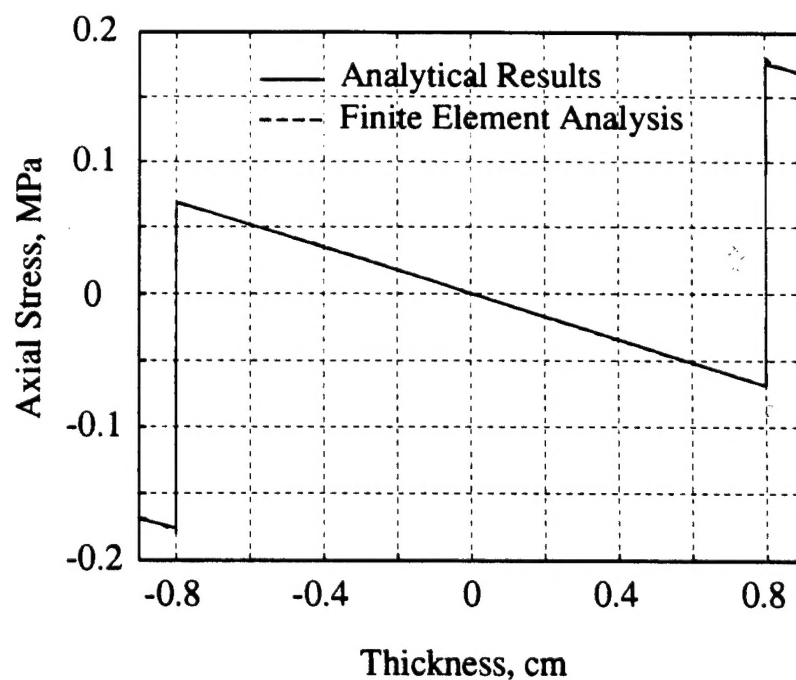


Figure 10: Stress Distribution of the Surface-Mounted Beam Through the Thickness